ABSTRACT

Title of Dissertation: ***HIGH-ENERGY-DENSITY LITHIUM-SULFUR BATTERIES USING GARNET SOLID ELECTROLYTE: PERFORMANCE AND CHARACTERIZATION***

Changmin Shi, Doctor of Philosophy, 2023

Dissertation directed by: Professor Eric D. Wachsman
Department of Materials Science and Engineering

There is every-growing clean energy storage systems demand to address the climate change challenges. The Lithium-Sulfur (Li-S) battery using solid-state electrolyte (SSE), therefore, are becoming a rising star to meet this requirement due to the low cost and high domestic availability of sulfur, exceptionally high theoretical energy density of sulfur chemistry, less flammability, the potential for suppression of the polysulfide shuttle, Li dendrite growth, low coulombic efficiency, and short circuiting in more conventional liquid electrolyte Li-S batteries. The most popular SSEs in Li-S battery field are $Li_{10}GeP_2S_{12}$ (LGPS) and Li stuffed garnet type $Li_7La_3Zr_2O_{12}$ (LLZO) with a space group of $Ia\bar{3}d$. LGPS has a high ionic conductivity of 1–10 mS/cm at room temperature (22℃), but the generation of H_2S toxic gas when reacting with moisture and the instability with Li metal limit its applications. LLZO is a highly promising SSE for Li-S batteries due to its reasonably high ionic conductivity (0.1–1 mS/cm) at 22℃ and excellent chemical stability with Li metal. However, Li dendrite growth is still observed in LLZO. To overcome the potential Li dendrite

growth issue, our group introduced a novel 3D porous/dense bilayer and porous/dense/porous trilayer LLZO structures that achieve an exceptional Li stripping/plating performance at a high current density of 10 mA/cm^2 at 22℃ with no applied pressure. Although significant improvement has been done in mitigating the LLZO/Li anode interface, further work on stabilizing the sulfur/LLZO interface still needs to be done to achieve high energy density and stable cycling Li-S batteries.

Through the studies in this dissertation, it was observed that La segregation to the LLZO surface on the sulfur cathode side led to Li-S battery charge failure. To address the issue, a PEO-based interlayer was applied on the cathode side to physically separate sulfur cathode and LLZO. Consequently, the Li-S batteries demonstrated a high initial discharge capacity of 1307 mAh/g at 22℃, corresponding to an energy density of 134 Wh/kg and 639 Wh/L. Next, since the PEO-based interlayer has a low ionic conductivity, an in-situ formed gel polymer electrolyte (GPE) was invented as a catholyte that had a high ionic conductivity of 3.5–5.6 mS/cm at 22℃. With an organic sulfur cathode (active material: sulfurized polyacrylonitrile) and a thin bilayer LLZO architecture, a very stable cycling using high sulfur loading (5.2 mg/cm^2) was obtained for 60 cycles at a discharge current density of 0.87 mA/cm^2 with a high initial discharge capacity of 1542 mAh/g, corresponding to an energy density of 223 Wh/kg and 769 Wh/L. In addition, using the same configuration and sulfur loading but using a different cell, 80% capacity retention for over 265 cycles was demonstrated at a discharge current density of 1.74 mA/cm^2 at 22℃. In the third project, as a small amount of flammable organic liquid catholyte and/or GPE compromises on the safety of solid-state batteries, the proof-of-concept “all-solid-state” Li-S battery using LLZO electrolyte was first innovated through a novel three-phase sulfur cathode to meet the high safety demand of solid-state Li-S batteries. In addition, by using the same “all-solid-state” battery design

and a 3D column LLZO architecture, a high energy density of 338 Wh/kg and 797 Wh/L was demonstrated.

HIGH-ENERGY-DENSITY LITHIUM-SULFUR BATTERIES USING GARNET SOLID ELECTROLYTE: PERFORMANCE AND CHARACTERIZATION

by

Changmin Shi

Dissertation submitted to the Faculty of the Graduate School of the
University of Maryland, College Park, in partial fulfillment
of the requirements for the degree of
[Doctor of Philosophy]
[2023]

Advisory Committee:
Professor Eric D. Wachsman, *Chair/Advisor*
Professor Liangbing Hu
Associate Professor Yifei Mo
Assistant Professor Paul Albertus
Professor Chunsheng Wang, *Dean's Representative*

© Copyright by
Changmin Shi
2023

Dedication

To my beloved and inspiring parents and younger sister,

I thank you for always

supporting me on pursuing my dreams

&

helping me become who I am.

献给我亲爱的爸爸妈妈和我的妹妹，

感谢你们

一直都支持我追求梦想，帮助我成为我想要的样子

Acknowledgements

My Ph.D. dissertation not only represents my research progress, but also is the results of experiences and memories that I have had at the University of Maryland, College Park from numerous remarkable individuals whom I wish to acknowledge.

I want to express my deepest gratitude to my research advisor Dr. Eric D. Wachsman for his supporting during my Ph.D. career. Thank you for having me in the world top-tier research group to conduct energy storage research to solve the most difficult energy challenges in the world. I am very grateful for the many opportunities to learn new practice research knowledge and skills, including but not limited to tape-casted ceramic synthesis, battery assembly, and materials characterizations. I sincerely appreciate your guidance and insightful comments to produce high quality research results and publications. Lastly, as an international student whose first language is not English, I am also always grateful for your understanding towards cultural differences and the way of my English language expression.

I want to thank my first research mentor in Wachsman Group: Dr. Tanner Hamann. Thank you for teaching me how to be an experimentalist through days and nights, training me on characterization skills and equipment necessary for my research with extreme patience, and for being always available whenever I needed your help. I can never forget the time when we worked together until after midnight. I also want to thank my peer mentor Dr. Adelaide Nolan graduated from Dr. Yifei Mo's group. Thank you for sharing your personal experiences in your Ph.D. life with me and providing numerous of supports and introducing your friends to me to get to know different research groups when I started to search for a research group to join. I would

also like to thank you and Professor Mo for providing us with the sulfur/garnet electrolyte stability first principal simulation which is very important to understand the battery failure mechanism.

I want to thank my colleagues in battery research at Wachsman Lab: Dr. Lei Zhang, Dr. George Alexander, Dr. Prem Jaschin, Dr. Yaoyu Ren, Dr. Dennis McOwen, Dr. Zhezhen Fu, Dr. Yi-Lin Huang, Griffin Godbey, Jon O'Neill, Jack Evans, and Richard Hoft. I am grateful for sharing your expertise with me on electrochemistry, garnet electrolyte, and solid-state batteries and training me on tape-casting ceramic synthesis and electrochemical analysis. I would also like to thank my colleagues in the research laboratory as a whole: Dr. Eugene Ostrovskiy and Dr. Sam Horlick. Thank you for the joy and happiness you brought to my entire Ph.D. period. I also enjoyed and greatly benefitted from the many discussions about published literatures, the possible methods to improve my experiments.

I want to thank my colleagues from Hu Lab: Dr. Hua Xie and Dr. Chunpeng Yang and Prof. Liangbing Hu. Thank you for training me on coin cell assembly that is very essential to my Ph.D. research and sharing your battery and electrochemistry expertise with me.

I want to thank my colleagues from Wang Lab: An Pham and Dr. Ai-Min Li and Professor Chunsheng Wang. Thank you for providing me with the organic sulfur compound powder and training me on how to synthesize it.

I want to thank Dr. Jiancun Rao, Dr. Sz-Chian Liou, and Dr. Wen-An Chiou of the UMD AIMLab for training me to use Tescan XEIA and GAIA scanning electron microscopy (SEM) and energy dispersive X-ray spectroscopy, both of which were

invaluable for my Ph.D. research. I am also grateful for your patience when answering my many confusions about instrument operations, sample preparations and results analysis. I also want to thank Maryland Nanocenter and its AIMLab for providing the access to its facilities and instrumentation.

I want to thank Dr. Peter Zavalij and the Teaching Assistant of the UMD X-ray Crystallographic Center. Thank you for training me on the X-ray diffraction (XRD) instrument and assisted me with my sample preparations and results analysis. XRD is a critical tool during my Ph.D. life for studying the garnet electrolyte phase structure stability under different electrochemical and chemical testing conditions.

I want to thank John Abrahams, Jonathan Hummel, Tom Loughran and Mark Lecates from UMD Fablab. Thank you for training me on the atomic layer deposition systems, Fablab SEM, Metra Thermal Evaporator and Fablab glovebox, respectively. These instruments allowed me to greatly improve my garnet and cathode performances, and to learn my garnet structure.

I want to thank funding agency Department of Energy through the Advanced Research Projects Agency–Energy, Army Research Laboratory, and the Center for Research on Extreme Battery to support my work during Ph.D.

I want to thank Ms. Adaire Parker and Professor Ichiro Takeuchi, who I could always come to with questions about registration for classes, the requirements of the Department of Materials Science and Engineering Graduate Program, graduation process and its important deadline.

Last but not least, I want to thank my family and friends. Thank you for always supporting me to pursue my dream and helping me stay focused on my goals. I

especially want to thank my parents and my younger sister, who give me tremendous unconditional love. You are the foundation of my life.

Table of Contents

Dedication ..... *ii*

Acknowledgements ..... *iii*

Table of Contents ..... *vii*

List of Tables ..... *ix*

List of Figures ..... *xi*

List of Abbreviations and Symbols ..... *xxii*

Chapter 1: Introduction to Li-S Batteries *1*

1.1 Why Use Li-S Batteries? **1**

1.2 Sulfur Cathode Working Principles **2**

1.2.1. Solid-Liquid-Solid Transition 2

1.2.2. Solid-Solid Transition 3

1.3 Anodes for Li-S Batteries **4**

1.4 Organic Liquid Electrolytes **5**

1.5 Solid-State Electrolytes for Li-S Batteries **6**

1.5.1. Advantages and Disadvantages on Sulfide Electrolytes 6

1.5.2. Advantages and Disadvantages on Oxide Electrolytes 7

1.6 Challenges of Li-S Batteries Using Garnet Electrolytes **7**

Chapter 2: Characterization Techniques *9*

2.1 XRD **10**

2.2 XRF **10**

2.3 SEM and EDX **11**

2.4 ToF-SIMS **12**

2.5 TEM **12**

2.6 XPS **13**

2.7 ATR-FTIR **13**

2.8 Elemental Analysis **14**

2.9 Electrochemical Techniques **14**

2.9.1. Battery Cycling Techniques 14

2.9.2. EIS 15

2.9.3. CV 15

Chapter 3: Research Objectives *16*

Chapter 4: Stabilizing Sulfur Cathode/Garnet Electrolyte Interface to Achieve High Energy Density Using 3D Asymmetric Electrolyte Architecture *20*

4.1 Introduction 20

4.2 Experimental 22

4.3 Results and Discussions 26

4.3.1 La Segregation Impacts on Cell Failure 26
4.3.2 3D Asymmetric Bilayer Garnet Hybridized Li-S Battery Design 34
4.3.3 Electrochemical Performance of the Hybridized Li-S Batteries 36
4.3.4 Chemical and Electrochemical Stability and Mechanical Properties 41
4.3.5 Energy Density Evaluation of the Hybridized Li-S Batteries 52

4.4 Conclusions 56

Chapter 5: High Sulfur Loading and Capacity Retention in Bilayer Garnet Lithium-Sulfur Batteries with Gel Polymer Electrolytes 58

5.1 Introduction 58

5.2 Experimental 59

5.3 Results and Discussions 64

5.3.1 *In-situ* Gel Polymer Electrolyte 64
5.3.2 Electrochemical Performance of GPE/Bilayer Ta-LLZO Design 70
5.3.3 Cell Performance Comparison 74
5.3.3 Characterizations on the Cell Stability 79

5.4 Conclusions 91

Chapter 6: All-Solid-State Garnet type Li-S Battery Enabled by Inorganic Conductive Lithium Salt and 3D Garnet Electrolyte Architectures 93

6.1 Introduction 93

6.2 Experimental 94

6.3 Results and Discussions 98

6.3.1 *Solid Catholyte Development* 98
6.3.2 *All-Solid-State Cathode Structure* 101
6.3.3 *Cell Performance* 107
6.3.4 *High-Energy-Density All-Solid-State Garnet Li-S Batteries* 115

6.4 Conclusions 121

Chapter 7: Conclusions and Future Work 123

7.1 Conclusions 123

7.2 Future Work 125

Chapter 8: Publications 126

Bibliography 127

List of Tables

Table 4.1. Summary of the XRF results on the sintered La excess/deficient samples

Table 4.2. Potential decomposition products between different sulfur species and La_2O_3 based on first principal calculation

Table 4.3. The Coulombic Efficiency comparison of our designs with other Li-S cells and the effect of polysulfide shuttle

Table 4.4. The energy density calculation

Table 4.5. The comparison on initial discharge capacity and its related energy density of our work with the state-of-art published results

Table 5.1. The elemental analysis of carbon and nitrogen in SPAN powder

Table 5.2. The ATR-FTIR details of the GPE

Table 5.3. Electrochemical performance of different pairs of 2M and 3M GPE cells

Table 5.4. The demonstrated energy density of the 2M GPE/bilayer Ta-LLZO design based on initial discharge capacity

Table 5.5. A comparison of our work with the state-of-art published results

Table 6.1. Cell performance summary

Table 6.2. High-energy-density cell performance summary

Table 6.3. The demonstrated energy density of the all-solid-state garnet Li-S battery using 3D column structure

Table 6.4. Energy density comparison of our work with the state-of-art published results

List of Figures

Figure 1.1. The schematic of the sulfur cathode working principle through "solid to liquid to solid" transition.

Figure 1.2. The schematic of the sulfur cathode working principle through "solid to solid" transition.

Figure 3.1. The thermodynamic stability of different sulfur species with pure cubic phase LLZO. All sulfur species except Li_2S are thermodynamically unstable with LLZO, which can cause continuous reaction between the sulfur cathode and LLZO in long-term cycling.

Figure 3.2. The SEM images (top view)/EDX mapping of Ca/Nb co-doped LLZO. The La segregation can be eliminated by Ca dopant partially occupation in the La site. The scale bar is 5μm.

Figure 3.3. The voltage profile of garnet Li-S cell tested at 0.03C at RT under a sulfur mass loading of 4 mg/cm^2 using the normal stoichiometric Ta-LLZO ($Li_{6.75}La_3Zr_{1.75}Ta_{0.25}O_{12}$).

Figure 4.1. Schematic of the 3-point bending model for mechanical properties investigation.

Figure 4.2. La segregation indications on cell failure. (a). The voltage profile of garnet Li-S cell tested at 0.03C at RT using the normal stoichiometric Ta-LLZO. (b) Voltage profile of garnet Li-S cell tested at 0.03C at RT using the 5wt% La excess Ta-LLZO. (c) Voltage profile of garnet Li-S cell tested at 0.03C at RT using 5wt% La deficient Ta-LLZO. (d). The calculated mutual reaction energy of pseudo-binaries of different sulfur species and La_2O_3. (e) The SEM and EDX mapping images of the Ta-LLZO (normal stoichiometry, top view) showing the La segregation. (f) SEM (top view) and

EDX mapping images of the 5wt% La excess Ta-LLZO. (g). SEM (top view) and EDX mapping images of the 5wt% La deficient Ta-LLZO. The scale bar for (f) and (g) is all 10 μm.

Figure 4.3. La excess Ta-LLZO sample characterizations. (a). The La excess Ta-LLZO XRD pattern. When different amount of extra La is added, the impurity phase of La_2O_3 is observed in all the samples. The impurity intensity goes higher when more La element is added in the Ta-LLZO. (b). The SEM images (top view)/EDX mapping of La excess Ta-LLZO with different amount of La excess. Both show La segregation. Combined with the XRD results, it is indicated that the La segregation phase is the La_2O_3. The scale bar is all 10 μm.

Figure 4.4. La deficient Ta-LLZO sample characterizations. (a). The La deficient Ta-LLZO XRD pattern. There is no impurity peak in 5wt.% La deficient Ta-LLZO compared with 1wt.% and 3wt.% La deficient Ta-LLZO that both have $La_2Zr_2O_7$ impurity phase. (b). The SEM images (top view)/EDX mapping of La deficient Ta-LLZO with different amount of La deficiency. Note that even in 1wt% La deficient Ta-LLZO, it shows La segregation. While when it comes to 3wt% and 5wt% La deficient Ta-LLZO, the La segregation disappears showing uniform La element mapping. The scale bar is all 10 μm.

Figure 4.5. The impedance of the 5%wt La deficient Ta-LLZO tested by using blocking Au electrodes, which leads to a conductivity of 10^{-5} S/cm^2 at RT. The frequency range is from 1MHz to 100 Hz.

Figure 4.6. Schematic fabrication of the high energy density hybridized Li-S cell.

Figure 4.7. The characterizations of the bilayer Ta-LLZO with PEO-based interlayer coating used in the study. (a) The in-beam mode SEM cross-section images of 3D bilayer Ta-LLZO structure with a thickness of 95 μm in dense layer and a 25 μm in porous layer with a dense layer on top and a porous layer at the bottom. (b). The SEM

image of Li infiltration condition in the porous side of the 3D bilayer Ta-LLZO. (c). The ZnO ALD layer thickness distribution on a silicon wafer surface. The total thickness of the ZnO ALD layer is on an average of (2.33 ± 0.013) nm with little variation. (d). The cross-section of the PEO-based membrane and Ta-LLZO bilayer (dense side) showing the thickness of the PEO-based interlayer is around 8.4 μm.

Figure 4.8. (a). The ASR of Li-Li symmetric cells for 1M LiFSI in DME (22.7 Ω-cm^2: the ASR of the liquid electrolyte and its SEI formation) and PEO/LiFSI membrane with 1M LiFSI in DME (70.4 Ω-cm^2: the ASR of the liquid electrolyte, its SEI formation, PEO/LiFSI membrane and the liquid electrolyte/PEO-based membrane interface). To make it comparable, the amount of each materials kept the same as that in Figure 4.9. (b). The ASR of Li-S full cells before and after cycling at 0.03C. The ASR of PEO/bilayer before cycling and after cycling is 921 Ω-cm^2 and 691 Ω-cm^2, respectively.

Figure 4.9. Electrochemical performance of the 3D asymmetric bilayer garnet hybridized Li-S cells. a) The dense PEO/bilayer and Celgard/bilayer cells cycling performance tested at 0.03C at RT and b) the voltage profile of the PEO/bilayer cells at 0.03C at RT. c) The PEO/bilayer cell tested at 0.05C at RT and d) the voltage profile of the PEO/bilayer cells at 0.05C at RT. e) The comparison of rate capability of PEO/bilayer and Celgard/bilayer cells. and f) the voltage profile of C-rate test of PEO/bilayer cell.

Figure 4.10. The full cycling performance of the PEO/bilayer cells reported in Figure 2. a). and b) are the 200 cycles and 100 cycles for the cells tested at 0.03C and 0.05C at RT, respectively. There is a capacity jump decrease after 35 cycles at 0.03C with lower Coulombic Efficiency for 7 cycles. But overall, the average Coulombic Efficiency at 0.03C and 0.05C is 99.4% and 99.8%, respectively, which demonstrate the polysulfide shuttle is fully blocked.

Figure 4.11. The XRD patterns of the hybridized electrolyte before and after cycling. PEO/LiFSI membrane only (black curve), PEO/LiFSI membrane on top of the bilayer

Ta-LLZO (red curve), PEO/LiFSI membrane on top of the bilayer Ta-LLZO rinsed by ACN (blue curve) and the hybridized electrolyte of the cycled cell rinsed by DME and ACN (purple curve).

Figure 4.12. XPS depth profiling of Ta-LLZO. a). and b). are the Zr *3d* and La *3d* XPS spectra after Ar^+ sputtering for 10min, 20 min and 40 min, respectively.

Figure 4.13. XPS spectra of Li 1s, S 2p, C 1s, N 1s, F 1s, and O 1s from an unsputtered non-cycled control sample (pellet LLZO coated with PEO soaked with LiFSI/DME, followed by ACN).

Figure 4.14. XPS spectra of Li 1s, S 2p, C 1s, N 1s, F 1s, and O 1s from an unsputtered cycled samples.

Figure 4.15. The ToF-SIMS depth profile of the cycled PEO/bilayer cell.

Figure 4.16. Mechanical properties of the Ta-LLZO and PEO electrolyte. a) and b) are the stress distribution of the Ta-LLZO and PEO electrolyte, respectively. c) and d) are the strain distribution of the Ta-LLZO and PEO electrolyte, respectively.

Figure 4.17. Cell energy density evaluation. a) and b–c) The comparison of initial discharge capacity and energy density in this work with state-of-art published results, respectively.

Figure 4.18. The further energy density prediction based on different parameters optimizations of the PEO/bilayer design versus sulfur mass loading and varying dense layer thickness in the bilayer Ta-LLZO.

Figure 5.1. The XRD pattern of the Ta-LLZO pellet for symmetric cell studies, showing its pure cubic garnet phase.

Figure 5.2. (a). Secondary electron mode and (b). back scatter electron mode SEM images of the as-synthesized bilayer Ta-LLZO. The dense layer and porous layer thickness are 40 and 55 μm, respectively.

Figure 5.3. (a) Schematic illustration of our cell configuration and the in-situ formed GPE on the bilayer LLZO. (b). The ATR-FTIR of the pure LiFSI, DOL, poly-DOL, DME and the GPE. (c). EIS measurement of different concentrated GPE. The frequency range is from 0.1MHz to 100 Hz with an amplitude of 25 mV.

Figure 5.4. The ionic conductivity of different GPEs.

Figure 5.5. The interfacial impedance between the GPE and Ta-LLZO. (a). Equivalent circuit of the Stainless Steel (SS)/GPE/Ta-LLZO pellet/GPE/Stainless Steel (SS) cell configuration. R_0 is the environmental resistance and R_{GPE} is the resistance contributed from GPE. R_G, R_{GB}, $R_{G/L}$, R_W is the resistance of bulk Ta-LLZO, Ta-LLZO grain boundary, interface between GPE and Ta-LLZO and the Warburg resistance, respectively. CPE_G, CPE_{GB}, $CPE_{G/L}$ and CPE_W are the constant phase element of Ta-LLZO grain, Ta-LLZO grain boundary, the interface between GPE and LLZO and Warburg diffusion tail, respectively. (b). Equivalent circuit of the SPAN cathode/GPE/ GPE/SPAN cathode cell configuration. R_0 is the environmental resistance. R_C, $R_{C/G}$, R_W is the resistance of the SPAN cathode, interface between SPAN cathode and GPE and the Warburg resistance, respectively. $CPE_{C/G}$ and CPE_W are the constant phase element of the interface between SPAN cathode and GPE and Warburg diffusion tail, respectively. The analytical approach was the same here as in our previous publication(1). (c–e) are the EIS of the SS/1M GPE/Ta-LLZO pellet/2M GPE/SS, SS/2M GPE/LLZO pellet/2M GPE/SS and SS/3M GPE/LLZO pellet/2M GPE/SS symmetric cell, respectively. The frequency was from 1MHz to 100 Hz. (f–h) are the EIS of the SPAN cathode/1M GPE/SPAN cathode, SPAN cathode/2M GPE/SPAN cathode and SPAN cathode/3M GPE/SPAN cathode symmetric cell, respectively. The frequency was from 1MHz to 1 Hz.

Figure 5.6. The electrochemical performance tests of our GPE/bilayer Ta-LLZO designs. (a) The voltage profile of the 1M GPE cell. The charge process cannot be finished. (b) and (c) Cycling performances of 2M and 3M GPE cells, respectively. (d) Cycling performances of 2M and 3M GPE cells. The discharge and charge current density for (a)–(d) are 0.87 mA/cm^2 and 0.435 mA/cm^2, respectively. (e). Cycling performances of 2M and 3M GPE cells at a discharge current density of 1.74 mA/cm^2. (f). Capacity recoverability/C-rate performances of the 2M GPE design ranging from 1.74 mA/cm^2 to 8.7 mA/cm^2 and then back to 1.74 mA/cm^2. Note that, c-rate is based on the theoretical capacity of elemental sulfur.

Figure 5.7. The voltage profile of the (a) 2M GPE/bilayer Ta-LLZO and of (b) the 3M GPE/bilayer Ta-LLZO with an optimized cycling voltage window at a discharge current density of 1.74 mA/cm^2.

Figure 5.8. The voltage profile of the capacity recoverability test of Figure 5.6f. The current density (discharge/charge) of cell #5 at the 5th, 15th, 25th, 35th and 45th cycle is 1.74/0.435, 2.61/0.435, 4.35/0.435 and 1.74/0.435, respectively. The current density unit is mA/cm^2.

Figure 5.9. The electrochemical characterizations of GPE/bilayer LLZO Li-S batteries. (a) and (b) are the EIS measurement of 2M and 3M GPE/bilayer Ta-LLZO batteries before cycling at 22℃ with an amplitude of 10 mV and a frequency range of 7 MHz to 0.01 Hz, respectively.

Figure 5.10. Cell performance evaluation. (a), (b) and (c–d) are the comparison of total number of cycles, average discharge capacity and energy density, respectively. Note that, open stars and solid stars indicated the demonstrated and projected energy densities, respectively. Note that, in Figure 3c–d, the open and solid red stars represented the achieved energy density based on initial and average capacities, respectively. The open and solid violet stars represented the projected energy density based on initial and average capacities, respectively. The detailed values are quantified in Table 5.5 with references cited.

Figure 5.11. The further energy density prediction versus sulfur mass loading by using the dense layer thickness to be 10 μm in the bilayer Ta-LLZO.

Figure 5.12. The XRD pattern of the 1M/2M/3M GPE/bilayer Ta-LLZO after cycling. All of them showed a pure cubic LLZO phase without impurity.

Figure 5.13. XPS analysis on the electrochemical decomposition between Ta-LLZO and GPE through XPS. C 1s and F 1s spectra of Ta-LLZO charged in 1M GPE and cycled in 3M GPE. (a) and (b) shows C 1s spectra of 1M GPE and 3M GPE, respectively. (c) and (d) shows F 1s spectra of 1M GPE and 3M GPE, respectively. The same color was used for the same decomposed compounds in C 1s and F 1s spectra for 1M and 3M GPE to be easy for comparison.

Figure 5.14. (a–d) Li 1s, S 2p, N 1s, and O 1s spectra of Ta-LLZO in 1M GPE having prolong charged issue. (d–h) Li 1s, S 2p, N 1s, and O 1s spectra of Ta-LLZO cycled in 3M GPE.

Figure 5.15. C 1s, F 1s, Li 1s, S 2p, N 1s, and O 1s spectra of Ta-LLZO cycled in 2M GPE.

Figure 5.16. (a) The SPAN cathode after fully discharged at 1M GPE/bilayer-LLZO case configuration. (b) The SEM image of pristine SPAN cathode without electrochemical cycling.

Figure 5.17. The morphology of SPAN cathode after cycling. (a–b). The SPAN cathode under fully discharged state with an applied discharge current density of 0.87 mA/cm^2 for 2M, and 3M GPE case, respectively. (c–d). The SPAN cathode after cycling under fully charged state for 2M and 3M GPE cells, respectively. (e–f) are the TEM images of SPAN after cycling in fully charged state for 2M and 3M GPE case, respectively.

Figure 5.18. The morphology of SPAN cathode before and after cycling regarding SPAN particles and SPAN cathode coated on carbon fibers. (a). The pristine SPAN particles. (b) and (c) are the SPAN cathode after cycling of 2M/3M GPE/bilayer Ta-LLZO case, respectively. (e–g) and (h–j) are the SPAN coated on the carbon felt current collector after cycling of 2M GPE/bilayer Ta-LLZO and 3M GPE/bilayer Ta-LLZO case, respectively. The scale bar of (e–j) is 5 μm. The S and N mapping are intentionally selected because they are representative elements of SPAN. The SPAN cathode samples coated on carbon felt were prepared by peeling off the SPAN from the outer part of the electrode so that the SPAN cathode coated on the carbon felt can be exposed.

Figure 6.1. The ATR-FITR spectroscopy regarding the thermal stability of LiFSI salt after the DME solvent is evaporated. Through the spectra, the LiFSI structure maintain perfectly without any bonding change compared with the pure pristine LiFSI, indicating there is no thermal runaway behavior happening through the drying process(2–4).

Figure 6.2. The electrochemical properties of pure LiFSI salt. (a). The Nyquist plot of a cell configuration of Stainless Steel (SS)/LiFSI/SS measured over the frequency range of 1MHz to 100 Hz and a voltage amplitude of 10 mV at different temperatures. The figure on the right is the zoomed-in version of the figure on the left. (b). The experimentally measured ionic conductivity of LiFSI and the ionic conductivity of other solid-state catholytes reported in literature. Ionic conductivity data for $Li_{2.3}C_{0.7}B_{0.3}O_3$ (LCBO), Li_6PS_5Cl (LPS-Cl), Li_6PS_5Br (LPS-Br), and Li_6PS_5I (LPS-I) were extracted from the references(5, 6). (c). The electrochemical stability window of LiFSI obtained by cyclic voltammetry with a carbon-felt/LiFSI+NGW^{TM}/bilayer-LLZO/Li-metal cell. The voltage range was 100 mV to 5 V with a scanning rate of 0.1 mV/second.

Figure 6.3. The schematics of the all-solid-state garnet type Li-S cells enabled by the novel three-phase cathode and bilayer-LLZO electrolyte architecture. The SPAN+NGW^{TM}+LiFSI composite cathode was obtained through melting the LiFSI in the SPAN+NGW^{TM}+LiFSI mixture and then cooled.

Figure 6.4. The optical image of three-phase cathode after heat treatment using carbon-black and NGW^{TM} as carbon source.

Figure 6.5. Characterizations of the all-solid-state garnet Li-S cell regarding the stability between SPAN and LiFSI and the morphology of cathode and cathode/LLZO interface. (a) and (b) are the XRD and ATR-FTIR pattern of the cathode materials in different conditions, respectively.

Figure 6.6. Morphology Characterizations of the all-solid-state garnet Li-S cell of the cathode and cathode/LLZO interface. Cross-section SEM images (a) of the interface between SPAN+NGW^{TM} cathode and bilayer LLZO, and (b) of the cathode with a cell configuration of SPAN+NGW^{TM}/bilayer-LLZO/Li-metal. Cross-section SEM images (c) of the interface between SPAN+NGW^{TM}+LiFSI cathode and bilayer LLZO, and (d) of the SPAN+NGW^{TM}+LiFSI cathode. Note that the LiFSI in these SEM images was simply mixed with SPAN+NGW^{TM} without heat treatment. Cross-section SEM images (e) of the interface between cathode and bilayer LLZO, and (f) of the cathode with a cell configuration of SPAN+NGW^{TM}+LiFSI (after heat treatment)/bilayer-LLZO/Li-metal.

Figure 6.7. The Nyquist plot of a cell configuration of (a) SPAN+NGW^{TM}/bilayer-LLZO/Li-metal. The ASR at both 22℃ and 60℃ are more than 250,000-ohm cm^2. (b) SPAN+NGW^{TM}+LiFSI mixture (without melting LiFSI)/ bilayer-LLZO/Li-metal with an ASR of 24,500-ohm cm^2 at 22 ℃ and 4800-ohm cm^2 at 60 ℃ . (c) SPAN+NGW(TM)+LiFSI composite (after melting LiFSI)/bilayer-LLZO/Li-metal with an ASR of 1400 ohm cm^2 at 22℃ and 433-ohm cm^2 at 60℃. The frequency ranges from 1MHz to 0.5 Hz and a voltage amplitude of 10 mV for all the tests.

Figure 6.8. The TEM images of the composite cathode: SPAN+NGW^{TM}+LiFSI (after melting LiFSI).

Figure 6.9. The electrochemical cycling of all-solid-state Li-S cell with a cell configuration of (a) and (b). SPAN+NGW^{TM}/bilayer LLZO/Li metal cells tested at 0.084 mA/cm^2 at 22℃ and 60℃, respectively. (c) and (d). SPAN+NGW^{TM}+LiFSI (without melting LiFSI)/bilayer LLZO/Li metal cells tested at 0.084 mA/cm^2 at 22℃ and 60℃, respectively.

Figure 6.10. Electrochemical performance of all-solid-state bilayer LLZO Li-S cells at 22 ℃ and 60 ℃. (a). The cycling performance tested at 0.084 mA/cm^2 at 22 ℃ over 200 cycles. (b). The rate performance at 60 ℃ under different current density of the all-solid-state garnet Li-S cell. 5 cycles were performed for each C-rate. (c) The voltage profile of the C-rate test. (d) and (e) The voltage profile and cycling performance of the all-solid-state Li-S cell tested at 60 ℃ at 0.167 mA/cm^2, respectively. (f). The cycling performance at 60 ℃ at a high current density of 0.84 mA/cm^2 (discharge)/0.334 mA/cm^2 (charge).

Figure 6.11. The all-solid-state garnet Li-S cell using carbon-black as carbon source and tested at a current density of 0.084 mA/cm^2 at 22 ℃.

Figure 6.12. Electrochemical and morphological characterizations of the all-solid-state garnet Li-S batteries tested at 0.167 mA/cm^2 at 60℃ (a). Electrochemical performances of the all-solid-state garnet Li-S battery over the entire cycling. The cell was stopped at 57th cycle due to a relative fast capacity decay from 41st to 57th cycle (blue region) compared with the first 40 cycles. (b). The SEM image captured at the composite cathode (top) and LLZO (bottom) interface of the all-solid-state Li-S cell after cycling.

Figure 6.13. (a). The voltage profile of the all-solid-state garnet Li-S cell tested at 0.84 mA/cm^2 (discharge current density)/ 0.334 mA/cm^2 (charge current density) at 60℃

under a sulfur mass loading of 1mg/cm^2. (b). The SEM image captured at the composite cathode (top) and LLZO (bottom) interface of the all-solid-state Li-S cell after cycling of (a).

Figure 6.14. The SEM image of a representee bilayer LLZO with a dense layer thickness of 45 μm and a porous layer thickness of 55 μm.

Figure 6.15. High-Energy-Density cell demonstration using 3D column LLZO architecture. (a) The schematics of 3D column LLZO enabled by direct ink writing. The column was printed directly onto the dense side of the bilayer LLZO. (b) The SEM (cross section and top view (insert)) images of the 3D column LLZO and the zoom-in SEM image of (b) to show the well-sintered bilayer LLZO architecture. The scale bars are 100 μm. (c) The XRD pattern of the 3D printed column LLZO architecture. (d) and (e) are the voltage profile and cycling performance respectively of the high-energy-density cell with a high sulfur mass loading of 7 mg/cm^2 tested at 60°C.

Figure 6.16. High sulfur loading (7 mg/cm^2) all-solid-state garnet Li-S cell enabled by the 3D LLZO bilayer architecture tested at 60℃ with current density of 0.35 mA/cm^2. (a) the cycling performance the all-solid-state garnet Li-S batteries (b). The voltage profile of the first cycle shown in (a).

Figure 6.17. Energy Density Comparison of the all-solid-state garnet Li-S batteries with the state-of-art garnet-based Li-S batteries. Note that the solid square/star and open square/star is for gravimetric energy density and volumetric energy density, respectively.

List of Abbreviations and Symbols

Li-S	lithium sulfur
Li	lithium
DMF	N,N-dimethylformamide
CE	columbic efficiency
S_8	elemental sulfur
Li-ion	lithium-ion
SPAN	sulfurized polyacrylonitrile
LTO	lithium titanate
LiTFSI	lithium bis(trifluoromethanesulfonyl)imide
DOL	1,3-Dioxolane
DME	1,2-Dimethoxyethane
SSEs	solid-state electrolytes
RT	room temperature
LLZO	$Li_7La_3Zr_2O_{12}$
NASICON	sodium ion super conductor
LiPON	lithium phosphorus oxynitride
Garnet electrolyte	garnet-type solid-state electrolyte
LLCZNO	Nb/Ca co-doped LLZO
SEM	scanning electron microscopy
EDX	energy dispersive X-ray spectroscopy
Ta-LLZO	Ta-doped LLZO
XRD	X-ray diffraction
XRF	X-ray fluorescent
XPS	X-ray photoelectron spectroscopy
ATR-FTIR	Attenuated Total Reflection-Fourier Transform Infrared Spectroscopy
IR	Infrared
%C	percent carbon
%N	percent nitrogen
TEM	Transmission Electron Microscopy
ToF-SIMS	Time-of-Flight Secondary Ion Mass Spectrometry
C	carbon
N	nitrogen
EIS	electrochemical impedance spectroscopy
DC	direct current
LGPS	$Li_{10}GeP_2S_{12}$
PEO	poly(ethylene oxide)
LiFSI	lithium bis(fluorosulfonyl) imide

$LiOH{\cdot}H_2O$	lithium hydroxide monohydrate
La_2O_3	lanthium oxide
ZrO_2	zirconium oxide
Ta_2O_5	tantalum oxide
CNT	carbon nanotube
KB	Ketjenblack
ALD	atomic layer deposition
ACN	Acetonitrile
ASR	areal specific capacity
NMP	N-Methyl-2-pyrrolidone
GPE	gel polymer electrolyte
SS	stainless steel
CEI	cathode electrolyte interface
PC	propylene carbonate
DMSO	dimethyl sulfoxide
EC	ethylene carbonate
DEC	diethyl carbonate
CSE	ceramic solid electrolyte
PAN	polyacrylonitrile
NGW™	graphene nanoribbon wire with trademark
MWCNTs	multi-walled carbon nanotubes
CVD	Chemical vapor deposition
CV	cyclic voltammetry
LCO	$LiCoO_2$
LCBO	$Li_{2.3-x}C_{0.7+x}B_{0.3-x}O_3$
HV	high voltage
σ	conductivity
R	total resistance of a given material
A	area of a given material
L	thickness of a given material

Chapter 1: Introduction to Li-S Batteries

Lithium-Sulfur (Li-S) batteries are secondary/rechargeable batteries. Historically, the first Li-S battery was invented and patented by Danuta Herbert and Juliusz Ulam in 1962(7), in which sulfur was used as an active redox material in the cathode, Li or Li-alloy was used as an anode and a saturated aliphatic amine was used as an electrolyte. In 1968, Bhaskara(8) improved the Li-S battery chemistry by using propylene carbonate (PC), γ-butyrolactone, dimethylsulfoxide (DMSO), and N,N-dimethylformamide (DMF) as organic solvents of the Li-S battery electrolyte. Consequently, the battery obtained an open circuit voltage of 2.35V–2.5V and an average discharge voltage of ~1.5–1.6V. In 1989, breakthrough work conducted by Peled et al.(9) demonstrated a primary Li-S battery using dioxolane/ether-based liquid electrolyte, although the columbic efficiency (CE) is lower than 90%. Dioxolane/ether-based liquid electrolyte is still among the most popular liquid electrolyte for Li-S batteries today.

1.1 Why Use Li-S Batteries?

The Li-S battery is becoming a very promising candidate for energy storage systems, especially when the elemental sulfur (S_8) is used as a cathode active material and Li metal is used as an anode. Sulfur chemistry has an exceptionally high theoretical energy density of 2600 Wh/kg and 2800 Wh/L, which is far beyond the energy densities of state-of-art Lithium-ion (Li-ion) batteries using oxide materials as the cathode and graphite/oxide materials/Li metal is used as the anode(10–13). At the same time, the Li-S battery represents a lower cost and more practical alternative to state-of-art Li-ion

batteries due to the low cost and high domestic availability of the sulfur material(10–13).

1.2 Sulfur Cathode Working Principles

There are two types of sulfur cathode reaction pathways. One is named “solid to liquid to solid” transition behavior while the other one is named “solid to solid” transition behavior.

1.2.1. Solid-Liquid-Solid Transition

Traditionally, the sulfur cathode undergoes the follow reaction pathways. During the discharge process, the S_8 will be reduced serially to Li_2S_8, Li_2S_6, Li_2S_4, Li_2S_2, and finally Li_2S. The Li_2S_8 and Li_2S_6 are called “long-chain” polysulfide, while the Li_2S_4 and Li_2S_2 are called “short-chain” polysulfide(14, 15). Note that the long-chain polysulfide is highly soluble in the ether-based liquid electrolyte (which will be discussed in section 1.4) and generates a liquid semi-product, while all other sulfur species (S_8, Li_2S_4, Li_2S_2, Li_2S) are insoluble. That is why this process is called “solid (S_8) to liquid (Li_2S_8, Li_2S_6) to solid (Li_2S_4, Li_2S_2, Li_2S)” transition process. During the charge process, the Li_2S will be oxidized into S_8 and theoretically achieve a specific capacity of 1670 mAh/g in terms of S_8. Figure 1.1 illustrates the voltage profile of Li-S batteries undergoing the “solid to liquid to solid” transition.

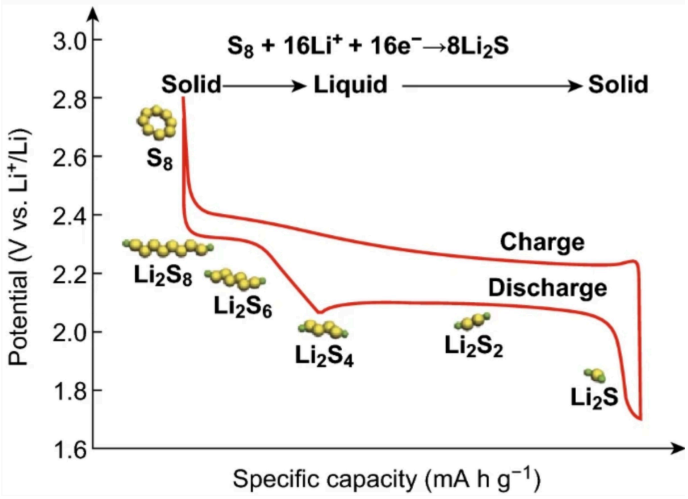


Figure 1.1. The schematic of the sulfur cathode working principle through "solid to liquid to solid" transition(16).

1.2.2. Solid-Solid Transition

In the 21st century, researchers found a new reaction pathway in Li-S batteries by using organic sulfur compounds such as sulfurized polyacrylonitrile (SPAN), small sulfur molecules(12, 13), and modifying the organic liquid electrolyte(17, 18). During the discharge process, instead of reducing S_8 to long-chain polysulfide and then to short-chain polysulfide and finally to Li_2S, the "solid to solid" transition process reduces S_8 to short-chain polysulfide and to Li_2S or directly to Li_2S without producing soluble long-chain polysulfide. During the charge process, the Li_2S is oxidized directly to S_8. Since there is no soluble sulfur species in the organic liquid electrolyte and all the generated products are solid species, this reaction pathway is defined as the "solid to solid" transition(19) shown in Figure 1.2.

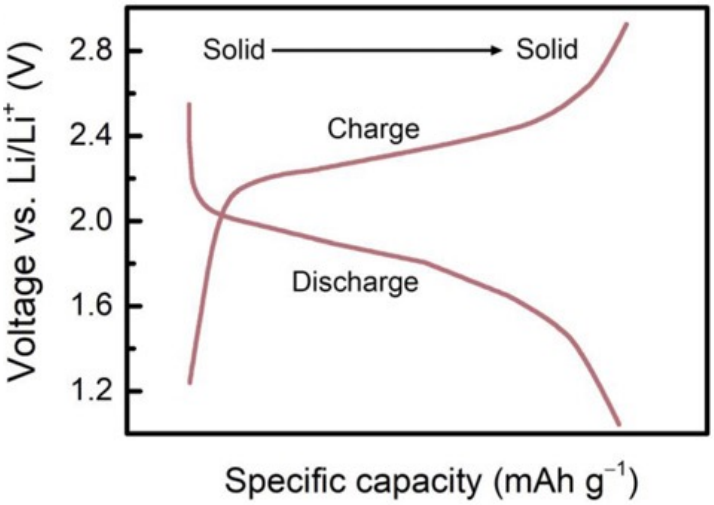


Figure 1.2. The schematic of the sulfur cathode working principle through "solid to solid" transition(19).

1.3 Anodes for Li-S Batteries

Generally, any material with a lower reduction potential than sulfur cathode could be used as an anode for a Li-S battery. The most popular anodes currently used for Li-based batteries are Li metal, graphite, and Lithium titanate (LTO). However, graphite and LTO are not commonly used for the Li-S battery. The graphite anode does not natively contain lithium and must be paired with a lithiated cathode such as Li_2S which requires huge activation process(20). In addition, the specific capacity of graphite (372 mAh/g) is less than $1/10^{th}$ the specific capacity of Li metal (3860 mAh/g), so a large mass of graphite must be used to match the sulfur cathode capacity and the battery energy density will be greatly reduced. For the LTO anode, the reduction potential of LTO (~1.5V vs. Li^+/Li)(21) is very close to the average discharge voltage of the sulfur cathode (1.7V to 2.1V vs. Li^+/Li)(22–24), and the specific capacity of LTO (175 mAh/g) is even lower than graphite. While LTO does not require a lithiated

cathode, a Li-S battery using a LTO anode will have very low energy density. Therefore, Li metal is a the most promising material for Li-S batteries due to its exceptionally high specific capacity which will lead to high-energy-density battery designs.

As mentioned in 1.3.1, although Li metal anode can lead to a high-energy-density battery design, it is limited by the possibility of Li dendrite growth issue(25), which causes battery shorting failure issues especially when testing the battery under high current density. In addition, the Li dendrite growth has been observed in both liquid electrolyte(26, 27) and solid-state electrolytes (SSEs)(28–31).

1.4 Organic Liquid Electrolytes

The most popular organic liquid electrolyte currently used in the Li-S batteries is 1M Lithium bis(trifluoromethanesulfonyl)imide (LiTFSI) in 1,3-Dioxolane (DOL) and 1,2-Dimethoxyethane (DME) with $LiNO_3$ additive. The $LiNO_3$ additive mitigates the long-chain polysulfide shuttling effect(32, 33), which is illustrated in the "solid to liquid to solid" transition reaction pathway. When the long chain polysulfides dissolved into the organic liquid electrolyte, it will generate a concentration gradient between the cathode and the anode. This concentration gradient drives the long-chain polysulfides to diffuse from the cathode to the anode, after which they react with the Li metal anode to form insulating short-chain polysulfide and Li_2S on the Li metal surface(34). During the charge process, those deposited sulfur species will simultaneously be electrochemically delithiated and lithiated on the Li metal surface, leading to abnormally large charge capacities, CE and fast capacity decay(35–39).

The majority of organic liquid electrolyte are highly flammable and does not prevent Li dendrite growth, although evidence in reducing the flammability and risk

of Li dendrite growth have been shown in highly concentrated electrolyte and fluorinated electrolytes(17, 18, 40, 41). Therefore, solid-state electrolytes to replace with organic liquid electrolyte to achieve safer Li-S batteries are among the most popular research areas recently.

1.5 Solid-State Electrolytes for Li-S Batteries

There are two main categories of SSEs used in Li-S batteries: polymer-based electrolyte and ceramic-based electrolyte. Although polymer-based electrolytes are flexible, light weight and are of low cost, they still possess safety issue because of their flammable nature and tendency to propagate Li dendrite growth(42). Only the most popular ceramic-based SSEs are discussed here which are sulfide-based SSEs and oxide-based SSEs.

1.5.1. Advantages and Disadvantages on Sulfide Electrolytes

Sulfide-based SSEs have a very high ionic conductivity at room temperature (RT) in the range of 1–10 mS/cm(5, 43–45) and they are the most thermodynamically compatible with the sulfur cathode(46–48). However, the disadvantages of sulfide-based SSEs for Li-S batteries are(48, 49): (1) they are very moisture sensitive and will react with H_2O to generate H_2S, which will cause severe environmentally issues if the batteries are not properly sealed; (2) they require an extremely high stacking pressure for battery operation; and (3) they show poor electrochemical stability against Li metal. The disadvantages of sulfide-based SSEs make it difficult to scale solid-state Li-S batteries to commercially relevant levels on the current techniques.

1.5.2. Advantages and Disadvantages on Oxide Electrolytes

There are a wide variety of oxide-based SSEs. For example, the lithium super ionic conductor (LISICON) exhibits a high ionic conductivity, but it is not stable against Li metal(50). The lithium phosphorus oxynitride (LiPON) is a typical thin-film type SSE that is stable with Li metal(51), though large scale production is expensive(52). The perovskite-type Li-ion conductor shows a wide electrochemically stability window, but it has a low ionic conductivity of 10^{-5} S/cm at RT and it is not stable against Li metal. Garnet-type SSE (garnet electrolyte), such as cubic $Li_7La_3Zr_2O_{12}$ (LLZO), is the most stable SSE against Li metal(53) and has high ionic conductivity (up to 10^{-3} S/cm at RT)(54, 55). As LLZO shows the most stability against Li metal compared with all other types of SSEs, it is the most ideal candidate for solid-state Li-S batteries using Li metal anodes.

1.6 Challenges of Li-S Batteries Using Garnet Electrolytes

Although the garnet electrolyte shows excellent chemical stability with Li metal, Li dendrite growth is still observed, likely due to Griffith flaws in the garnet electrolyte surface(56) that facilitate for interfacial cracking. This Li dendrite growth issue in garnet electrolyte was well resolved by our group using unique porous/dense/porous LLZO "trilayer" and dense/porous LLZO "bilayer" architectures(57–59). These electrolyte architectures significantly increased the electrode/electrolyte interfacial area and enabled an exceptionally high areal current density of 10 mA/cm^2 in a Li-Li symmetric cell without applied pressure(57). Although significant improvement has

been done in modifying the LLZO/Li anode interface(60–64), further work on stabilizing the sulfur/LLZO interface still needs to be done.

Chapter 2: Characterization Techniques

To comprehensively understand battery failure mechanisms and achieve stable cycling performance and high energy density, it is critical to characterize the physical, chemical, and electrochemically properties of the battery materials. X-ray diffraction (XRD) is a powerful tool to characterize crystal phase structure and phase purity of a given material. X-ray Fluorescence (XRF) is a non-destructive analysis tool to determine the elemental composition of a given material. SEM visualizes the morphological and topographical properties of materials, which is enhanced by EDX to visualize the elemental distribution for a given material. X-ray photoelectron spectroscopy (XPS) analyzes interfacial chemistry and is used to identify interfacial decomposition products that form during battery cycling. Time-of-Flight Secondary Ion Mass Spectrometry (ToF-SIMS) analyzes the 3D elemental distribution of a material at/below the material surface. Transmission Electron Microscopy (TEM) visualizes the morphology, topography, elemental distribution, and phase distribution of materials at nano-sized scales (<50 nm). Attenuated total reflection-Fourier transform infrared spectroscopy (ATR-FTIR) identifies the bonding vibrations of molecules and functional groups in a sample. Elemental analysis is specifically used to confirm the carbon (C) and nitrogen (N) content in the SPAN material. Electrochemical characterization of the batteries was carried out using galvanostatic and potentiostat programs, electrochemical impedance spectroscopy (EIS), and Cyclic Voltammetry (CV). This chapter will outline the fundamental working principles of

these characterization tools. All detailed parameters of characterization experiments will be discussed in section 4.

2.1 XRD

In 1913, the well-known Bragg's Law(65) (equation 2.1) was introduced to interpret the diffraction peaks created by constructive interface of X-rays reflected off parallel crystal planes in a given material.

$$n \times \lambda = 2d \times sin\theta \tag{2.1}$$

Where n is the diffraction order (measured in integer numbers), λ is the wavelength of the incident/reflected X-ray, d is the interspacing between the two parallel crystal planes reflecting the X-ray, and θ is the diffracted angle on a given crystal plane. When two parallel X-rays with a well-defined λ are reflected by two parallel atomic planes with an interspacing of d, the deeper beam travels an extra distance of $2d \times sin\theta$ if the two beams are in phase and will experience constructive interference. Since the wavelength λ of the X-ray source is fixed, the diffraction angles θ of the various diffraction peaks are used to obtain the corresponding interspacing d, which are then used to identify the crystal phase and calculate the lattice parameter(s).

2.2 XRF

When high-energy X-rays (higher than the binding energy of an atom, typically higher than the binding energy of K or L shell in an atom) irradiate samples, the electron of an atom in the sample will be dislodged. The electron vacancy left will

be filled by another electron from a higher energy orbital shell of that atom. This electron dropping off behavior from high energy state to low energy state releases a fluorescent X-ray. The XRF measures this energy to determine the elemental composition in a sample.

2.3 SEM and EDX

When a high energy (up to 40 keV) electron beam hits a sample under vacuum, secondary electrons, back scattered electrons, and characteristic X-rays are generated that are collected by the SEM detectors. These collected signals are translated into images representing the morphological and topographical properties of the samples. Secondary electrons are generated when the incident electron beam interacts with the electron cloud of the sample atoms and transfers enough energy to eject some of these bound electrons. Higher energy bound electrons then relax to fill the resulting unoccupied electron states, releasing characteristic X-rays in the process. The characteristic X-rays are used to identify different elements inside the sample, which is the working principle of EDX. Elemental mapping of EDX can provide spatial distributions of different elements in the samples. Back scattered electrons are generated when electrons from the incident electron beam repeatedly scatter off the electron clouds of the sample atoms and are eventually redirected back out of the sample. Scattering occurs more often when interacting with larger atomic number elements with more bound electrons and sample regions of higher atomic density, so back scatter electrons are used to visualize the mass density distribution of the sample.

2.4 ToF-SIMS

ToF-SIMS is a surface-sensitive analysis tool used to analyze the 3D elemental distribution of the sample. A focused ion beam generally consisting of Ga^+ ions is directed towards the sample and ablates material from the sample surface. This ablated material is composed of individual atoms or multi-atom fragments, some of which become ionized by the focused ion beam. The ToF-SIMS detector uses voltage biases to attract either positively or negatively charged fragments towards the detector and uses the travel time to calculate the fragment mass. By repeatedly scanning the focused ion beam over the same area of the sample, each scan will analyze the elemental distribution at different depths and provide the 3D elemental distribution of the sample. While the elemental surface-sensitivity is lower than that of XPS, the ability to gain 3D elemental information of a specific area on the sample ensures that ToF-SIMS is incredibly useful for analyzing battery materials.

2.5 TEM

For TEM, the incident electron beam is accelerated to an extremely high voltage of 200 kV to minimize the wavelength of the accelerated electrons and allow imaging at near-atomic scales. Unlike SEM, the TEM incident electron beam fully penetrates through the sample to minimize multi-scatter events that reduce image resolution. As a result, TEM samples are polished to thicknesses less than 100 nm using mechanical polishing or ion milling, with special care taken to avoid introducing damage artifacts into the TEM sample. The transmitted electrons are used to visualize the sample topology and analyze the elemental distribution of the sample. The TEM electromagnetic lens can be adjusted so the incident electron beam diffracts through

the sample and produces a diffraction pattern. By selecting a specific diffraction spot, the image of the sample topology will highlight only areas with crystal phases that contribute to the selected diffraction spot.

2.6 XPS

XPS is based on the photoelectric effect discovered by Einstein in 1905, where x-rays of sufficient energy are absorbed by atoms in a sample and emit electrons with a range of energies. By comparing the energy of the original x-rays with the kinetic energies of the emitted photoelectrons, the binding energy associated with each photoelectron can be calculated. While different elements/compounds can have overlapping binding energies, it is generally possible to identify the materials represented by the binding energy peaks in the XPS spectra. Since high energy photons such as x-rays are easily absorbed by surface layer atoms, XPS is an incredibly surface technique for analyzing surface chemistries and providing quantitative analysis of bonding covalency for a given material surface.

2.7 ATR-FTIR

In FTIR, an IR beam is directed at the sample and the sample absorbs/emits specific IR frequencies that match the vibrational modes of molecules in the sample. By attributing each peak in the FTIR spectra to a specific bond type, the internal bonding structure of the sample can be quantified. ATR is the most commonly used sampling methodology for FTIR and is very helpful for analyzing thick sample. As a result, ATR-FTIR is the most used technique to characterize the bonding structure of

samples due to the ease of sample preparation, high detection accuracy and sensitivity, and high measuring speed.

2.8 Elemental Analysis

Elemental analysis occurs after the sample is combusted at 950 °C in an oxygen rich environment. Carbon from the sample is converted to CO_2 that absorbs photons at specific wavelengths within the IR spectrum. An increase in the concentration of CO_2 will increase the amount of absorbed IR energy and change the detector voltage output. Nitrogen from the sample is converted to NOx gas that is reacted with reagents to produce nitrogen gas (N_2). Nitrogen gas has a lower thermal conductivity compared to the instrument's helium carrier gas. Therefore, increased concentrations of N_2 gas will increase the temperature of a tungsten wire filament cell that the combustion gases are flowed across. Analytical results are reported as percent carbon (%C) and percent nitrogen (%N) and calculated from weight of the sample placed inside the tin cup prior to combustion. Moisture content is not determined. The elemental analysis is used to confirm the sulfur wt.% of the SPAN used in the studies.

2.9 Electrochemical Techniques

2.9.1. Battery Cycling Techniques

In galvanostatic mode, a varying voltage is applied to the Li-S battery to give a constant cycling current (positive for charging, negative for discharging), with the voltage increasing/decreasing as the Li-content of the S electrode decreases/increases. In potentiostatic mode, a constant voltage is applied to the Li-S battery and the current is a function of voltage based on Bulter-Volmer model.

2.9.2. EIS

During EIS, an AC voltage input signal is applied to the Li-S battery to produce an AC current output signal. By comparing the magnitude and relative phase of the voltage and current signals, the real and imaginary impedance of the Li-S battery can be calculated. By testing at a range of frequencies, an EIS impedance spectrum is measured that carries information about different kinetic processes within the sample. A DC voltage can be applied to shift the Li-S battery away from equilibrium and obtain impedance spectra under different conditions.

2.9.3. CV

CV is a potentiodynamic electrochemical testing program that provides kinetic and thermodynamic information on the electrochemical reactions of the electrodes. During the CV measurement, the working electrode potential is scanned linearly with respect to time and the resulting current is measured. In the CV plot, whenever there is a peak in current, it indicates an electrochemical reaction took place at that voltage.

Chapter 3: Research Objectives

In garnet Li-S batteries, it was understood that all sulfur species except for Li_2S are thermodynamically unstable with LLZO (Figure 3.1). However, Fu et al. has shown that a self-inhibiting solid-liquid electrolyte interface (SLEI) can be formed between the sulfur cathode and LLZO to prevent the cathode side reactions when using a Nb/Ca co-doped LLZO (LLCZNO) garnet electrolyte(66).

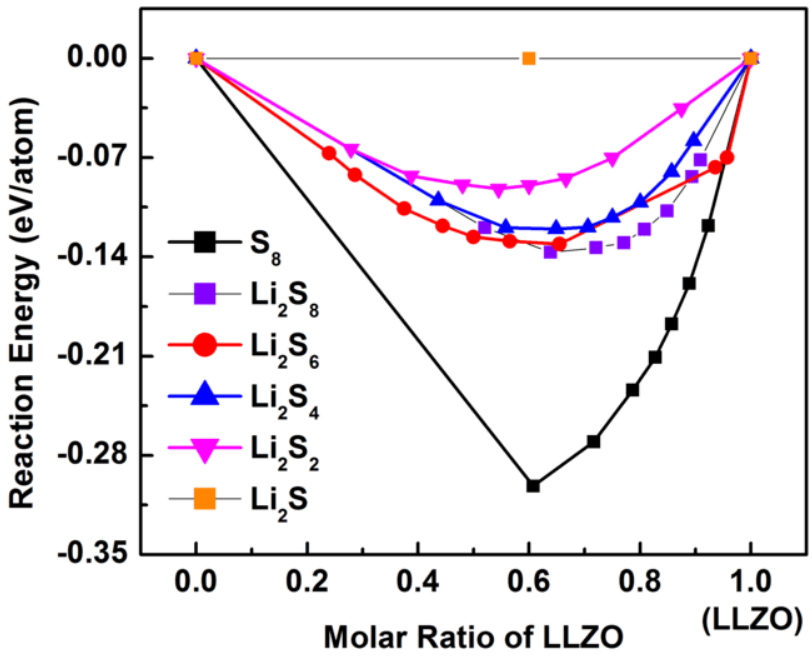


Figure 3.1. The thermodynamic stability of different sulfur species with pure cubic phase LLZO. All sulfur species except Li_2S are thermodynamically unstable with LLZO, which can cause continuous reaction between the sulfur cathode and LLZO in long-term cycling.

Another critical challenge in garnet Li-S batteries is the large sulfur volume expansion during lithiation (~78%)(67, 68), which causes loss of contact with the

electronically conductive additives and current collectors. To overcome this, our group infiltrated the sulfur cathode into the porous layer of bilayer (porous/dense)/trilayer (porouse/dense/porous) garnet structure to help maintain contact with the sulfur cathode during volume expansion and allowed successful cycling of garnet Li-S batteries(58, 69). Our previous garnet Li-S results(57, 58, 70) demonstrated stable cycling using LLCZNO. With the bilayer/trilayer structures, our group has achieved a high current density of 10 mA/cm^2 at RT and with no applied pressure in Li-Li symmetric cells(57). However, the high relative density of the LLZO electrolyte added additional mass to the cells and decreased the gravimetric energy density. Therefore, we introduced a new cell configuration to achieve high specific capacity and high energy density. For this dissertation, we used a thin bilayer garnet (porous/dense) structure in which the pores were filled by Li metal while the sulfur cathode is on the dense side of the bilayer.

The Ca dopant in LLCZNO can segregate and form regions of Ca-rich secondary phase, as shown in the Scanning Electron Microscopy (SEM) and Energy dispersive X-ray spectroscopy (EDX) in Figure 3.2. This may generate current density hot spots at the LLCZNO/Li metal interface that can lead to Li dendrite growth if no protective layer exists(64), and can reduce the ionic conductivity of the LLCZNO (71). It was also found that the Nb dopant can be reduced by Li metal(72). Therefore, Ta-doped LLZO (Ta-LLZO) was chosen as the garnet electrolyte for all the studies in this dissertation due to the better stability of Ta-LLZO with Li metal compared to other popular dopants, such as Al and Nb (72–74).

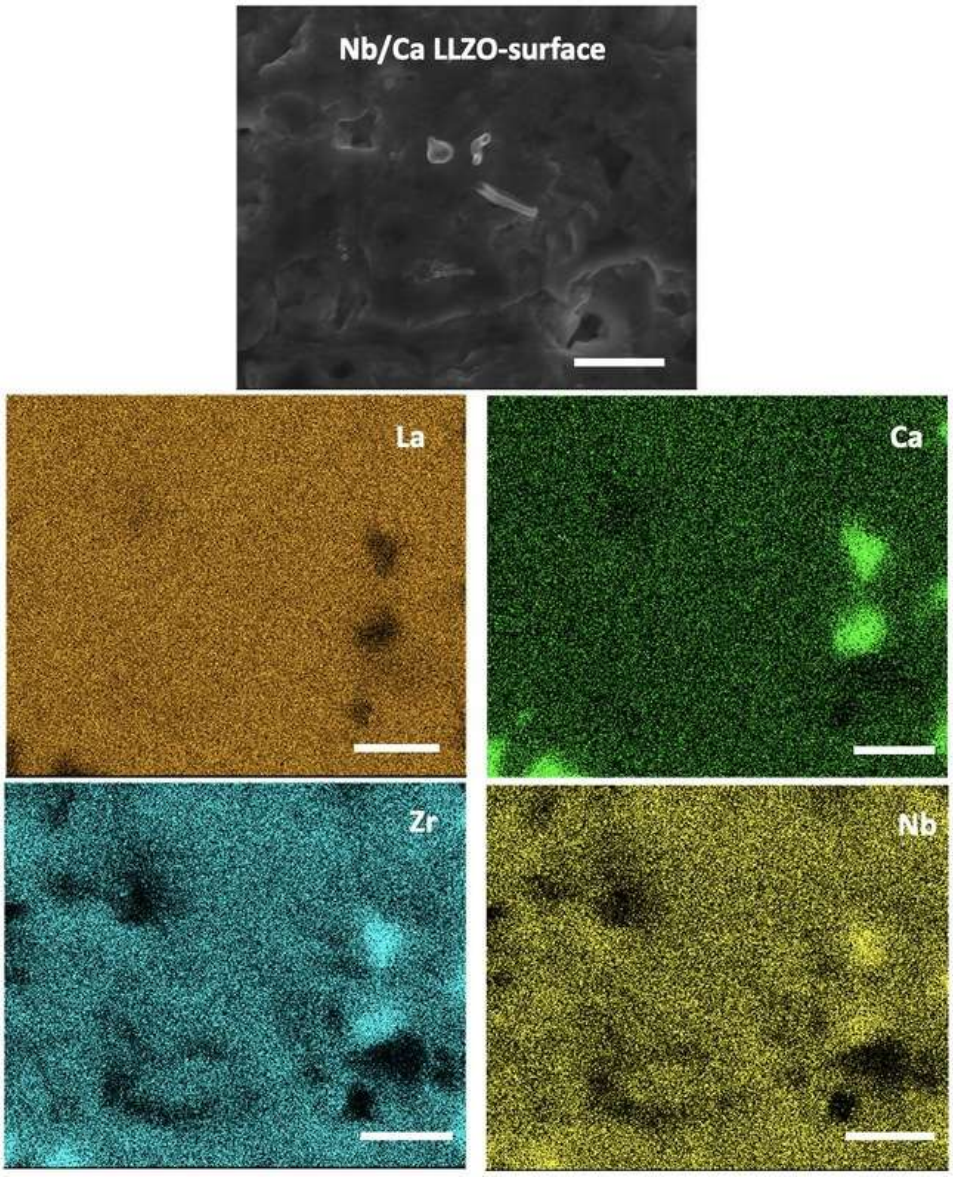


Figure 3.2. The SEM images (top view)/EDX mapping of Ca/Nb co-doped LLZO. The La segregation can be eliminated by Ca dopant partially occupation in the La site. The scale bar is 5μm.

Although Ta-LLZO is the most stable type of LLZO with Li metal, we observed a charge fluctuation issue in Li-S cells using Ta-LLZO electrolyte when cycled at 0.03C (1C = 1670 mA/g), as shown in the voltage profile in Figure 3.3. As 0.03C is equal to 0.2 mA/cm^2 and should be far below the critical current density of bilayer

LLZO(59). Further research is required to better understand the sulfur-cathode/LLZO interface and resolve this issue to have a workable Li-S cell using garnet electrolyte.

.

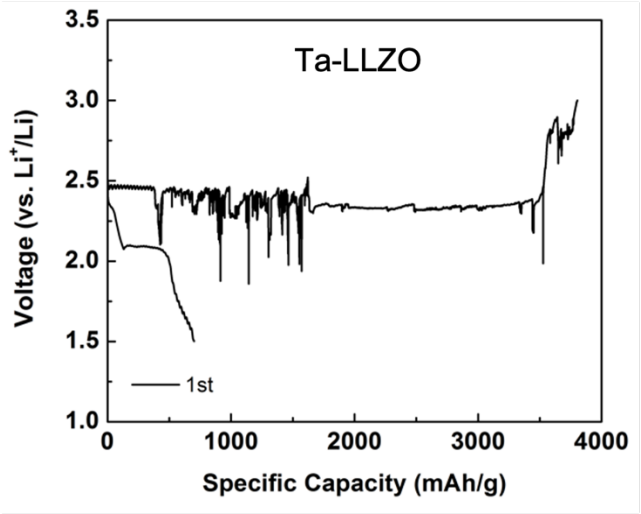


Figure 3.3. The voltage profile of garnet Li-S cell tested at 0.03C at RT under a sulfur mass loading of 4 mg/cm^2 using the normal stoichiometric Ta-LLZO ($Li_{6.75}La_3Zr_{1.75}Ta_{0.25}O_{12}$).

This dissertation reflects studies on (i) garnet-type Li-S battery failure mechanism analysis resulted from the sulfur-cathode/Ta-LLZO interface; (ii) the resolution on addressing the Li-S battery failure and the methods on how to achieve stable cycling with good energy density; (iii) the revolutionary design of "all-solid-state" Li-S battery using garnet electrolyte which has never been reported in the battery field until now. Specifically, the proof-of-concept of the all-solid-state battery design was first discussed and then focus on high-energy-density all-solid-state Li-S battery design using garnet electrolyte through the method of direct ink printing that was previously developed by our lab(75).

Chapter 4: Stabilizing Sulfur Cathode/Garnet Electrolyte Interface to Achieve High Energy Density Using 3D Asymmetric Electrolyte Architecture

4.1 Introduction

As discussed in the chapter 1 that solid-state Li-S batteries are one of the most promising candidates for next generation energy storage technologies due to the low cost and high domestic availability of sulfur, the exceptionally high theoretical energy density of a Li-S (2600 Wh/kg and 2800 Wh/L)(10, 13, 33, 76, 77), and the potential for suppression of the polysulfide shuttle, Li dendrite growth, low coulombic efficiency, and short circuiting in more conventional liquid electrolyte Li-S batteries (35–39). The most popular SSEs in Li-S battery field are $Li_{10}GeP_2S_{12}$ (LGPS) and Li stuffed garnet type LLZO with a space group of $Ia\bar{3}d$ (47, 78, 79). LLZO is a highly promising SE for Li-S batteries due to its reasonably high ionic conductivity (0.1–1 mS/cm) at RT and excellent chemical stability with Li metal(80) and does not generate any toxic gases when it exposes to air and moisture, compared with sulfide-based SSEs. In addition, with a bilayer/trilayer structure, our group has achieved a high current density of 10 mA/cm^2 at RT and with no applied pressure in Li-Li symmetric cells(57). However, according to Chapter 3, there are still challenges that need to be resolved at the sulfur-cathode/Ta-LLZO interface.

To investigate the charge failure issue in Chapter 3, herein we systematically studied the elemental sulfur cathode and Ta-doped LLZO (Ta-LLZO) interface. Our results show that without the buffer layer on the cathode side, the integration of sulfur

cathode onto the Ta-LLZO dense garnet leads to an infinite long-time charge issue. The results further show a strong indication this is due to lanthanum segregation to the surface of Ta-LLZO. To overcome this challenge, a thin Poly(ethylene oxide) (PEO)-based interlayer is applied to stabilize the sulfur cathode/Ta-LLZO interface. The PEO-based interlayer not only physically separates the sulfur cathode and the Ta-LLZO bilayer surface, but also can accommodate the stress/strain generated from sulfur volume expansion that may lead to micro-cracks in the Ta-LLZO. On the anode side, an ultra-thin ZnO layer was coated by atomic layer deposition (ALD) on the porous side of the 3D asymmetric bilayer Ta-LLZO to obtain conformal Li/Ta-LLZO contact(81). When these approaches were combined, we were able to obtain a high sulfur mass loading of 4 mg/cm^2 with a high initial discharge capacity (1307 mAh/g) at RT corresponding to an energy density of 639 Wh/L and 134 Wh/kg, and stable long-term cycling with no applied pressure. By simply reducing the LLZO dense layer thickness to 10 μm as we have previously demonstrated(70), a significantly higher energy density of 1308 Wh/L and 257 Wh/kg is achievable.

*4.2 **Experimental***

La excess, La deficient and normal stoichiometrically LLZO sample synthesis: The La excess and La deficient Ta-LLZO samples were prepared by milling stoichiometric amount of lithium hydroxide monohydrate ($LiOH{\cdot}H_2O$, Alfa Aesar), tantalum oxide (Ta_2O_5, Alfa Aesar), zirconium oxide (ZrO_2, Inframat Advanced Materials) with 1wt%, 3wt% and 5%wt extra/deficient preheated lanthanum oxide (La_2O_3, GFS Chemistry). Then the powders were calcined at 900 °C for 10 hrs in a magnesium oxide crucible. The 3D solid electrolytes bilayers were prepared using the method previously reported by us(81) using Ta-doped LLZO and LLCZNO. The sintering temperature for both Ta-LLZO and LLCZNO is 1100℃.

Battery Materials Preparation: All the liquids were dried in 4 Å molecular sieves (Millipore Sigma) for at least two days before use. The PEO (Mwt. = 600,000, Millipore Sigma), LiFSI (99.9%, Alfa Chemistry) and carbon nanotube (CNT, Carbon Solution, Inc.) were dried at 60°C, 120°C and 95°C under vacuum for 24 hrs before use, respectively, to avoid moisture contamination. Poly(Ethylene Oxide) (PEO) and lithium bis(fluorosulfonyl) imide (LiFSI) (EO: Li^+ = 15:1) were dissolved in the acetonitrile (ACN, anhydrous, Millipore Sigma) and stirred at 40°C to ensure good mixing. The obtained PEO/LiFSI solution concentration was 0.03 g/mL. The S_8 (Millipore Sigma) and Ketjenblack (KB, H.M. Royal Inc.) were mixed in the carbon disulfide (anhydrous, Millipore Sigma), followed by ultrasonic stirring at RT for 3 hrs before use. The concentration of the binder-free cathode suspension was 0.2 g_S/mL and 12 mg_{KB}/mL. All preparations were performance in an Ar-filled glovebox with O_2 < 0.01 ppm and H_2O < 0.25 ppm.

Electrochemical Cell Preparation: First, lithium carbonate removal was done for the prepared bilayer in a tube furnace at 800°C for 2 hrs under inert gas atmosphere. Then thin ZnO ALD layers were coated on both sides of the bilayer Ta-LLZO at 112°C. On the anode side, surface-cleaned molten lithium was infiltrated into the porous side of the bilayer structure within a few seconds due to the ultra-thin ZnO ALD layer and capillary force. On the cathode side, 40 μL of the PEO solution was uniformly drop-cast on the dense side of the bilayer Ta-LLZO with an area of 1 cm^2, followed by vacuum drying at RT and then drying at 70°C to achieve a total thickness of ~8.4 μm. After that, the CNT and cathode suspension was applied on top of the PEO-based solid membrane to obtain a high sulfur mass loading of 4 mg/cm^2, followed by further heating at 120°C for ~2 min to ensure the elemental sulfur was uniformly coated. Finally, 1M LiFSI DME liquid electrolyte was drop coated on top of the cathode side. The cells without PEO-based interlayer were prepared in the same recipe, but just without drop casting the PEO solutions on the dense Ta-LLZO surface.

Electrochemical Measurement: 2032 type coin cells were used for all the electrochemical performance measurements at RT. All cycling tests were performed by an Arbin instrument BT 2000. The EIS measurements were performed using a Bio-logic VMP3 potentiostat over the frequency range of 1 MHz to 1 Hz with an amplitude of 10 mV.

Characterizations: SEM and EDX images were captured with a Tescan GAIA FEG SEM. XRD was performed on a C2 Discover diffractometer (Bruker AXS) with a Cu K_α radiation source (λ = 1.54056 Å) at 40 kV and 40 mA. The ALD thickness was characterized by Auto ELIII Ellipsometer. The lanthanum and zirconium mass ratio

was quantified using x-ray fluorescence measurements (XRF, Bruker Ranger), which were carried out under vacuum between 6.5 and 35 keV. The XRF data was analyzed using Spectra EDX software. Results were normalized to the nominal amount of zirconium in the LLZO (fixed at 1.75 moles per formula unit). For XPS measurement, all the samples were brought into He-filled glove box prior to any measurements. The atmosphere was kept < 0.1 ppm O_2 and < 0.0 ppm H_2O. The samples were loaded on ca. 2 cm diameter puck with Cu tape and transferred to XPS chamber without air exposure using air-tight transfer vessel. XPS spectra were acquired with the Kratos Axis UltraDLD[1] using monochromatic Al Ka (10 mA, 15 kV). XPS scans were carried out at 20 eV pass energy. Prior to depth profiling, the puck was taken out from the XPS chamber and transferred to He-filled glove box in N_2 atmosphere. The samples were loaded on a ca. 15 cm bar to provide enough distance between the samples to avoid cross contamination. The sample bar was brought to XPS in He atmosphere and was transferred to XPS. The container was briefly opened in the lab, while the sample bar was loaded into the antechamber, resulting in an air exposure for less than 1 min. XPS depth profiling was carried out with Ar^+ gun with an energy of 2 kV over a raster area of 6 mm × 6 mm. XPS was collected after 10 min, 20 min and 40 min of sputtering time. Charge neutralizer (filament current 1.8 A, charge balance 2.5 V) was used during the measurements. XPS spectra were analyzed with CasaXPS(82). The spectra were referred to C 1s peak of hydrocarbon at 284.5 eV(83). Tougaard-type background was subtracted before deconvolution and analysis of the peaks. The area ratios of peaks

[1] Certain commercial equipment, instruments, materials, suppliers, or software were identified in this paper to foster understanding. Such identification does not imply recommendation or endorsement by the National Institute of Standards and Technology, nor does it imply that the materials or equipment identified are necessarily the best available for the purpose.

were fixed to its theoretical area ratio of their degeneracy with the same full width at half maximum. S $2p_{3/2}$ and S $2p_{1/2}$ peak separation was kept consistent at 1.18 eV[42] for all peaks. The ToF-SIMS was performed on a Ga^+ focused ion beam (FIB)/SEM (Tescan GAIA3) equipped with ToF-SIMS. The typical analyzed area was 20 μm × 20 μm with an accelerated voltage and beam current of the ToF-SIMS of 30kV and 1900 pA, respectively.

Computational Methods: We considered the interfaces between La_2O_3 and different sulfur species, as well as different sulfur species and LLZO as a pseudobinary and determined the most thermodynamically stable phase equilibria, as in previous work (84). We normalized the compositions of the sulfur species, La_2O_3, LLZO and Li salts to one atom per formula unit, respectively. The reaction energies shown in Figure 1.3 and 4.2, reflect the energy of decomposition of the pseudobinary to the stable phase equilibria at each molar ratio. The energies for the materials used in our study were obtained from the Materials Project database(85).

Finite element modeling: Finite element modeling was performed using SolidWorks 2020 package. Samples with dimension of 100 μm in thickness, 5 mm in length, and 3mm in width were created. The mechanical properties of LLZO and PEO were taken from literatures(86–89). 3-point bending models were applied on the samples (Figure 4.1) with a bending force of 0.1N applied. Stress and strain distributions were observed.

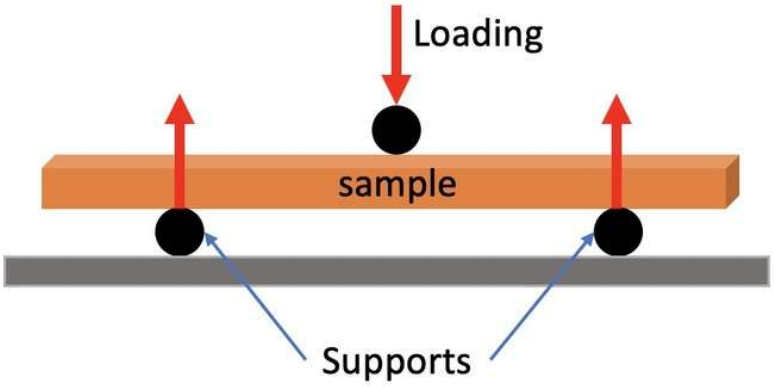


Figure 4.1. Schematic of the 3-point bending model for mechanical properties investigation.

4.3 Results and Discussions

4.3.1 La Segregation Impacts on Cell Failure

We observed in sulfur cathode/liquid electrolyte/Ta-LLZO (ZnO ALD coated)/Li metal cell configurations, large voltage fluctuations during charging and a total charge capacity exceeding the theoretical value of sulfur (1670 mAh/g) in Figure 4.2a. Subsequently, only 700 mAh/g discharge capacity was achieved at 0.03C in the first cycle.

To investigate this degradation, XRD, SEM and EDX mapping were applied to study the surface composition and morphology of Ta-LLZO. It was found that in stoichiometric Ta-LLZO, La segregation is observed (Figure 4.2e).

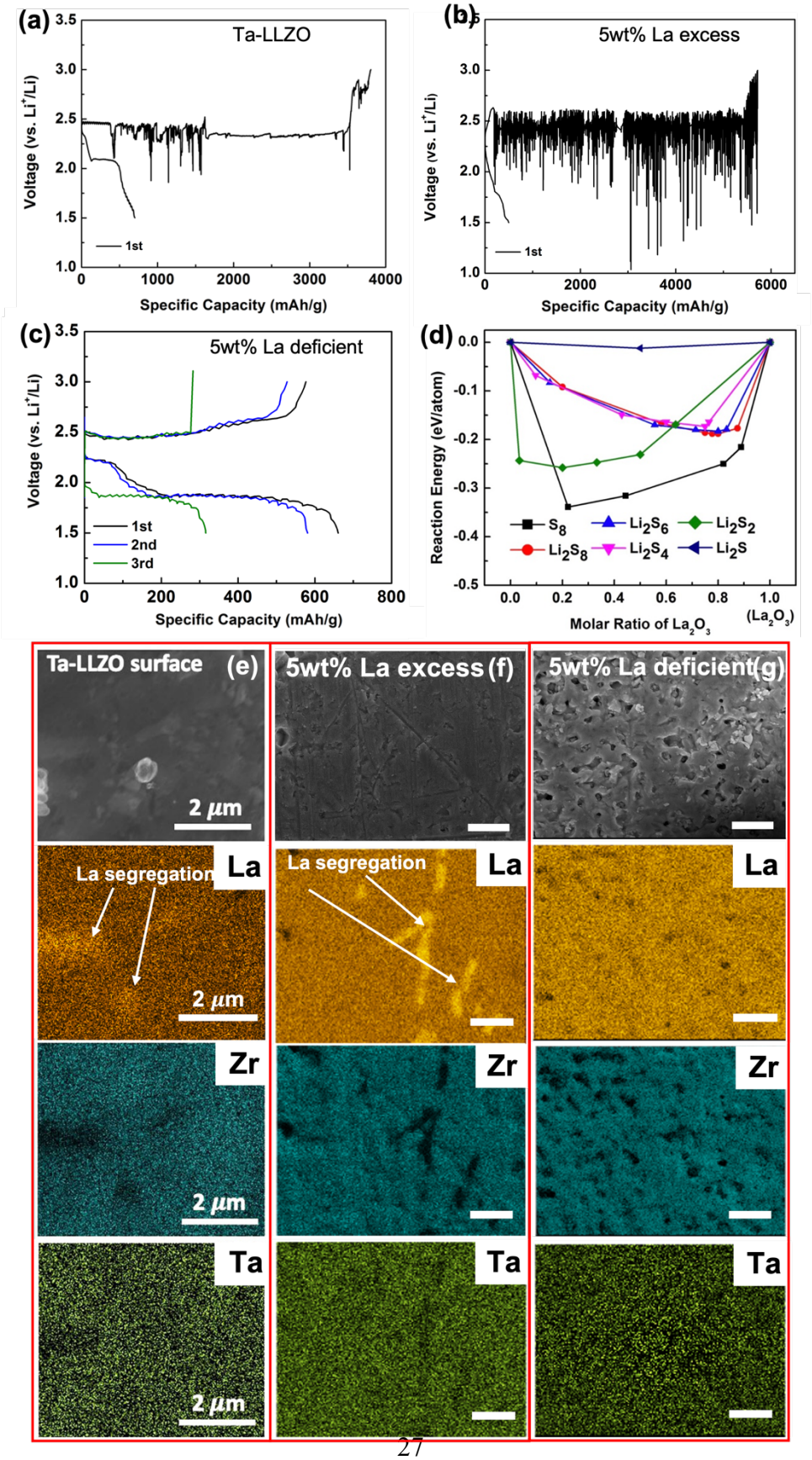

(a)
Ta-LLZO
Voltage (vs. Li+/Li)
Specific Capacity (mAh/g)
1st
(b)
5wt% La excess
Voltage (vs. Li+/Li)
Specific Capacity (mAh/g)
1st
(c)
5wt% La deficient
Voltage (vs. Li+/Li)
Specific Capacity (mAh/g)
1st
2nd
3rd
(d)
Reaction Energy (eV/atom)
Molar Ratio of La2O3
(La2O3)
S8
Li2S6
Li2S2
Li2S8
Li2S4
Li2S
Ta-LLZO surface
(e)
5wt% La excess
(f)
5wt% La deficient
(g)
2 μm
La segregation
La
Zr
Ta

Figure 4.2. La segregation indications on cell failure. (a). The voltage profile of garnet Li-S cell tested at 0.03C at RT using the normal stoichiometric Ta-LLZO. (b) Voltage profile of garnet Li-S cell tested at 0.03C at RT using the 5wt% La excess Ta-LLZO. (c) Voltage profile of garnet Li-S cell tested at 0.03C at RT using 5wt% La deficient Ta-LLZO. (d). The calculated mutual reaction energy of pseudo-binaries of different sulfur species and La_2O_3. (e) The SEM and EDX mapping images of the Ta-LLZO (normal stoichiometry, top view) showing the La segregation. (f) SEM (top view) and EDX mapping images of the 5wt% La excess Ta-LLZO. (g). SEM (top view) and EDX mapping images of the 5wt% La deficient Ta-LLZO. The scale bar for (f) and (g) is all 10 μm.

To determine if La segregation causes the voltage fluctuation during charging, La-excess (1wt%, 3wt% and 5wt%) and La deficient (1wt%, 3wt% and 5wt%) Ta-LLZO using the same cell configuration were tested. For the La-excess Ta-LLZO, the XRD patterns (Figure 4.3a) showed a La_2O_3 impurity was formed in all three samples and their corresponding SEM and EDX mapping images (Figure 4.3b and Figure 4.2f) showed La segregation on the Ta-LLZO surface indicating that the La segregation phase is La_2O_3. For the La-deficient Ta-LLZO, the XRD patterns (Figure 4.4a) showed an impurity phase of $La_2Zr_2O_7$ in 1wt% and 3wt% La deficient the samples, while it showed a cubic garnet phase in 5%wt Ta-LLZO without impurity, and their corresponding SEM and EDX mapping images (Figure 4.4b and Figure 4.2g) showed that the there is no La segregation in the 5%wt La deficient Ta-LLZO samples. The amount of La in the La excess and La deficient samples was experimentally verified through X-ray Fluorescence (XRF) shown in Table 4.1. The measured XRF data is very consistent with the nominal La content.

Table 4.1. Summary of the XRF results on the sintered La excess/deficient samples

Designed La wt % Additions/Subtractions	Designed La (mol in $Li_xLa_yZr_{1.75}Ta_{0.25}O_{12}$)	Measured La wt%	Measured Zr wt %	Measured La (mol in $Li_xLa_yZr_{1.75}Ta_{0.25}O_{12}$)
+5	3.14	72.9%	27.1%	3.12
+3	3.08	72.7%	27.3%	3.08
+1	3.02	72.2%	27.8%	3.01
-1	2.96	72.0%	28.0%	2.98
-3	2.90	71.4%	28.6%	2.89
-5	2.84	71.2%	28.8%	2.86

Therefore, the 5%wt La excess and 5%wt La deficient Ta-LLZO were used for Li-S cells assembly (Figure 4.2b and 4.2c) to evaluate the La segregation effect. The 5%wt La excess Ta-LLZO cell (Figure 4.2b) showed the same charge voltage fluctuation issue as the normal stoichiometry Ta-LLZO (Figure 4.2a). While rapid voltage drops can be due to shorting, these voltage fluctuations are likely due to the thermodynamically favorable reaction between different sulfur species and La_2O_3 associated with the La segregation (Figure 4.2d and Table 4.2) which can lead to the cell degradation and failure. This is further confirmed by the 5%wt La deficient Ta-LLZO which does not have La segregation and shows a normal charge/discharge voltage profile (Figure 4.2c) without any rapid voltage drops. The lower capacity is most likely due to the lower conductivity (10^{-5} S/cm, Figure 4.5) of the 5%wt La deficient Ta-LLZO. These results strongly imply that La surface segregation plays a significant role in Li-S cell stabilization.

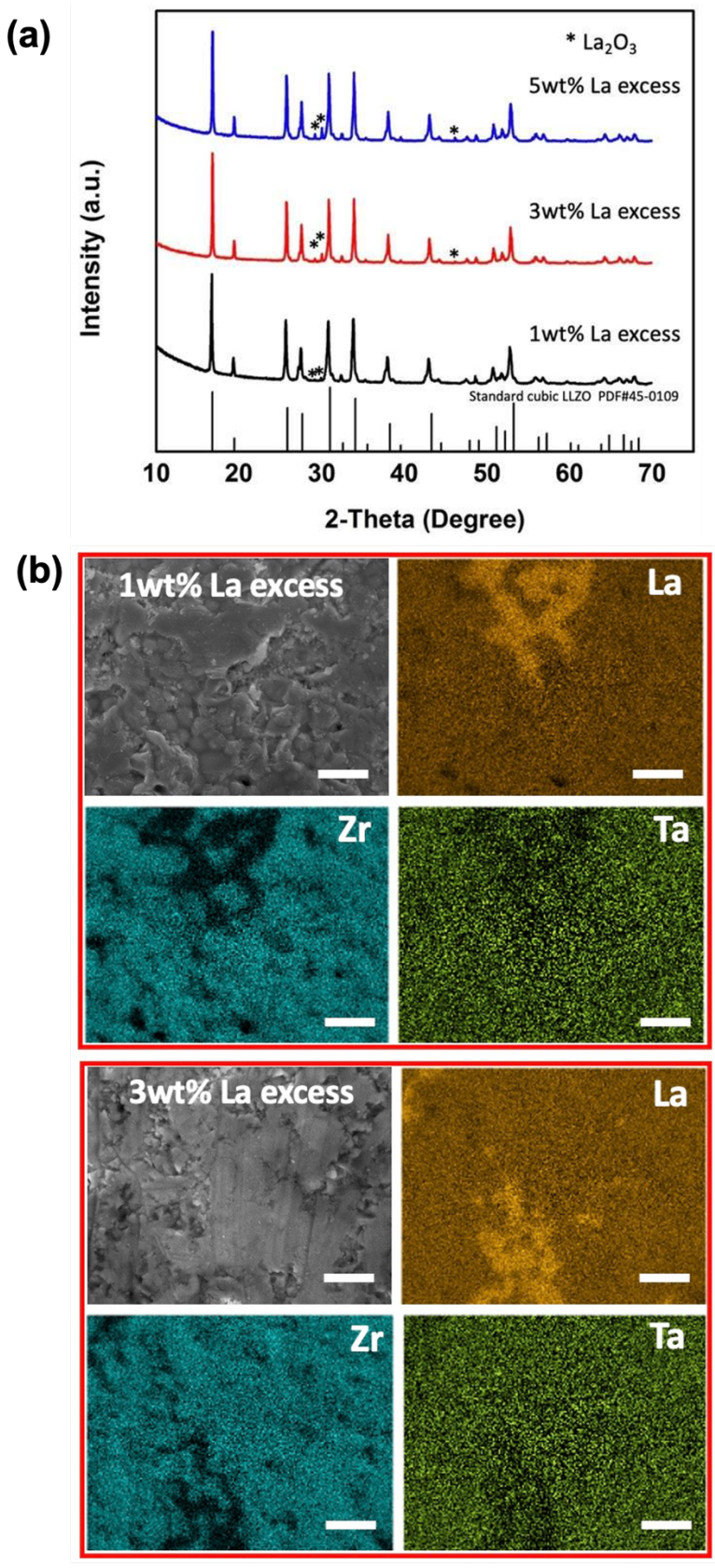

(a)
* La_2O_3
5wt% La excess
3wt% La excess
1wt% La excess
Standard cubic LLZO PDF#45-0109
Intensity (a.u.)
10
20
30
40
50
60
70
2-Theta (Degree)
(b)
1wt% La excess
La
Zr
Ta
3wt% La excess
La
Zr
Ta

Figure 4.3. La excess Ta-LLZO sample characterizations. (a). The La excess Ta-LLZO XRD pattern. When different amount of extra La is added, the impurity phase of La_2O_3 is observed in all the samples. The impurity intensity goes higher when more La element is added in the Ta-LLZO. (b). The SEM images (top view)/EDX mapping of La excess Ta-LLZO with different amount of La excess. Both show La segregation. Combined with the XRD results, it is indicated that the La segregation phase is the La_2O_3. The scale bar is all 10 μm.

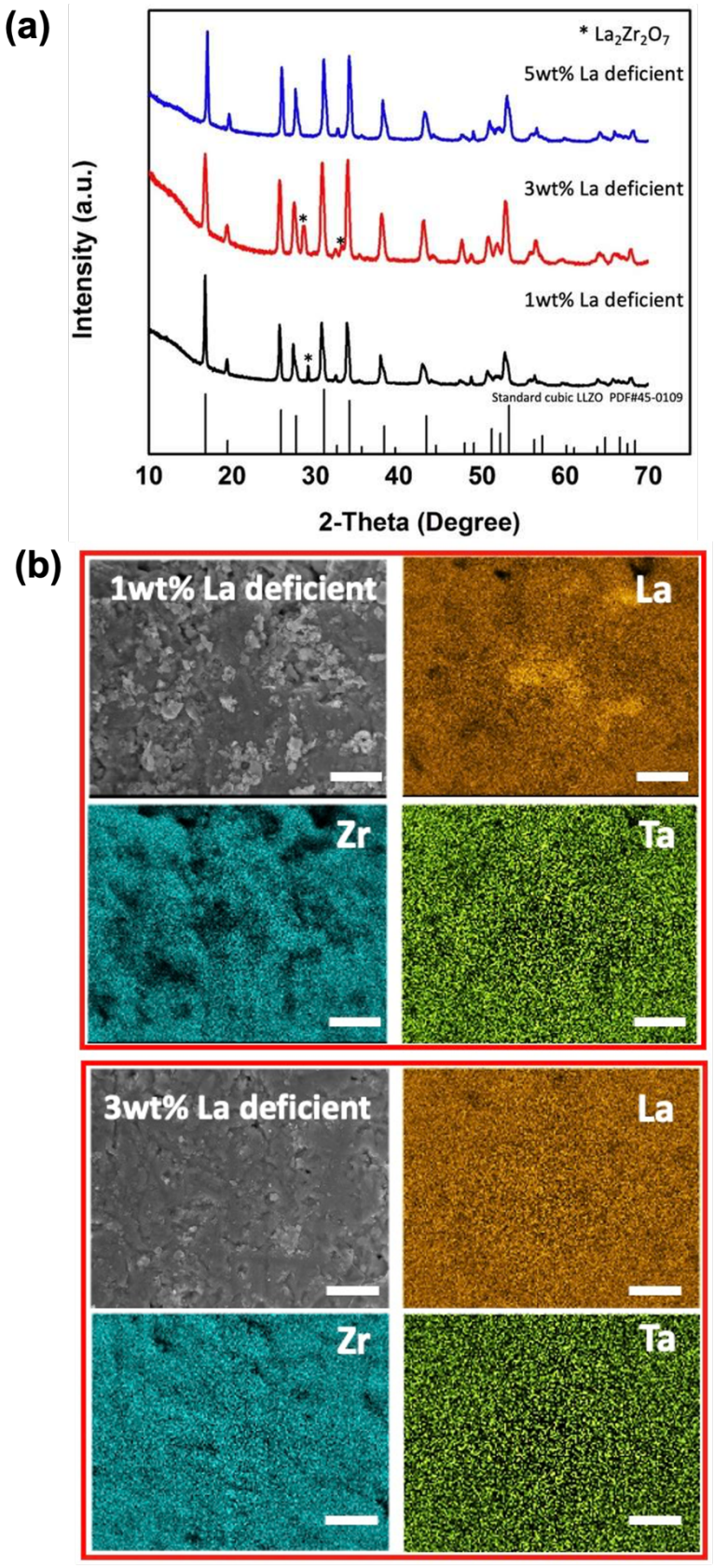

(a)
* $La_2Zr_2O_7$
5wt% La deficient
3wt% La deficient
1wt% La deficient
Standard cubic LLZO PDF#45-0109
Intensity (a.u.)
10
20
30
40
50
60
70
2-Theta (Degree)
(b)
1wt% La deficient
La
Zr
Ta
3wt% La deficient
La
Zr
Ta

Figure 4.4. La deficient Ta-LLZO sample characterizations. (a). The La deficient Ta-LLZO XRD pattern. There is no impurity peak in 5wt.% La deficient Ta-LLZO compared with 1wt.% and 3wt.% La deficient Ta-LLZO that both have $La_2Zr_2O_7$ impurity phase. (b). The SEM images (top view)/EDX mapping of La deficient Ta-LLZO with different amount of La deficiency. Note that even in 1wt% La deficient Ta-LLZO, it shows La segregation. While when it comes to 3wt% and 5wt% La deficient Ta-LLZO, the La segregation disappears showing uniform La element mapping. The scale bar is all 10 μm.

Table 4.2. Potential decomposition products between different sulfur species and La_2O_3 based on first principal calculation

	La_2O_3
S_8	S_8O, LaS_2
Li_2S_8	Li_2SO_4, Li_2S, LaSO, La_2SO_2
Li_2S_6	Li_2SO_4, LaSO, La_2SO_2
Li_2S_4	Li_2SO_4, Li_2S, La_2SO_2
Li_2S_2	LaS_2, Li_2SO_4, Li_2S
Li_2S	Li_2O, La_2SO_2

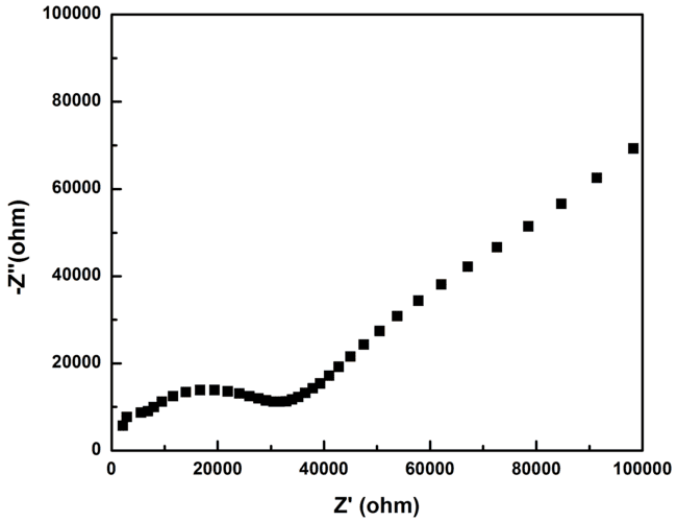


Figure 4.5. The impedance of the 5%wt La deficient Ta-LLZO tested by using blocking Au electrodes, which leads to a conductivity of 10^{-5} S/cm^2 at RT. The frequency range is from 1MHz to 100 Hz.

4.3.2 3D Asymmetric Bilayer Garnet Hybridized Li-S Battery Design

To overcome the above La-degradation issue and achieve a higher discharge capacity, a PEO-based interlayer was applied to physically separate the sulfur cathode from the stoichiometric Ta-LLZO which has La_2O_3 impurities suspected to react with the sulfur. The garnet hybridized Li-S cell design is shown in Figure 4.6.

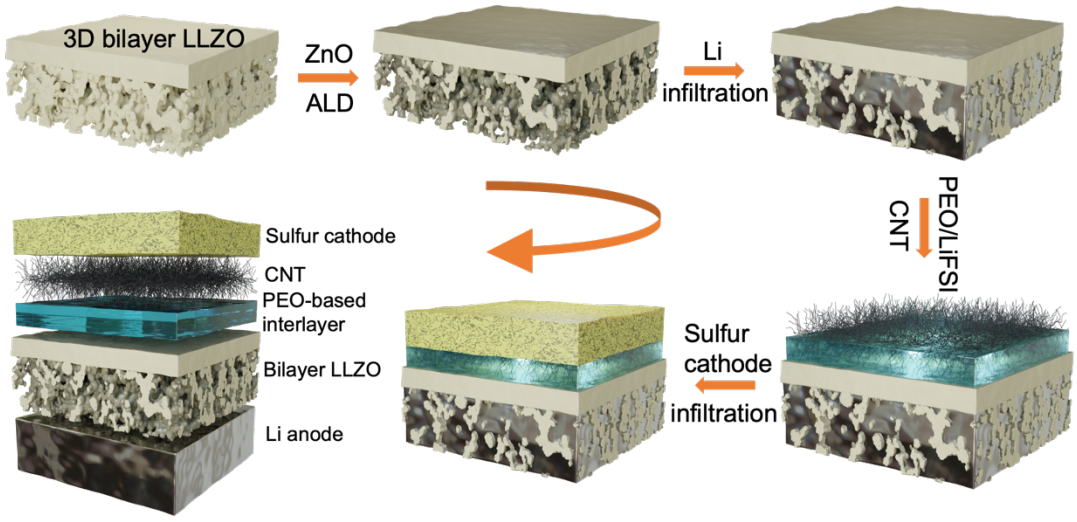


Figure 4.6. Schematic fabrication of the high energy density hybridized Li-S cell.

First, the 3D bilayer Ta-LLZO (95 μm and 25 μm thick dense and porous layer, respectively, shown by the SEM in Figure 4.7a) were fabricated(81), then coated by an ultra-thin and uniform ZnO ALD layer on both sides with an average thickness of 2.3 nm (Figure 4.7c). This was followed by fast Li infiltration (Video 1) in the porous side due to the capillary forces and the molten Li reacting with the ZnO coating layer and forming a Li-Zn-O layer that was easily wet by the remaining molten Li. As SEM image

in shown Figure 4.7b, the infiltrated Li metal filled the porous Ta-LLZO exceptionally well. Then a thin PEO-based interlayer (Figure 4.7d) containing CNT was coated on the dense Ta-LLZO side of the bilayer. LiFSI-based PEO electrolyte has the benefit of high ionic conductivity and low viscosity (17, 90, 91). It should also be note, that the ZnO ALD layer on the cathode side may help reduce the crystallinity of the PEO interlayer and increase its ionic conductivity(92–94). After adding the CNT/PEO interlayer, the sulfur/carbon cathode mixture was drop-cast on top of the CNT/PEO interlayer to achieve a high sulfur mass loading of 4 mg/cm^2, and 20 μL/cm^2 of 1M LiFSI in DME was added to wet the cathode side to ensure good contact.

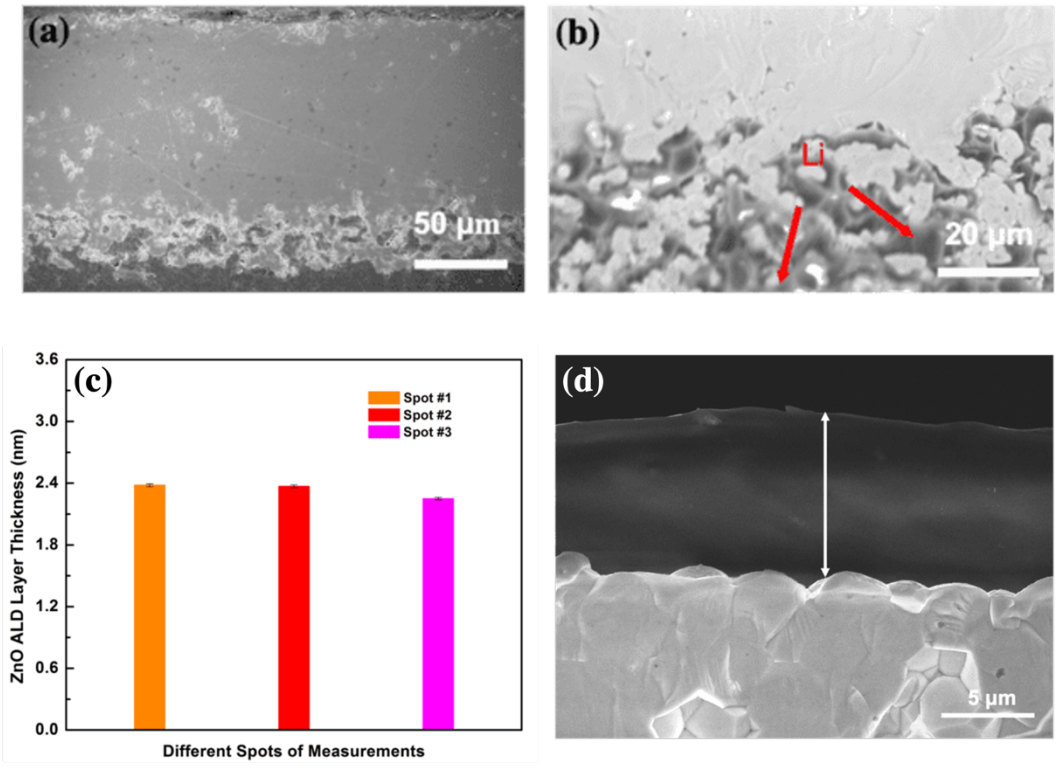


Figure 4.7. The characterizations of the bilayer Ta-LLZO with PEO-based interlayer coating used in the study. (a) The in-beam mode SEM cross-section images of 3D bilayer Ta-LLZO structure with a thickness of 95 µm in dense layer and a 25 µm in

porous layer with a dense layer on top and a porous layer at the bottom. (b). The SEM image of Li infiltration condition in the porous side of the 3D bilayer Ta-LLZO. (c). The ZnO ALD layer thickness distribution on a silicon wafer surface. The total thickness of the ZnO ALD layer is on an average of (2.33 ± 0.013) nm with little variation. (d). The cross-section of the PEO-based membrane and Ta-LLZO bilayer (dense side) showing the thickness of the PEO-based interlayer is around 8.4 μm.

4.3.3 Electrochemical Performance of the Hybridized Li-S Batteries

Electrochemical performance was characterized in 2032-type coin cells at RT. EIS measurements of Li-Li symmetric cells demonstrated that adding the PEO-based interlayer only increased the total area specific resistance (ASR) by 47.7 Ω-cm^2 (Figure 4.8a). Long-term cycling performance of Li-S full cell with 4 mg/cm^2 sulfur mass loading was performed at both 0.03C (0.2 mA/cm^2) and 0.05C (0.335 mA/cm^2) at RT (Figure 4.9a–d shows the first 35 cycles, while the full cycling performance of the same cells (100–200 cycles) is in Figure 4.10). As shown in Figure 4.9a, the first discharge cycle showed an exceptionally high capacity of 1307 mAh/g at 0.03C. During subsequent cycling, the capacity decay of 0.93% per cycle with an average Coulombic Efficiency (CE) approaching 100% (~102% in the first 35 cycles and then the CE stabilized with an average value of 99.4% throughout the entire 200 cycles). As illustrated in Figure 4.10a, a sudden capcaity drop was observed. We believe the sudden capacity drop and low CE was due to the nonideal packaging of the battery affecting battery performance during testing. However, the cell self-stabilized after 7 cycles as indicated by the high CE. Note that the polysulfide shutting issue was generally not observed as indicated by the high average CE (>99%), while if shuttle effect were taking place, the average CE could be ~80% over the entire testing cycles in Li-S cells

as demonstrated in our previous work(66). During cycling, the ASR of PEO/bilayer cell reduced from the pre-cycling value of 921 Ω-cm^2 to a post-cycling value of 691 Ω-cm^2 (Figure 4.8b). The reduction in cell ASR was likely due to improved infiltrated liquid electrolyte uniformity on the cathode side and a better sulfur cathode contact with carbon felt current collector during cycling which improves Li^+ and electron transport, respectively.

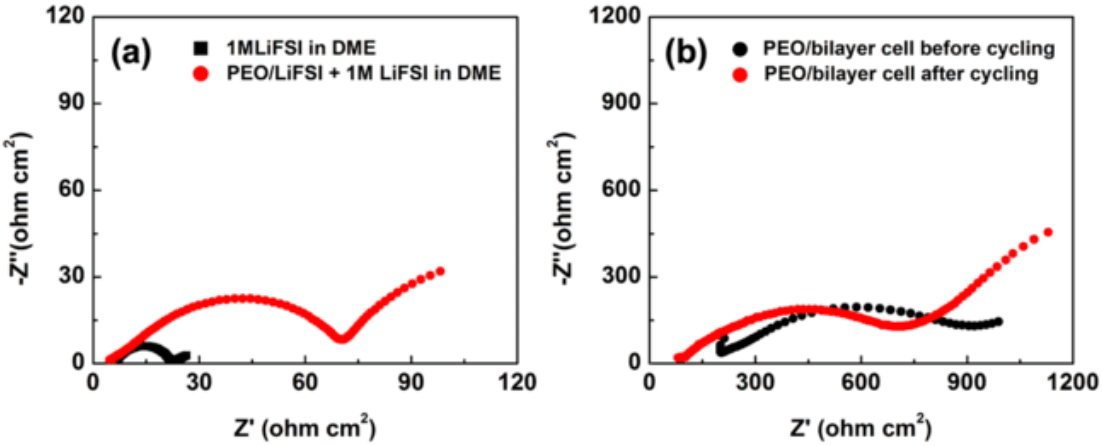


Figure 4.8. (a). The ASR of Li-Li symmetric cells for 1M LiFSI in DME (22.7 Ω-cm^2: the ASR of the liquid electrolyte and its SEI formation) and PEO/LiFSI membrane with 1M LiFSI in DME (70.4 Ω-cm^2: the ASR of the liquid electrolyte, its SEI formation, PEO/LiFSI membrane and the liquid electrolyte/PEO-based membrane interface). To make it comparable, the amount of each materials kept the same as that in Figure 4.9. (b). The ASR of Li-S full cells before and after cycling at 0.03C. The ASR of PEO/bilayer before cycling and after cycling is 921 Ω-cm^2 and 691 Ω-cm^2, respectively.

For comparison, Li-S full cells were assembled using porous polyethylene polymer separators (Celgard) instead of dense PEO interlayer (Figure 4.9a), since Celgard could also separate the sulfur cathode from the Ta-LLZO to prevent interfacial

side reactions. The Celgard/bilayer cell cycled at 0.03C had a capacity decay rate of 1.8% per cycle, almost double that of the PEO/bilayer cell, and had a lower average CE of 87.5%. Both approaches showed that the cell failure can be avoided compared with no interlayer case (Figure 4.2a). Based on this cell performance, the PEO-based interlayer was shown to stabilize the cathode/Ta-LLZO interface and achieve dramatically improved cycling results. When the cycling current of the PEO/bilayer cells was increased to 0.05C (Figure 4.9c), the capacity fade rate increased slightly to 1.1% per cycle compared to 0.93% per cycle at 0.03C.

The PEO/bilayer hybridized cell also showed good performance at higher C-rates (Figure 4.9e). The average discharge capacities for each of the 5 cycles at 0.05C, 0.1C and 0.2C were 1103 mAh/g, 970 mAh/g and 791 mAh/g, respectively, after which the cell was still able to deliver 882 mAh/g when cycled back to 0.05C. While the C-rate performance of Celgard/bilayer cell showed good capacity recoverability, the discharge capacity at each C-rate was ~1/2 that of PEO/bilayer cells.

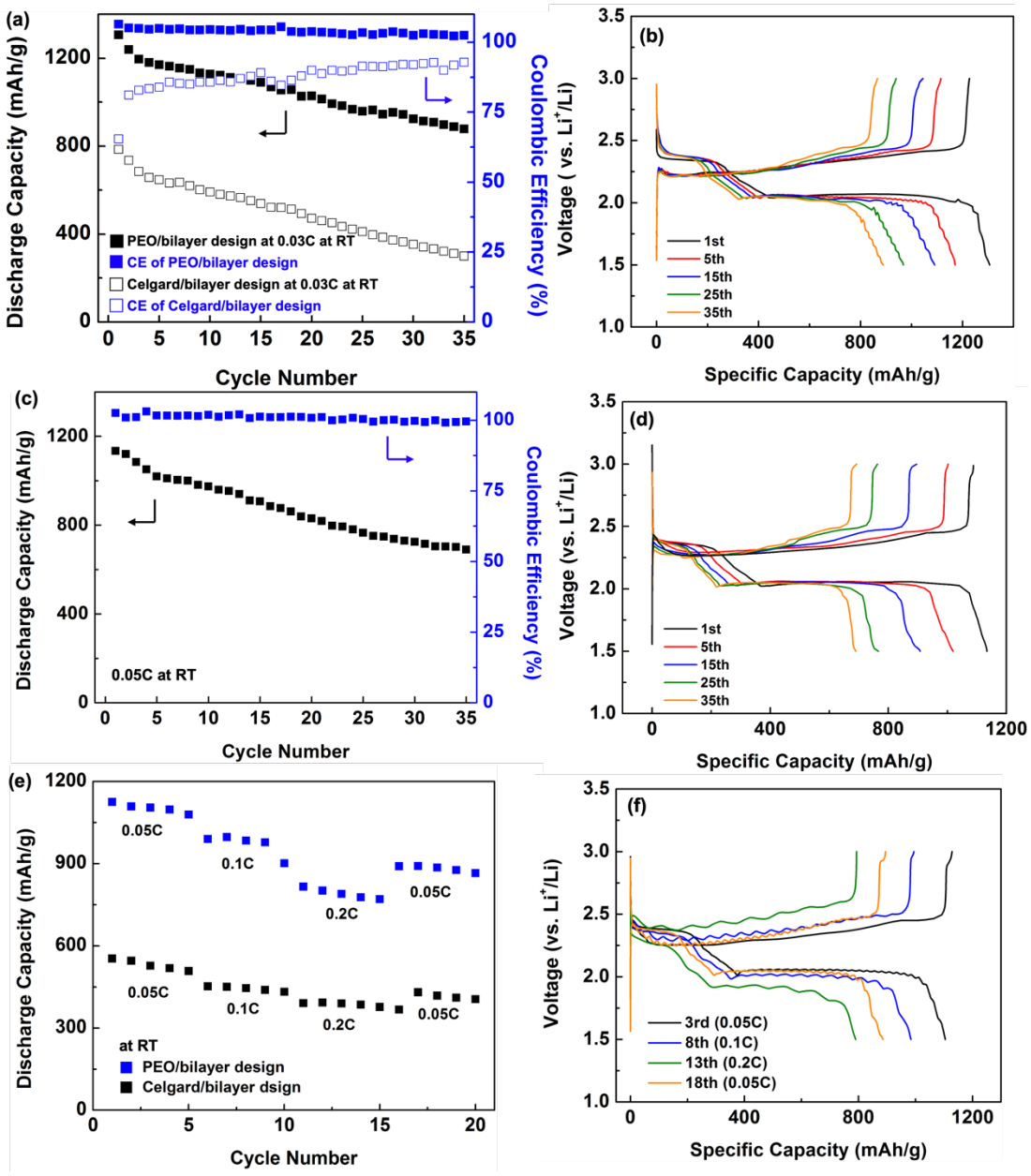


Figure 4.9. Electrochemical performance of the 3D asymmetric bilayer garnet hybridized Li-S cells. a) The dense PEO/bilayer and Celgard/bilayer cells cycling performance tested at 0.03C at RT and b) the voltage profile of the PEO/bilayer cells at 0.03C at RT. c) The PEO/bilayer cell tested at 0.05C at RT and d) the voltage profile of the PEO/bilayer cells at 0.05C at RT. e) The comparison of rate capability of PEO/bilayer and Celgard/bilayer cells. and f) the voltage profile of C-rate test of PEO/bilayer cell.

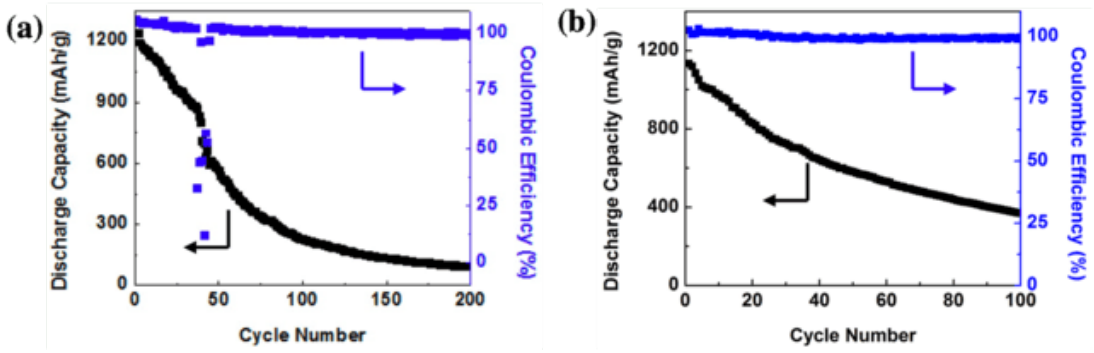


Figure 4.10. The full cycling performance of the PEO/bilayer cells reported in Figure 4.9. a). and b) are the 200 cycles and 100 cycles for the cells tested at 0.03C and 0.05C at RT, respectively. There is a capacity jump decrease after 35 cycles at 0.03C with lower Coulombic Efficiency for 7 cycles. But overall, the average Coulombic Efficiency at 0.03C and 0.05C is 99.4% and 99.8%, respectively, which demonstrate the polysulfide shuttle is fully blocked.

All the PEO/bilayer cells showed stable charge/discharge voltage profiles, featuring the two typical reduction plateaus representing the S_8 to polysulfide to Li_2S conversion behavior and without any charge voltage fluctuations (Figure 4.9b, 4.9d and 4.9f). In addition, the 2nd discharge voltage plateau was maintained without voltage reduction during cycling at both 0.03C and 0.05C, which indicate the PEO/bilayer Ta-LLZO design blocked the polysulfide shuttle(95). This further demonstrated the effectiveness of the PEO-coated interlayer between the sulfur cathode and the bilayer Ta-LLZO. A comparison of our designs with other solid-state Li-S cells and with Li-S cells using liquid electrolytes is shown in Table 4.3.

Table 4.3. The Coulombic Efficiency comparison of our designs with other Li-S cells and the effect of polysulfide shuttle.

Sulfur Loading mg/cm^2	Temperature	Main Electrolyte	Average Coulombic Efficiency (%)	Ref.
2.2–2.3	RT	LLZO***	~87%	(96)**
1	RT	LLZO***	~99%	(97)**
0.8	RT	LLZO***	99.2%	(98)**
1	RT	LLZO***	99.2%	(99)**
1	RT	LLZO***	99.4%	(100)**
3.2	RT	LLZO***	99.5%	(101)**
0.7	RT	$LiPF_6$ in FEC/FEMC/HFE	99.5%	(102)
2–3	RT	LiTFSI in DOLDME with $LiNO_3$ additive	96.5%	(103)**
1.4	RT	LiTFSI in DOLDME with $LiNO_3$ additive	96%	(104)**
N/A*	RT	LiTFSI in DOLDME with $LiNO_3$ additive	98%	(105)**
4	RT	Ta-LLZO	99.4% (0.03C) 99.8% (0.05C)	This work

* It is the very first demonstration to use $LiNO_3$ in pure liquid electrolyte Li-S cell to mitigate polysulfide shuttle.
** The published results do not mention the average Coulombic Efficiency over the entire cycling range, so that the value is calculated manually with the help of "Image J" software.
*** Note that certain dopants are used to obtain a high ionic conductivity at RT, which is also the same as shown in Table 4.4 in section 4.3.5.

4.3.4 Chemical and Electrochemical Stability and Mechanical Properties

Advanced characterization techniques—XRD, XPS and ToF-SIMS—were applied to systematically study the stability and geometry of the PEO-based electrolyte and the Ta-LLZO interface. To illustrate the chemical stability of the PEO-based film with Ta-LLZO, the solid PEO-based film was coated on the dense Ta-LLZO surface and the whole sample was heated to 60°C for 7 days, with and without subsequently rinsing by ACN before characterization. To demonstrate the electrochemical stability of the PEO-based membrane/Ta-LLZO interface, the cycled Li-S hybridized cells were used, and hybrid electrolyte rinsed by DME and ACN solvents before any postmortem characterizations.

Before cycling, the PEO-coated Ta-LLZO XRD pattern is a combination of the PEO-based electrolyte pattern and the pure cubic Ta-LLZO phase pattern (Figure 4.11). After removing the PEO-coated layer on the Ta-LLZO by ACN solvent, the XRD pattern of the PEO-based membrane disappears and only the cubic Ta-LLZO pattern remains. There were no structural changes at the Ta-LLZO surface attached to PEO-based membrane. After electrochemical cycling, the postmortem XRD analysis illustrated the bilayer Ta-LLZO still maintained the pure cubic phase, indicating the PEO-based membrane does not disorder the structure of Ta-LLZO.

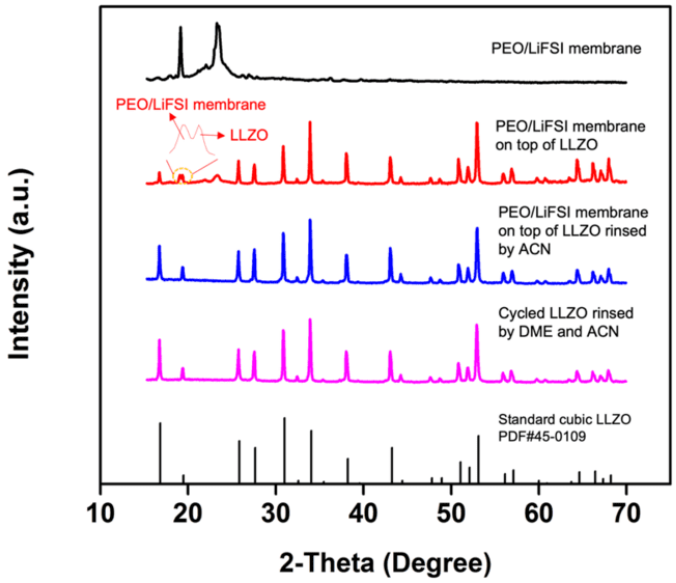


Figure 4.11. The XRD patterns of the hybridized electrolyte before and after cycling. PEO/LiFSI membrane only (black curve), PEO/LiFSI membrane on top of the bilayer Ta-LLZO (red curve), PEO/LiFSI membrane on top of the bilayer Ta-LLZO rinsed by ACN (blue curve) and the hybridized electrolyte of the cycled cell rinsed by DME and ACN (purple curve).

To further investigate the stability of LLZO, XPS spectra of Ta-LLZO after cycling 30 times was studied. The Ta-LLZO was sputtered with Ar^+ for 10 min, 20 min and 40 min and shown in Figure 4.12 (a) and (b). (Zr 3d and La 3d spectra before sputtering were observed but are not shown here) The sputtered depths are roughly expected to be around 10 nm, 20 nm and 40 nm, respectively, although the sputtering rate may have varied due to varying amounts of organic compounds from PEO and the electrolyte.

Zr $3d_{5/2}$ and Zr $3d_{3/2}$ peaks in Zr 3d spectra after sputtering are fitted well with the theoretical area ratio constraint. This indicates that there is no disordered lattice for Zr in Ta-LLZO after 10 min sputtering and beyond. Zr $3d_{5/2}$ and Zr $3d_{3/2}$ were observed at 181.5 eV and 183.8 eV, respectively. These peak positions are in good accordance with previously reported values (106). The peak positions are consistent throughout the sputtering, and the peak intensity increased with the sputtering time due to the elimination of surface products. The sputtered peak positions did not move during sputtering which suggests that Ta-LLZO structure was not altered during cycling and sputtering.

The La *3d* peak shows 4 distinct peaks and 2 broad peaks in the region of 820–870 eV. La $3d_{5/2}$ peaks are found at 827–840 eV and can be deconvoluted into 3 peaks: one main peak (833.1 eV) with two satellite peaks of bonding (837.4 eV) and antibonding (833.6 eV) components(107). The antibonding peak is broader than the main peak and the bonding peak, which is consistent with La *3d* peak observation of La compounds(107). The 842–870 eV region shows La $3d_{3/2}$ and a broad plasmon peak of La $3d_{5/2}$ around 849 eV. The region above 840 eV is overlapped with La MNN (the

most intense La Auger peak) (107) which we were unable to subtract. Nevertheless, the peak positions of La $3d_{5/2}$ and La $3d_{3/2}$ are in good accordance with previous report of LLZO(108). The peak position and FWHM of La peaks did not change, between 10 min, 20 min and 40 min of sputtering which shows that the Ta-LLZO structure was not altered with cycling from about 10 nm deep and beyond, which is consistent with observation of Zr 3*d* spectra.

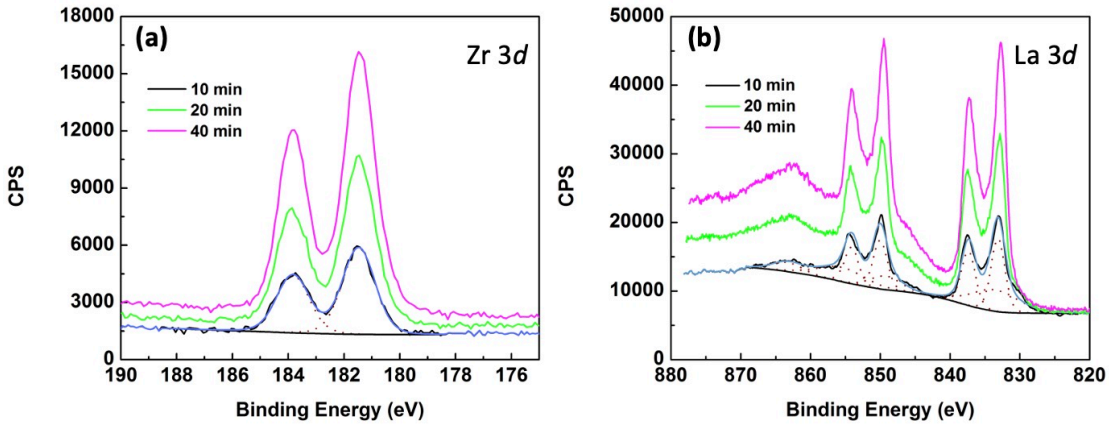


Figure 4.12. XPS depth profiling of Ta-LLZO. a). and b). are the Zr *3d* and La *3d* XPS spectra after Ar^+ sputtering for 10min, 20 min and 40 min, respectively.

As a baseline for the measurements on cycled samples, a sample that was not cycled was measured with no sputter depth profiling (Figure 4.13). The main peak of C 1s spectrum is attributed to C-O bond from the PEO coating. A small peak at lower binding energy which is attributed to hydrocarbon at 284.5 eV is used for referencing other peak positions reported here(83). C-O bond is at 286.2 eV which is the expected position(83). A small shoulder at 288.0 eV is attributed to ketones(83).

The O 1s spectra was deconvoluted into 2 peaks. The main peak at 532.5 eV is attributed to O in PEO(108). Another source of O in the control sample is FSI anion. A small peak at 533.2 eV can be attributed to N-SO_2-F in FSI anion.

The main S $2p_{3/2}$ peak was observed at 169.3 eV with shoulder at 167.6 eV and a small peak at 163.1 eV. Since the sample was exposed to 1 M LiFSI/DME but not cycled, the 169.3 eV peak is attributed to N-SO_2-F in the FSI anion. 167.6 eV can be attributed to sulfates(83). A peak at 163.1 eV can be attributed to sulfides(83, 108). Those may have come from impurities that were included in LiFSI salt or decomposition products of LiFSI.

The F 1s spectra shows 2 peaks: one large peak at 687.1 eV and one smaller peak at 684.4 eV. Since the majority of F should be from FSI, the large peak at 687.1 eV can be attributed to N-SO_2-F in the FSI anion. The peak at 684.5 eV is in the metal fluoride region and can be attributed to LiF(83, 109). Considering that the S 2p suggests the presence of FSI impurities or decomposition products, LiF may have been generated from the salt decomposition, or it was already in the salt as an impurity.

Since the main source of N in the sample is the FSI anion, the main N 1s peak at 399.1 eV is attributed to LiN-(SO_2-F)$_2$ in FSI anion. This peak position is used for peak attribution in the main manuscript. The peak position of 400.5 eV is in good accordance with the compound NH_2CONH_2(108) which is used in one of synthetic method for HFSI(110). This position is also in good accordance with other chemicals that includes -CONH-(108). Hence, we attribute this peak mainly to the impurity from LiFSI which contains -CONH-.

The Li 1s peak was fitted with one peak at a peak position of 55.5 eV. Since LiFSI is the main source of Li, this peak is attributed to $LiN(SO_2F)_2$. While LiF is suggested to be present from the F 1s spectrum, LiF (which would occur at 55.7 eV(108)) was not observed in the Li 1s spectrum deconvolution, due to the low overall intensity and high noise.

In summary, LLZO coated with PEO then soaked in LiFSI/DME followed by ACN is used for the baseline sample. The residual layer was thick enough to entirely screen the underlying LLZO. A list of peaks from LiFSI is as follows; O 1s at 533.2 eV, S $2p_{3/2}$ at 169.3 eV, F 1s at 687.1 eV, N 1s at 399.1 eV, and Li 1s at 55.5 eV. Additional features corresponding to smaller amounts of LiF, ketones, and compounds containing -CONH- such as NH_2CONH_2, which is used to synthesize HFSI, were observed. Figure 4.13 shows all the expected peaks from LiFSI and PEO and other peaks indicating that the residual layer consisted of PEO with LiFSI and minor impurities.

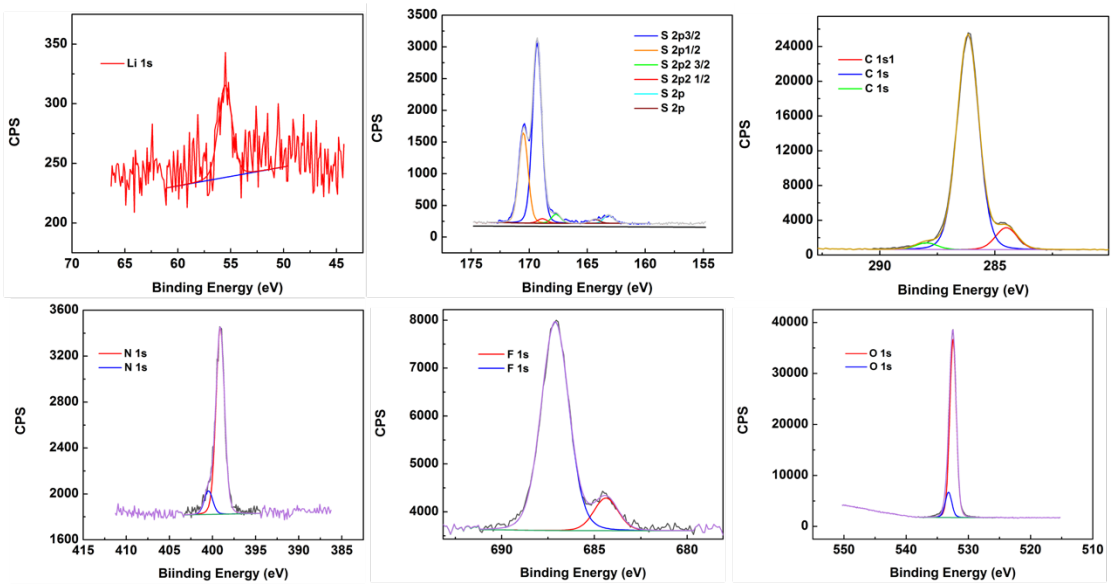


Figure 4.13. XPS spectra of Li 1s, S 2p, C 1s, N 1s, F 1s, and O 1s from an unsputtered non-cycled control sample (pellet LLZO coated with PEO soaked with LiFSI/DME, followed by ACN).

XPS spectra of cycled LLZO before sputtering is shown in Figure 4.14. In the C *1s* spectrum, the lowest peak at 284.5 eV(111) is due to hydrocarbons and is used to reference all the binding energy. A 286.2 eV peak is attributed to C-O bond(111). A peak at 287.9 eV is attributed to ketones(111) and a 289.2 eV peak is attributed to carbonates(111) such as Li_2CO_3. A small peak at 292.7 eV is in good accordance with the peak position of fluorinated carbon(108, 112) which was also observed in F 1s spectrum.

In the Li *1s* spectrum, Li *1s* peak is overlapped with Zr *4s* which is at 53.5 eV. This Zr *4s* peak position is in good accordance with ZrO_2(111) and it is expected to arise from Zr in LLZO which should be at a similar binding energy. The peak center of Li *1s*, from a fit to a gaussian-Lorentzian peak shape, was at 55.1 eV. LiF (55.7 eV), Li_2O (55.6 eV), LiOH (54.9 eV), LiN_3 (55.2 eV), Li_2CO_3 (55.2 eV)(113) are possible components. Li in LLZO (55.2 eV) can also be present(114), but it is hard to distinguish each component because of close vicinity of the possible components.

The F *1s* peak showed 3 peaks. The first 2 peaks at 684.5 eV and 687.2 eV are attributed to LiF and N-SO_2-F, respectively. Attribution of 687.2 eV peak to N-SO_2-F is based on the F 1s spectra of uncycled LLZO soaked in 1 M LiFSI/DME which we used as a control sample (see Figure 4.13 for details).

The intensity of LiF in relation to N-SO_2-F significantly increased compared to uncycled LLZO (Figure 4.13) soaked in 1 M LiFSI/DME, which suggests LiFSI

decomposed during cycling. There was another peak at 688.5 eV which is in reasonable agreement with fluorinated carbon position(83, 108). This is consistent with the C *1s* peak at 292.7 eV which is also attributed to fluorinated carbon.

The S 2p spectrum was deconvoluted into 5 components. The S $2p_{3/2}$ positions are 161.5 eV, 163.3 eV, 166.4 eV, 168.3 eV, and 169.3 eV and are attributed to Li_2S, sulfides, $Li_2S_2O_4$, Li_2SO_2(108, 111, 115, 116) and $LiN(SO_2F)_2$ (based on the N-SO_2-F peak position from control sample in Figure 4.13), respectively. Considering that decomposition products from LiFSI were expected based on the discussion on F 1s spectrum, sulfur compounds may have generated from FSI decomposition.

The O 1s spectrum was deconvoluted into 4 peaks. A 528.0 eV peak is within the range of metal oxides(111). This can be attributed to oxides formed on LLZO surface. (Zr 3d and La 3d spectra were observed but not shown here) The peak intensity of metal oxides is relatively low because metal oxides are covered with decomposition products formed on LLZO. A 529.4 eV peak is attributed to O in ZnO(108) from the ALD coating applied to the LLZO sample. (ZnO peaks observed in Zn 2p spectrum but not shown here) A 531.4 eV peak can be attributed to Li compounds such as Li_2O (531.3 eV), LiOH (531.3 eV) and Li_2CO_3 (531.4 eV)(108). Their peak positions are within few eV and was not able to deconvolute. The 532.6 eV peak is attributed to the C-O bond(108). It is expected that C-O is present from PEO and DME. Li_2SO_4, which is expected from the S 2p spectrum, would have a peak at 532.2 eV(108), however, Li_2SO_4 was not able to be distinguished because of the close vicinity to the C-O peak. Since the 531.4 eV peak (Li compounds) has the largest area, lithium decomposition compounds were the major component in cycled sample surface. The decrease in

intensity of the FSI anion peak, at 533.3 eV, relative to the baseline sample suggests that most of FSI anion has reacted at the surface of LLZO.

In the N 1s spectrum, the 398.2 eV peak is attributed to nitrides(111, 112). A 399.6 eV peak is close to the FSI anion peak but 0.4 eV higher than the position observed in Figure 4.13 for the control sample. As indicated in O 1s spectrum, most of the FSI anion is decomposed, hence this peak is attributed to decomposition products of FSI. A 401.9 eV peak can be attributed to LiN_3(108, 109). There should be another peak at 398.7 eV (109) for LiN_3 but it was not clearly observed due to low intensity of the peak.

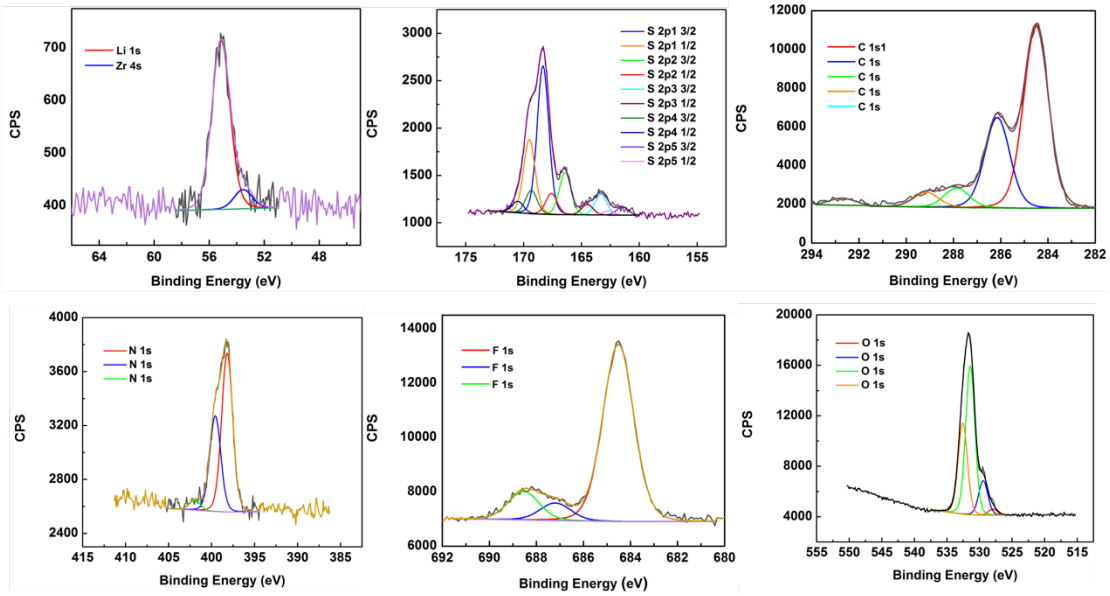


Figure 4.14. XPS spectra of Li 1s, S 2p, C 1s, N 1s, F 1s, and O 1s from an unsputtered cycled samples.

In summary, XPS observations suggest that the following components are formed with cycling; Li_2CO_3, LiF, ketones, Li_2O, LiOH, LiN_3, Li_2S, $Li_2S_2O_4$, Li_2SO_4.

Decomposition of the FSI was suggested from the S 2p, F 1s, O 1s, and N 1s spectra, and decomposition of PEO was suggested from the C 1s and O 1s spectra.

By analyzing the XPS spectra obtained before sputtering, Li_2CO_3, LiF, ketones, Li_2O, LiOH, LiN_3, Li_2S, $Li_2S_2O_4$, Li_2SO_4 were found to be at the surface of Ta-LLZO (Figure 4.13 and Figure 4.14 for detail). Among these components, Li_2S and Li_2SO_4 may have contributed to protecting LLZO from further degradation(117) resulting in Zr 3d and La 3d spectra which did not significantly change throughout the sputtering time. As shown in sputtered spectra of Zr 3d and La 3d, PEO coating prevented La segregation and led to successful cycling.

The ToF-SIMS was used to characterize the thickness of the polymer/ceramic interphase layer, due to it high surface sensitivity and chemical selectivity(118). As shown in Figure 4.15, the decomposition products LiF^- from LiFSI and CH_3O^- from PEO were observed at the interface. These results are in good agreement with XPS measurements. As the sputtered depth increases, the counts of those decomposition compounds change from low to high and then back to low indicating there is an interphase layer formed at the interface. The number of counts on ZrO^- and LaO_2^- that is used to indicate Ta-LLZO signals, increase and then stabilize (blue region) when pure Ta-LLZO phase is reached.

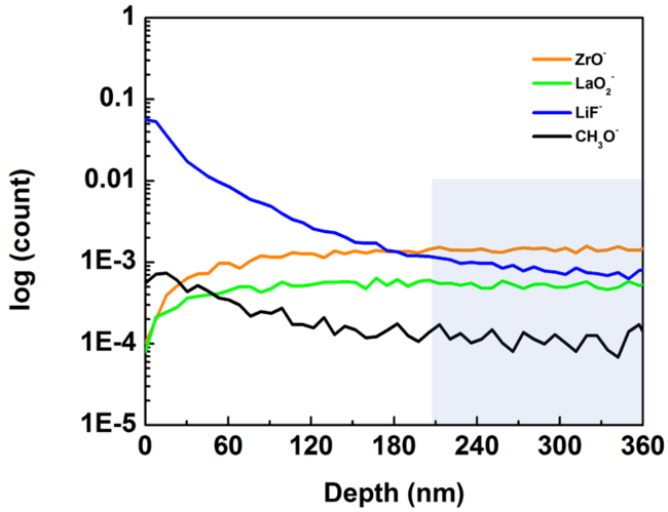


Figure 4.15. The ToF-SIMS depth profile of the cycled PEO/bilayer cell.

In addition to the PEO-based interlayer preventing side reactions between the sulfur cathode and Ta-LLZO, finite element modeling (FEM) showed the low elastic modulus PEO was able to isolate the Ta-LLZO from the stress/strain associated with the 80% volume expansion of the sulfur cathode during discharge. Without the protection of the PEO-based interlayer, simulations indicate the sulfur volume expansion would create significant stress in the Ta-LLZO (Figure 4.16a and 4.16c), which could lead to fractures in the electrolyte separator and eventual short circuit. With the protection of PEO-based interlayer, the low elastic modulus PEO could deform in response to the sulfur volume expansion while remaining intact, thereby protecting the Ta-LLZO (Figure 4.16b and 4.16d). Based on the FEM results, the highest strain in the PEO enhanced Ta-LLZO is 3.82×10^{-2}, which is three magnitudes higher than pure Ta-LLZO (6.68×10^{-5}). The resulted higher strain of PEO can efficiently adopt the stress and volume expansions of the sulfur cathode.

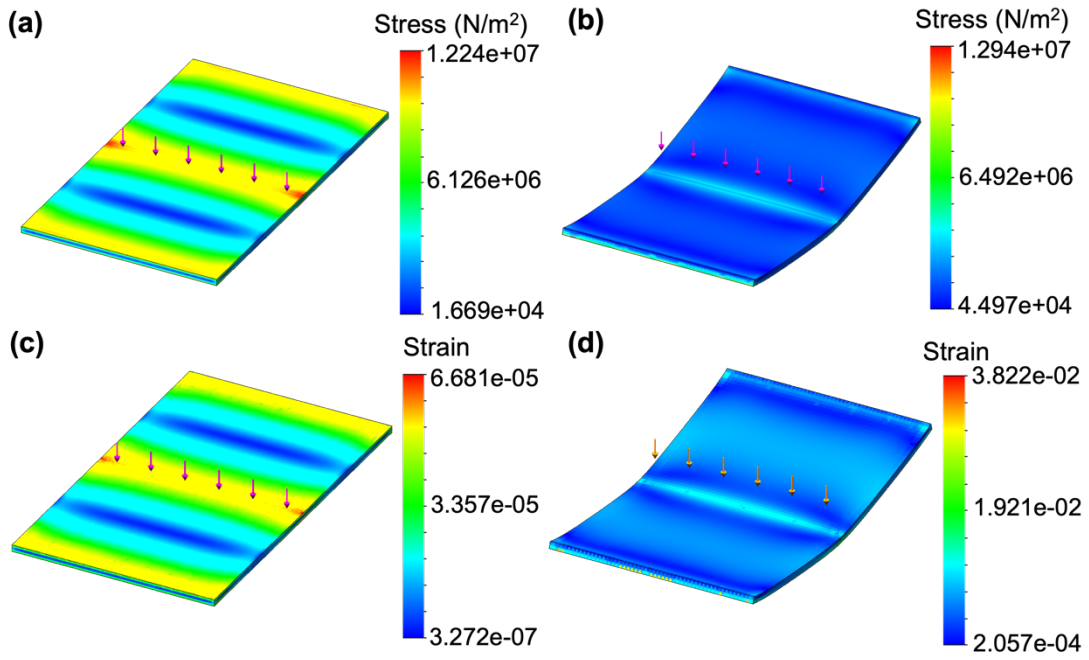


Figure 4.16. Mechanical properties of the Ta-LLZO and PEO electrolyte. a) and b) are the stress distribution of the Ta-LLZO and PEO electrolyte, respectively. c) and d) are the strain distribution of the Ta-LLZO and PEO electrolyte, respectively.

4.3.5 Energy Density Evaluation of the Hybridized Li-S Batteries

Specific capacity and corresponding cell energy density are all critical to practical application. For this work with a high sulfur mass loading on a planar surface, we demonstrated that, with our thin bilayer Ta-LLZO design, an energy density of 639 Wh/L and 134 Wh/kg was achieved at 0.03C at RT based on the high initial discharge capacity of 1307 mAh/g (Figure 4.9a and 4.9b). The detailed calculation and comparison are shown in Table 4.4 and Table 4.5, respectively. This value is beyond state-of-the-art garnet-type hybridized Li-S batteries with a sulfur cathode on a planar garnet surface, which have limited energy densities of less than 400 Wh/L and 100

Wh/kg (Figure 4.17), mainly due to the thick electrolyte and low sulfur mass loading(58, 69, 96–101).

Table 4.4. The energy density calculation

Material	**Mass mg/cm^2**	**Density g/cm^3**	**Volume (μL/cm^2)**	**Specific Capacity (mAh/g)**	**Charge (mAh)**
Sulfur	**4.00**	**2.07**	**1.93**	**1307**	**5.23**
CNT	**0.80**	**1.35**	**0.59**		
PEO	**1.20**	**1.44**	**0.83**		
Liquid electrolyte	**21.00**	**1.06**	**0.00**		
Ta-LLZO	**55.00**	**5.00**	**12.00**		
Li-metal	**1.73**	**0.53**	**2.24**	**3861**	**6.68**
Total	**83.73**		**17.60**		
Average Voltage=2.15 V				**Energy Density (Wh/kg)**	**134**
				Energy Density (Wh/L)	**639**
				Projected (Wh/kg)	**257**
				Projected (Wh/L)	**1308**

* Cell energy density calculated based on the cathode area and the amount of Li used is based on the capacity match: $m_{(sulfur)} \times C_{(sulfur)} = m_{(Li)} \times C_{(Li)}$, where *m* and *C* represent the mass and capacity, respectively. $C_{(sulfur)}$ = 1670 mAh/g. The capacity curve (1307 mAh/g) at 0.03C revealed an energy density of 639 Wh/L and 134 Wh/kg. To make our results comparable with the published ones, all the data shown in Figure 4.17a are calculated in the same way.

** Based on the calculated values from Table 4.4, the N/P ratio of the assembled garnet Li-S battery was ~1.9. An excess lithium of ~1.5 mg/cm^2 was used for contact with the current collector as demonstrated in our previous work(70).

*** The projected energy density in Table 4.4 was calculated by simply reducing the dense layer of the bilayer LLZO to be 10 μm (the actual dense layer thickness of 95 μm) while keeping all other parameters the same as the actual case.

Table 4.5. The Comparison on initial discharge capacity and its related energy density of our work with the state-of-art published results

Sulfur Loading mg/cm^2	Temperature	Main Electrolyte	Electrolyte Thickness (μm)	Initial Discharge Capacity (mAh/g)	Energy Density		Ref.
					Wh/L	Wh/kg	
2.2–2.3	RT	LLZO	100	1250	397	65	(96)**
1	RT	LLZO	1200	1150	20	4	(97)**
0.8	RT	LLZO	1200	~1150	17	3	(98)**
1	RT	LLZO	1000	1173	24	5	(99)**
1	RT	LLZO	1000	1150	20	4	(100)**
3.2	RT	LLZO	700	1050	85	18	(101)**
7.5	RT	Bilayer LLZO	Dense: 35 Porous: 70	645	511	248	(58)
5.4	RT	Trilayer LLZO	Porous: 70 Dense: 30 Porous: 70	1169	633	272	(69)
4	RT	Bilayer Ta-LLZO	Dense: 95 Porous: 25	1307	639	134	This work
4	RT	Bilayer Ta-LLZO	Dense: 10 Porous: 25	1307	1308	257	This work

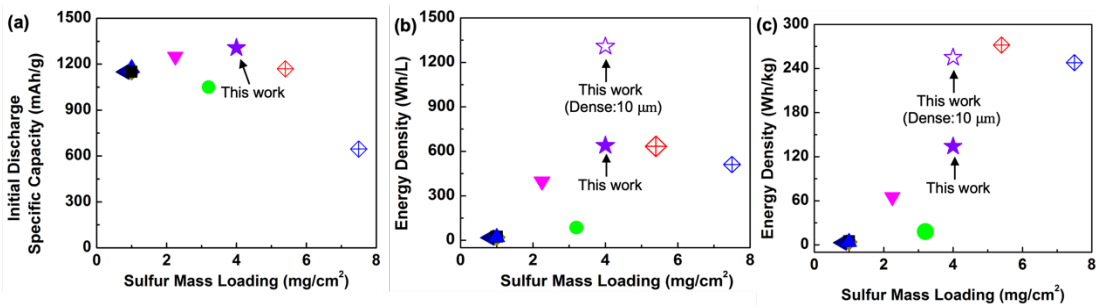


Figure 4.17. Cell energy density evaluation. a) and b–c) The comparison of initial discharge capacity and energy density in this work with state-of-art published results(58, 69, 96–101), respectively.

Based on the results reported in this work, by simply reducing the dense layer thickness to 10 μm as we have previously demonstrated(70), and maintaining the 4 mg/cm^2 sulfur loading, the energy density would be 1308 Wh/L and 257 Wh/kg (Figure 4.17, open violet star). Further energy density predictions based on different parameter optimizations of the PEO/bilayer design are shown in Figure 4.18. With the further assumed amount of CNT and liquid electrolyte, an exceptionally high energy density of 1308 Wh/L and 485 Wh/kg could be achieved when the dense layer thickness is 10 μm.

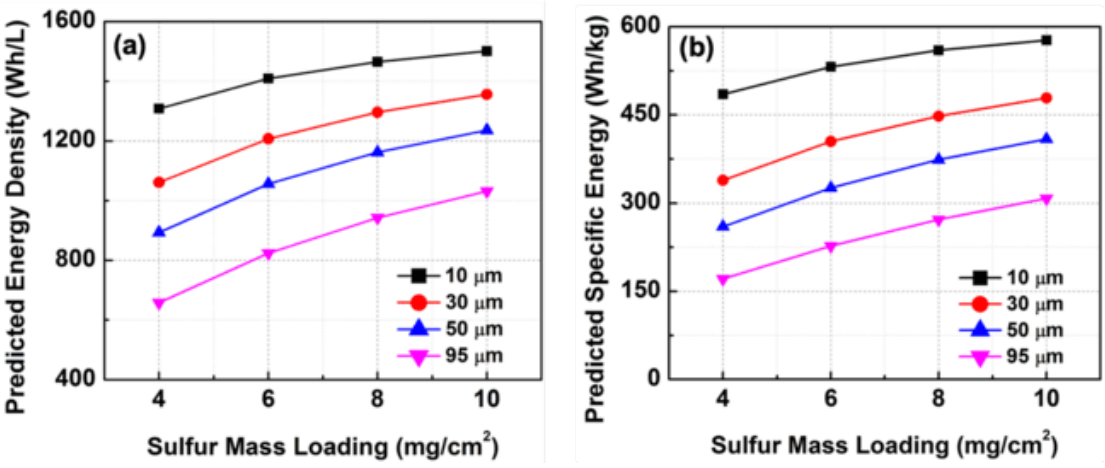


Figure 4.18. The further energy density prediction based on different parameters optimizations of the PEO/bilayer design versus sulfur mass loading and varying dense layer thickness in the bilayer Ta-LLZO.

* The reasonable assumptions are a following to obtain the values in Figure 4.18:

- The projected value uses the sulfur specific capacity of $C_{(sulfur)}$ = 1307 mAh/g to match with Li anode to get the amount of Li needed.
- A porosity of 55% of the porous layer is used and its thickness is derived from the volume of Li metal.
- The amount of cathode and liquid electrolyte is calculated in such way: sulfur(vol%):CNT(vol%)= 9:1; cathode(vol%):liquid electrolyte(vol%)=7:3.

4.4 Conclusions

We demonstrated that La segregation to the garnet surface reacts with sulfur cathodes and is corelated with the cell failure/degradation mechanism in garnet-type Li-S batteries. To resolve the challenge, PEO/LiFSI was applied to physically separate the sulfur cathode and LLZO and it effectively improved the performance of garnet Li-S full cells by introducing a stable polymer/ceramic interface. A high sulfur mass loading (4 mg/cm^2) on a planar garnet surface was able to achieve a capacity of 1307 mAh/g and a good energy density of 639 Wh/L and 134 Wh/kg at RT was demonstrated. By simply reducing the LLZO dense layer thickness to 10 μm as we have previously demonstrated(70), this battery could achieve a higher energy density of 1308 Wh/L and 257 Wh/kg. The stability between PEO-based film and Ta-LLZO were systematically studied through XRD and XPS analysis, the bulk Ta-LLZO structure and the valence state of La^{3+} and Zr^{4+} do not change from 10 nm deep and below after cycling indicating the PEO-based layer can form a chemically and electrochemically stable interface with the Ta-LLZO ceramic electrolyte. In addition, finite element analysis showed a PEO-based interlayer inserted between the bilayer Ta-LLZO and the sulfur cathode could

accommodate the stresses associated with sulfur volume expansion during lithiation, thereby eliminating the risk of Ta-LLZO fracture and potential short circuit.

Chapter 5: High Sulfur Loading and Capacity Retention in Bilayer Garnet Lithium-Sulfur Batteries with Gel Polymer Electrolytes

5.1 Introduction

From the sulfur cathode side, our studies in Chapter 4 have indicated the sulfur cathode/Ta-LLZO interface can be unstable, with the sulfur reacting with La-segregation phases at the LLZO surface. At the same time, the huge sulfur volume expansion during discharge (~80%)(67, 68) applies significant stress/strain to the sulfur cathode/Ta-LLZO interface and may cause cracking. In Chapter 4, to solve these issues, we added a PEO-based interlayer between the sulfur cathode and bilayer Ta-LLZO to improve the chemical and mechanical stability of the interface during cycling, with the resulting Li-S battery demonstrating a high initial discharge capacity of 1307 mAh/g(119). However, a relatively large amount of catholyte (20 μL/cm^2) was used and relatively fast capacity decay was observed when cycling at 22℃, reducing cell energy density. Likewise, the low sulfur mass loading and the high mass of thick LLZO separators(96–98, 100) in these cells negatively impacted their energy densities.

To address these issues, we have developed an innovative gel polymer electrolyte (GPE) as catholyte to replace the PEO as a stabilizing interlayer between the cathode and the thin bilayer Ta-LLZO electrolyte. The GPE was synthesized *in-situ* on the dense Ta-LLZO surface, to stabilize the sulfur cathode/Ta-LLZO interface while maintaining good physical contact.

*5.2 **Experimental***

LLZO Synthesis: Ta-doped LLZO was prepared through solid state reaction. Stoichiometric amounts of lithium hydroxide monohydrate ($LiOH{\cdot}H_2O$, 98%, Alfa Aesar), tantalum oxide (Ta_2O_5, 99.85%, Alfa Aesar), zirconium oxide (ZrO_2, 99.9%, Inframat Advanced Materials) and dried lanthanum oxide (La_2O_3, 99.99%, GFS Chemicals) were ball milled and calcined at 900 °C for 10 hours in a magnesium oxide crucible. The as-calcined powder was again ball milled for 24 hours in 2-propanol. After drying the calcined powder, it was pressed into pellets and covered with sufficient mother powder before sintering at 1100 °C for 8 hours. The sintered pellets were mechanically polished to a desired thickness using silicon carbide abrasive discs (LECO Corp.) with different grit size (#400–#2000) to create a smooth surface. XRD was used to confirm the pellets were pure cubic phase LLZO (Figure 5.1). The synthesis process for Ta-doped LLZO bilayer (Figure 5.2) was based on the synthesis process for Nb-doped LLZO discussed in our previous publication(58), with the Ta precursor replacing the Nb precursor. Specifically, fish oil, toluene and Isopropyl alcohol were added into the calcinated powder and ball milled for 24 hrs. Subsequently, benzyl butyl phthalate, polyalkylene glycol and polyvinyl butyral were weighed out and mixed for another 24 hrs. After that, the slurry was centrifugally dried for 30–40 min. For the dense layer, the slurry was directly cast at 10 cm/min through a doctor blade onto a mylar sheet while being heated at 120°C. For the porous layer, poly(methyl methacrylate) spheres were added into the slurry and ball milled for another 1hr before tape casting. The dense tape and porous tape were laminated together using a hot press roller. After that, the bilayer tape was sintered in a tube furnace at 1100°C. The Li_2CO_3

on the surface of the bilayer LLZO and LLZO pellet was removed by heating the samples to 800℃ for 2 hours under inert gas flow. After that, a ZnO ALD coating layer was deposited using an ATHENA ALD system (Forge Nano Inc.).

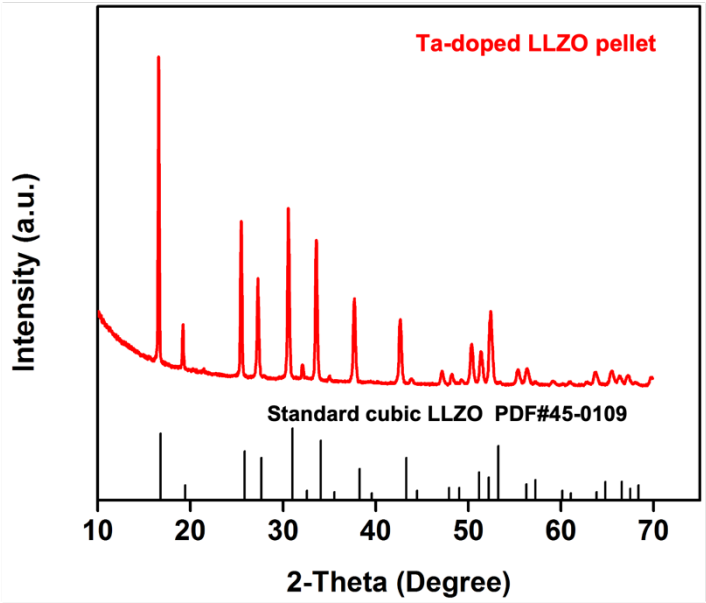


Figure 5.1. The XRD pattern of the Ta-LLZO pellet for symmetric cell studies, showing its pure cubic garnet phase.

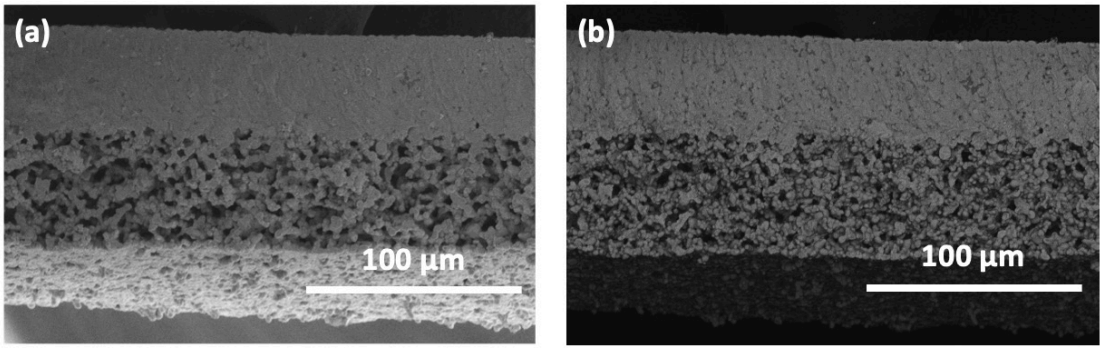


Figure 5.2. (a). Secondary electron mode and (b). back scatter electron mode SEM images of the as-synthesized bilayer Ta-LLZO. The dense layer and porous layer thickness are 40 and 55 μm, respectively.

GPE preparation: LiFSI (99.9%, Alfa Chemistry) was vacuum dried at 120°C for 24 hours before use. DOL (99.8%, Millipore Sigma) and DME (99.5%, Millipore Sigma) solvents were dried by 4 Å molecular sieves (Millipore Sigma) for at least 3 days before use. The liquid solutions of 1M/2M/3M LiFSI in DOL were drop-casted on the dense side of the bilayer LLZO, followed by heating to 45°C overnight and then resting at 22℃ for 24 hours in a low illumination environment to enable DOL polymerization. After that, a solution of 1M LiFSI in DME was drop casted on top of the polymerized DOL, creating the GPE. The solutions of 1M/2M/3M LiFSI in DOL and solution of 1M LiFSI in DME were mixed in volume ratios of 1:1. All preparations were performance in an Ar-filled glovebox.

SPAN cathode preparation: Elemental sulfur (S, Millipore Sigma) and polyacrylonitrile (PAN, Mw. ~ 151,000, Millipore Sigma) was mixed with a mass ratio of 8:1 and high-energy ball milled overnight. After that, the S and PAN mixture was heated to 300 °C at a heating rate of 5°C/min, held at 300 °C for 7.5 hours under flowing Ar, and then cooled to 25℃. The obtained SPAN powder was mixed with carbon black (H.M. Royal Inc.) in a mass ratio of 8:2 and dispersed in N-Methyl-2-pyrrolidone (NMP, 99.5%, Millipore Sigma), followed by strong stirring to ensure uniform mixing. The SPAN/carbon black suspension was then drop cast onto a carbon felt to achieve a sulfur mass loading of 5.2 mg/cm^2, followed by drying at 100°C overnight in an Ar-filled glovebox with O_2 < 0.01 ppm and H_2O < 0.30 ppm. Sulfur made up 44 wt% of the SPAN material (Table 5.1) as determined by elemental analysis using a carbon and nitrogen analyzer with experimental details shown in characterization part.

Table 5.1. The Elemental Analysis of Carbon and Nitrogen in SPAN powder

Element	Weight %
C K	40.7
N K	14.6

* The sulfur weight percentage based on the elemental analysis is S(*wt.%*) + H(*wt.%*) = 100%–41%–15%= 44.7%, which is consistent with EDX point scanning results.
**Considering that Hydrogen makes up ~1 *wt.%* of the SPAN total mass(22) and cannot be detected by elemental analysis, a final sulfur weight percentage of 44% is used for specific capacity and energy density evaluations.

Electrochemical Measurement: 2032 type coin cells (MTI Corp.) were used for all battery cycling measurements, which were conducted using an Arbin BT 2000 instrument. The coin cells were rested at 22℃ for at least 24 hours before cycling. The voltage cutoffs were set to 1V and 3.2V (vs. Li^+/Li), followed by a constant voltage charge at 3.2V until current fell to 0.087 mA/cm^2. The current density of 0.435 mA/cm^2 was used during constant-current charge process for all the battery tests. The cell capacity was calculated based on the mass of sulfur in SPAN. EIS measurements for calculating GPE conductivity were performed by a Solartron 1260 Impedance/Gain-phase Analyzer with a voltage amplitude of 25 mV and a frequency range of 0.1 MHz to 100 Hz, and a stainless steel/GPE/stainless steel cell configuration was used. The EIS measurements were performed in the Ar-filled glovebox. The ionic conductivity of the GPE was calculated using Ohm's law: $\sigma = \frac{1}{R}\frac{L}{A}$, where R, A, and L were the total resistance, the area and the thickness of the GPE, respectively, The GPE/LLZO interfacial EIS was measured by using a Bio-logic VSP-300 potentiostat. The areas

used of ASR/conductivity calculations were taken to be the SPAN cathode area. Impedance curve fitting was performed using the Z-fit software.

Characterizations: (1). SEM and EDX images were captured with a Tescan GAIA FEG SEM. All samples are washed with NMP and dried before characterization. (2). ATR-FTIR was recorded by NEXUS 670 FTIR instrument. The background signal was subtracted before any ATR-FTIR measurement. (3). The elemental analysis was conducted by LECO 628 carbon nitrogen analyzer. Samples were combusted at 950℃ and CO_2 was measured by infrared detection, while nitrogen gas was measured by thermal conductivity. Analytical results were reported as percent carbon (%C) and percent nitrogen (%N) and calculated from the mass of the sample placed inside a Tin sample cup. (4). TEM observation was performed on JEM 2100F (JEOL, Japan) at 200 keV. All samples were washed by NMP solvent and dried before characterization. (5). XRD was performed using a C2 Discover diffractometer (Bruker AXS) with a Cu Kα radiation source (λ = 1.54056 Å) operated at 40 kV and 40 mA. The samples were rinsed by NMP and DME solvents before XRD measurements. (6). All the samples were transferred to He glove box in a sealed bag prior to XPS measurements. The glove box atmosphere was kept < 0.1 ppm O_2 and < 0.0 ppm H_2O. The samples were loaded on a ca. 2 cm diameter puck with Cu tape and transferred to XPS chamber without air exposure using air-tight transfer vessel. XPS spectra were obtained with the Kratos Axis Ultra^{DLD2} using monochromatic Al Ka (10 mA, 15 kV). XPS scans were carried out at 20 eV pass energy. Charge neutralizer was used during the measurements with

[2] Certain commercial equipment, instruments, materials, suppliers, or software were identified in this paper to foster understanding. Such identification does not imply recommendation or endorsement by the National Institute of Standards and Technology, nor does it imply that the materials or equipment identified are necessarily the best available for the purpose.

filament current of 1.8 A and charge balance of 2.5 V. XPS spectra was analyzed with CasaXPS(82). All the spectra were referred to C 1s peak of hydrocarbon at 284.8 eV. Tougaard-type background was subtracted before deconvolution and analysis of the peaks.

5.3 Results and Discussions

5.3.1 *In-situ* Gel Polymer Electrolyte

Figure 5.3a shows a schematic of our innovative GPE/Ta-LLZO hybrid electrolyte. A thin ZnO layer was deposited on both sides of the bilayer Ta-LLZO to improve wetting between the Li metal and the Ta-LLZO (on the anode side)(57, 81) with an average thickness of ~9 nm. During cell fabrication, we observed that the ZnO also improved the wetting between the GPE and the Ta-LLZO (on the cathode side). The GPE interlayers were synthesized with three different LiFSI salt molar concentrations of 1M, 2M, and 3M. For the sake of brevity, the mixtures will be referred to as “1M GPE”, “2M GPE”, and “3M GPE”, respectively.

The GPE was characterized by ATR-FTIR in Figure 5.3b. Within the fingerprint region (i.e., below 1500 cm^{-1}), the 1M GPE showed -O-C- stretching of the DOL (i.e., the GPE precursor) transmittance peak at 1080 cm^{-1}, indicating the presence of residual unpolymerized precursor. In contrast, no residual unpolymerized precursor was observed in the ATR-FTIR spectra for the 2M GPE and 3M GPE, indicating they were completely polymerized. Additional detail regarding the GPE peaks is provided in Table 5.2.

Table 5.2. The ATR-FTIR details of the GPE

Wavenumber (cm^{-1})	**Interpretations**	**Ref.**
748 and 833	-C-H bending of poly-DOL	(120)
916	-C-H out of plane stretching of DOL	(121)
1080	-O-C stretching of DOL	(121)
1103	-OLi edging group of poly-DOL	(122)
1176 (after adding DME)	-O-C- stretching of DME	(123)

The average GPE thickness is 2.5–3 μm. The conductivity of the GPEs was measured using EIS. From the Nyquist plot in Figure 5.3c, the average ionic conductivity of 1M, 2M, and 3M GPE at 22℃ was 5.6, 4.5, and 3.5 mS/cm, respectively (Figure 5.4). Because of their high conductivity, the average area specific resistance (ASR) of the bulk 1M, 2M, and 3M GPEs contributes only 4.7, 5.6, and 8.6 ohm-cm^2, to the total cell ASR.

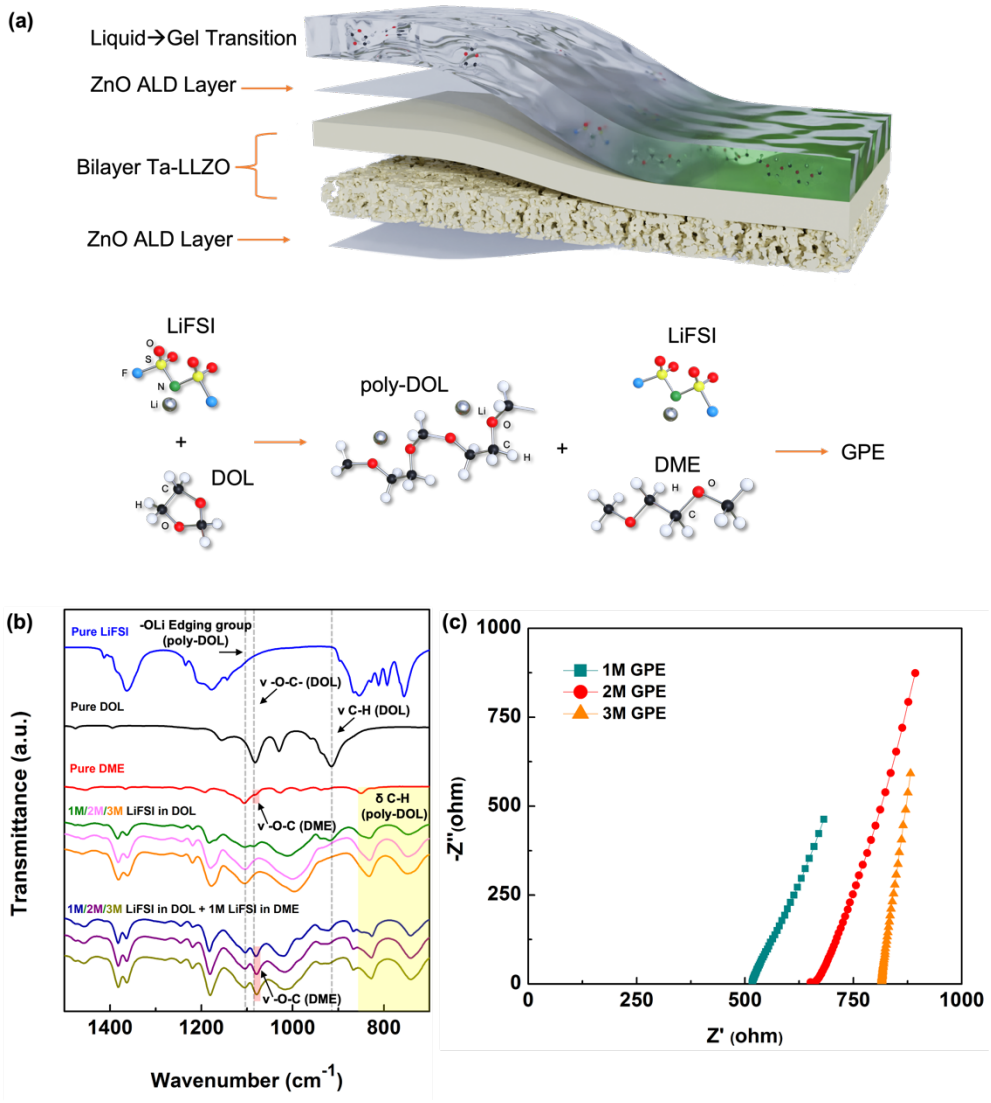


Figure 5.3. (a) Schematic illustration of our cell configuration and the in-situ formed GPE on the bilayer LLZO. (b). The ATR-FTIR of the pure LiFSI, DOL, poly-DOL, DME and the GPE. (c). EIS measurement of different concentrated GPE. The frequency range is from 0.1MHz to 100 Hz with an amplitude of 25 mV.

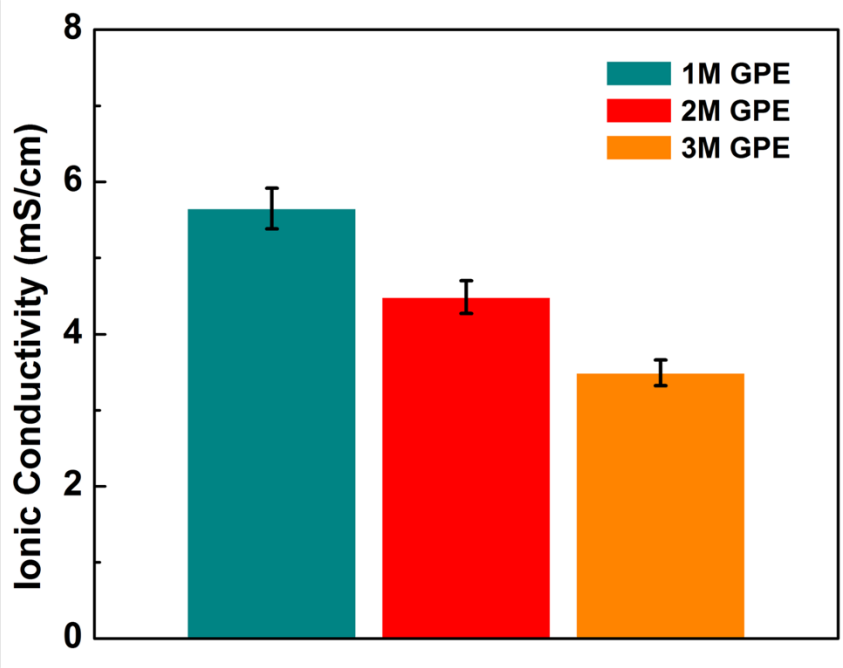


Figure 5.4. The ionic conductivity of different GPEs.

The impedance of the GPE/Ta-LLZO interface (for 1M, 2M, and 3M) and the GPE/SPAN cathode interface was also measured (Figure 5.5). The equivalent circuit of these systems are shown in Figure 5.5a and Figure 5.5b. The overall interfacial ASR between the GPE and the Ta-LLZO was 31 ohm-cm^2 (1 M) (Figure 5.5c), 46 ohm-cm^2 (2 M) (Figure 5.4d) and 63 ohm-cm^2 (3 M) (Figure 5.5e), respectively. The overall interfacial ASR between the GPE and the SPAN cathode was very low, measuring only 3.5 ohm-cm^2 (1 M), 4 ohm-cm^2 (2 M), and 5.5 ohm-cm^2 (3 M), respectively (see Figures 5.5f–g).

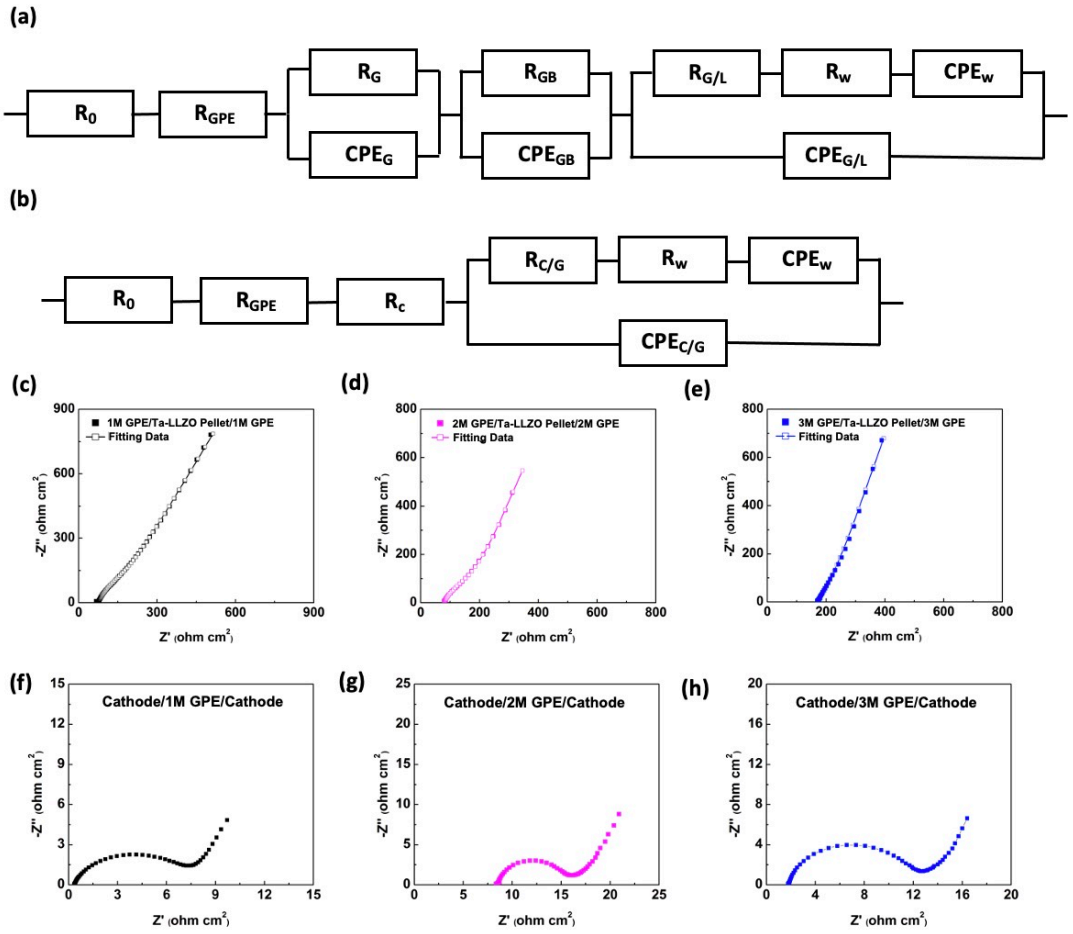


Figure 5.5. The interfacial impedance between the GPE and Ta-LLZO. (a). Equivalent circuit of the Stainless Steel (SS)/GPE/Ta-LLZO pellet/GPE/Stainless Steel (SS) cell configuration. R_0 is the environmental resistance and R_{GPE} is the resistance contributed from GPE. R_G, R_{GB}, $R_{G/L}$, R_W is the resistance of bulk Ta-LLZO, Ta-LLZO grain boundary, interface between GPE and Ta-LLZO and the Warburg resistance, respectively. CPE_G, CPE_{GB}, $CPE_{G/L}$ and CPE_W are the constant phase element of Ta-LLZO grain, Ta-LLZO grain boundary, the interface between GPE and LLZO and Warburg diffusion tail, respectively. (b). Equivalent circuit of the SPAN cathode/GPE/GPE/SPAN cathode cell configuration. R_0 is the environmental resistance. R_C, $R_{C/G}$, R_W is the resistance of the SPAN cathode, interface between SPAN cathode and GPE and the Warburg resistance, respectively. $CPE_{C/G}$ and CPE_W are the constant phase element of the interface between SPAN cathode and GPE and Warburg diffusion tail, respectively. The analytical approach was the same here as in our previous

publication(1). (c–e) are the EIS of the SS/1M GPE/Ta-LLZO pellet/2M GPE/SS, SS/2M GPE/LLZO pellet/2M GPE/SS and SS/3M GPE/LLZO pellet/2M GPE/SS symmetric cell, respectively. The frequency was from 1MHz to 100 Hz. (f–h) are the EIS of the SPAN cathode/1M GPE/SPAN cathode, SPAN cathode/2M GPE/SPAN cathode and SPAN cathode/3M GPE/SPAN cathode symmetric cell, respectively. The frequency was from 1MHz to 1 Hz.

The GPE/LLZO interfacial resistance ($R_{G/L}$) was tested through GPE/LLZO/GPE symmetric cell and calculated using the following equation:

$$R_{G/L} = \frac{R_{tot} - R_0 - R_{GPE} - R_G - R_{GB}}{2}$$

The GPE/SPAN cathode interfacial resistance ($R_{G/L}$) was tested through SPAN cathode/GPE/SPAN cathode symmetric cell and calculated using the following equation:

$$R_{G/L} = \frac{R_{tot} - R_0 - R_{GPE} - R_C}{2}$$

5.3.2 Electrochemical Performance of GPE/Bilayer Ta-LLZO Cells

The electrochemical cycling performance of all our garnet Li-S cells was tested at 22 ℃ using a high sulfur mass loading of 5.2 mg/cm^2 and different GPE concentrations. The 1M GPE cell was unable to properly cycle due to an infinitely long charge time (Figure 5.6a) at a discharge/charge current density of 0.87/0.435 mA/cm^2. Conversely, both the 2M and 3M GPE cells charged and discharged normally as shown in Figure 5.6b–f, Figure 5.7 and 5.8. The performance of different cells for long cycling test in this work were summarized in Table 5.3.

Table 5.3. Electrochemical performance of different pairs of 2M and 3M GPE cells

Cell Type (Cell Number#)	Discharge Current Density (mA/cm^2)	Discharge Capacity (mAh/g)	CE (%)	Energy Density (Wh/kg/Wh/L)
2M GPE (#1)	0.87	1542 (1379)	100.3	223/769
3M GPE (#2)	0.87	1312 (1316)	98.4	185/647
2M GPE (#3)	1.74	1367 (1218)	99.3	199/686
3M GPE (#4)	1.74	1266 (1116)	100.1	173/604

* The charge current density for all the cells was 0.435 mA/cm^2. The energy density was calculated based on the initial discharge capacity.
** For the discharge capacity, it is listed as initial (average) discharge capacity.
*** CE is Columbic Efficiency.

EIS measurements show that the 2M and 3M GPE cells had total ASR values of only 105 ohm-cm^2 and 124 ohm-cm^2, respectively (Figure 5.9). Figure 5.6b–d illustrate the long-term cycling performance of the 2M (cell #1) and 3M GPE (cell #2) cells discharged at 0.87 mA/cm^2 at 22℃. The 2M GPE cell demonstrated high initial capacity of 1542 mAh/g with an average capacity of 1379 mAh/g over 60 cycles. Similarly excellent performance was shown by the 3M GPE cells, with an average capacity of 1316 mAh/g. Both the stability under cycling and the magnitude of battery

capacity (under high sulfur mass loading and high current density) suggest that a stable cathode/electrolyte interface was successfully formed with almost no capacity fade for 60 cycles. Unfortunately, cell #1 and #2 testing was disrupted by a lab power loss after 60 cycles resulting in premature cell failure.

In Figure 5.6e the cycling stability of both the 2M (cell #3) and the 3M (cell #4) GPE remained after increasing the discharge current density to 1.74 mA/cm^2. The average discharge capacity of the 2M GPE cell was 1218 mAh/g for the first 265 cycles with 80% capacity retention. The average discharge and charge voltage was 1.73 V and 2.26 V, respectively. Note that, the 80% capacity retention was calculated after the capacity of cell #3 was stabilized at the 5th cycle. The 3M GPE cell had an average discharge capacity of 1116 mAh/g over 200 cycles.

In Figure 5.6f, the capacity recoverability of the 2M GPE design was evaluated using cell #5 for a sequence of discharge current densities:1.74 mA/cm^2 (0.2C, 1C = 1670 mA/g), 2.61 mA/cm^2 (0.3C), 4.35 mA/cm^2 (0.5C), 8.7 mA/cm^2 (1C) and then back to 1.74 mA/cm^2 (0.2C), with 10 cycles for each condition. It was observed that the average discharge capacity for the 10 cycles at 8.7 mA/cm^2 was as high as 1015 mAh/g, 74 % of the average discharge capacity (1375 mAh/g) at 1.74 mA/cm^2. When the cell was switched from 8.7 mA/cm^2 back to 1.74 mA/cm^2, the final average discharge capacity was 1293 mAh/g, which was comparable to the initial average discharge capacity observed for the first 10 cycles at 1.74 mA/cm^2. (The voltage profile of the rate test is shown in Figure 5.86.) This demonstrates that even relatively high C-rates for Li-S cells are possible with our GPE-stabilized sulfur cathode/Ta-LLZO interface.

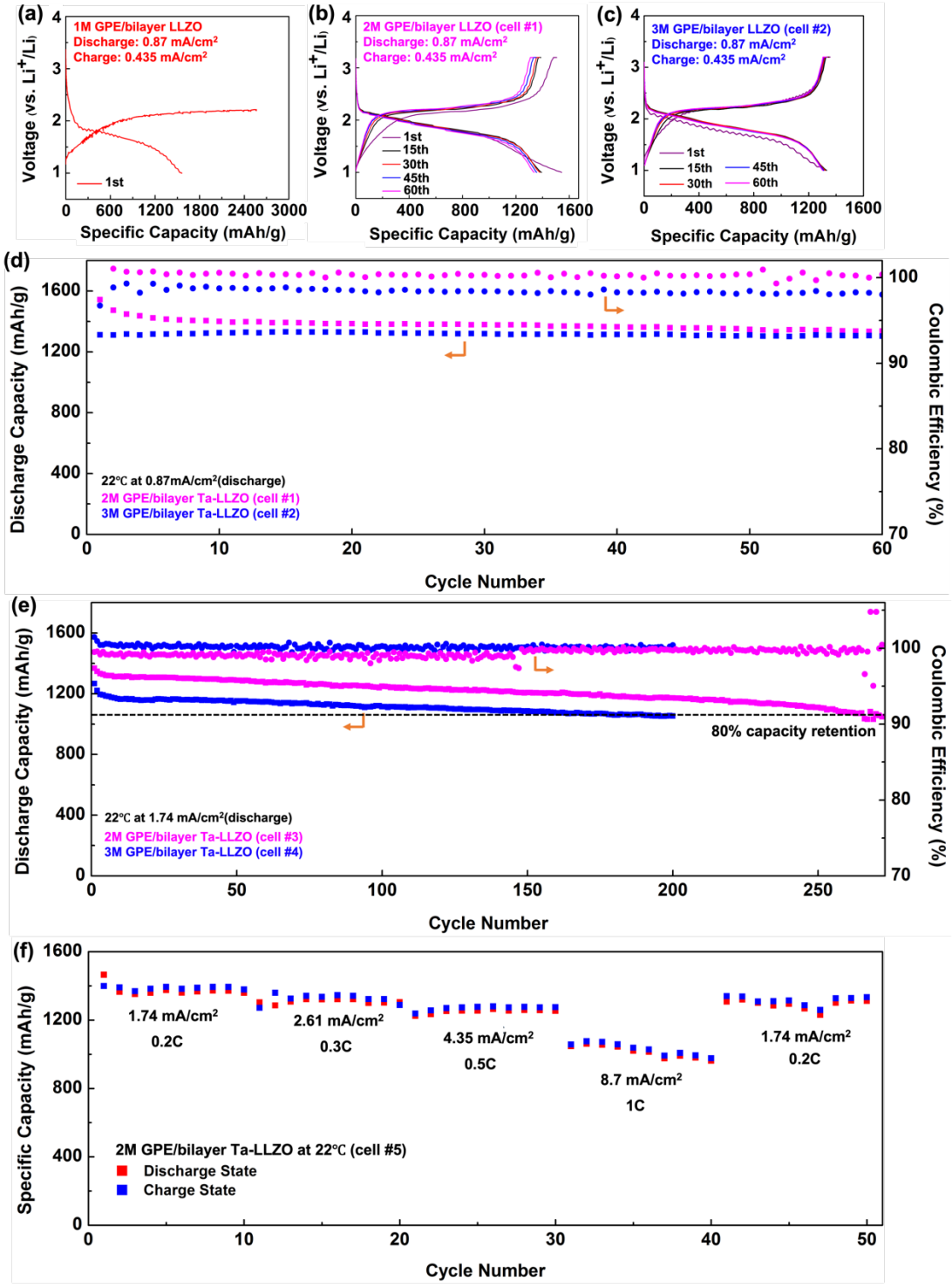


Figure 5.6. The electrochemical performance tests of our GPE/bilayer Ta-LLZO designs. (a) The voltage profile of the 1M GPE cell. The charge process cannot be

finished. (b) and (c) Cycling performances of 2M and 3M GPE cells, respectively. (d) Cycling performances of 2M and 3M GPE cells. The discharge and charge current density for (a)–(d) are 0.87 mA/cm^2 and 0.435 mA/cm^2, respectively. (e). Cycling performances of 2M and 3M GPE cells at a discharge current density of 1.74 mA/cm^2. (f). Capacity recoverability/C-rate performances of the 2M GPE design ranging from 1.74 mA/cm^2 to 8.7 mA/cm^2 and then back to 1.74 mA/cm^2. Note that, c-rate is based on the theoretical capacity of elemental sulfur.

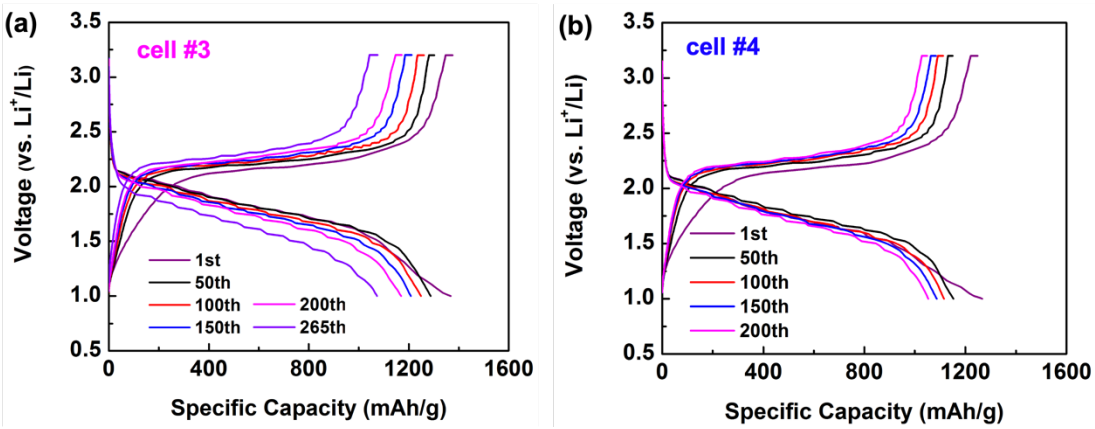


Figure 5.7. The voltage profile of the (a) 2M GPE/bilayer Ta-LLZO and of (b) the 3M GPE/bilayer Ta-LLZO with an optimized cycling voltage window at a discharge current density of 1.74 mA/cm^2.

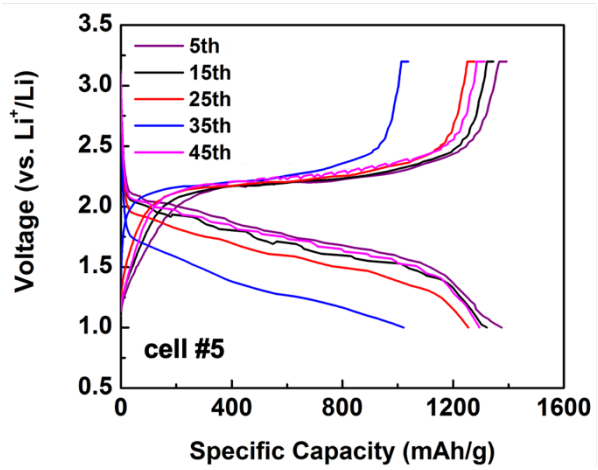


Figure 5.8. The voltage profile of the capacity recoverability test of Figure 5.6f. The current density (discharge/charge) of cell #5 at the 5th, 15th, 25th, 35th and 45th cycle

is 1.74/0.435, 2.61/0.435, 4.35/0.435 and 1.74/0.435, respectively. The current density unit is mA/cm^2.

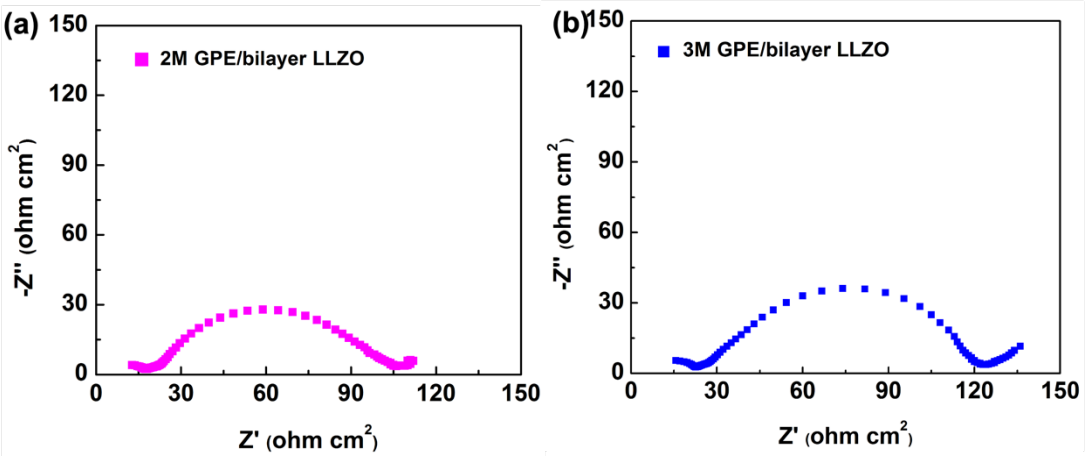


Figure 5.9. The electrochemical characterizations of GPE/bilayer LLZO Li-S batteries. (a) and (b) are the EIS measurement of 2M and 3M GPE/bilayer Ta-LLZO batteries before cycling at 22℃ with an amplitude of 10 mV and a frequency range of 7 MHz to 0.01 Hz, respectively.

5.3.3 Cell Performance Comparison

Achieved cycle number, average discharge capacity and energy density are critical factors for battery performance evaluation. Cell #3 (Figure 5.6e), which achieved an average discharge capacity of 1218 mAh/g for over 265 cycles, outperformed previously published garnet Li-S cells, as shown in Figures 5.10a and 5.10b.

Similarly, cell #1 produced a high initial discharge capacity of 1542 mAh/g (Figure 5.6d) at 0.87 mA/cm^2, which corresponds to an energy density of 223 Wh/kg (769 Wh/L), shown in Table 5.3 and Figures 5.10 b–d. This is among the highest values reported for garnet Li-S cells to date. Moreover, by simply reducing the dense layer

thickness to our previously demonstrated 10 μm(*28*), we can project an energy density of 296 Wh/kg (924 Wh/L), as indicated in Figures 5.10c and 3d. Energy density calculations can be found in Table 5.4. A comparison of our work with state-of-art results for garnet Li-S cells is shown Table 5.5.

In addition, for a projected Ta-LLZO dense-layer thickness of 10 μm, further energy density projections based on different sulfur loading (mg/cm^2) are shown in Figure 5.11. For example, for a sulfur loading of 7.5 mg/cm^2 as we previously demonstrated(*29*), an energy density of 361 Wh/kg and 1116 Wh/L is achievable.

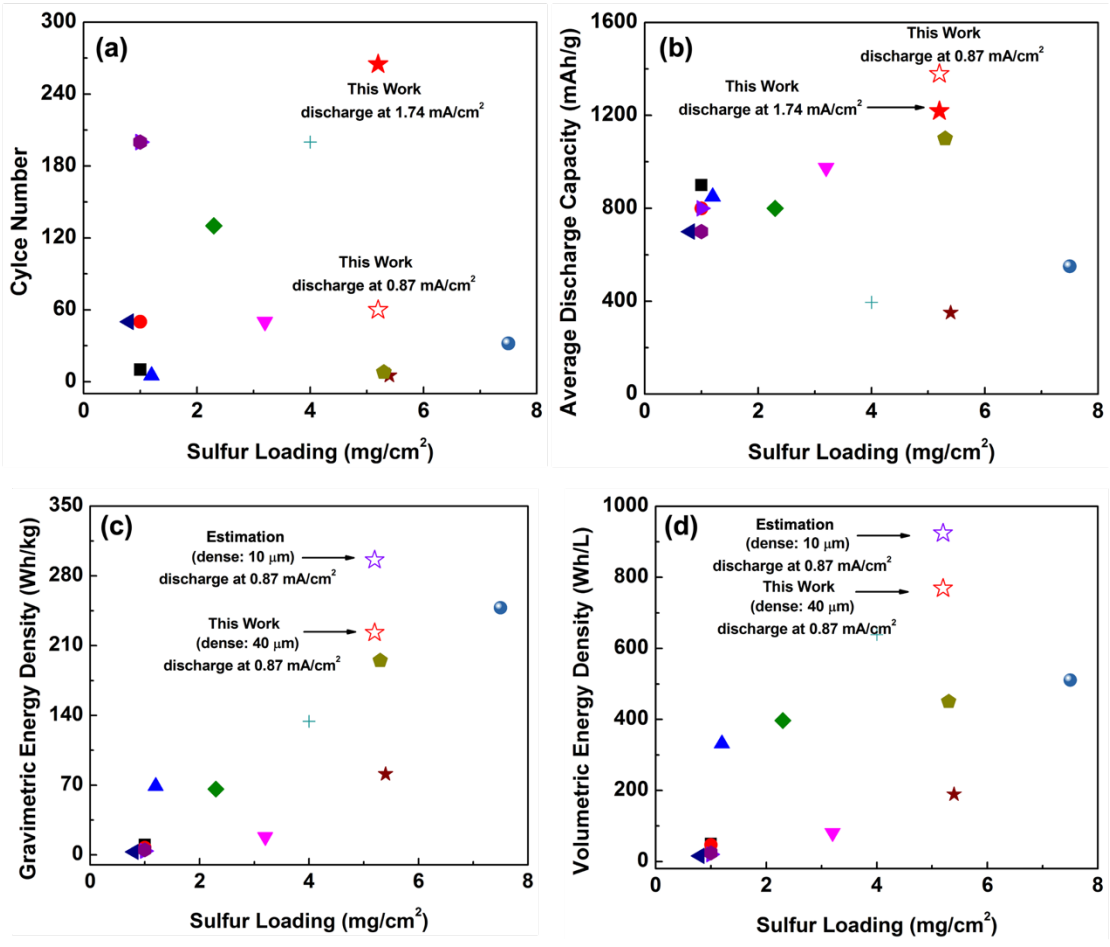


Figure 5.10. Cell performance evaluation. (a), (b) and (c–d) are the comparison of total number of cycles, average discharge capacity and energy density, respectively. Note that, open stars and solid stars indicated the demonstrated and projected energy densities, respectively. Note that, in Figure 3c–d, the open and solid red stars represented the achieved energy density based on initial and average capacities, respectively. The open and solid violet stars represented the projected energy density based on initial and average capacities, respectively. The detailed values are quantified in Table 5.5 with references cited.

Table 5.4. The demonstrated energy density of the 2M GPE/bilayer Ta-LLZO design based on initial discharge capacity

Material	**Mass (mg/cm^2)**	Density (g/cm^3)	**Volume ($\mu L/cm^2$)**	Average Energy (Wh/cm^2)	Charge (mAh)
SPAN	**11.8**	1.18	**5.59**	13.74	8.68
Carbon	**3**	1.80	**1.67**		
2M SPE	**7.19**	N/A	**0.00**		
Liquid electrolyte	**5.25**	1.06	**0.00**		
Ta-LLZO	**32.00**	5.00	**9.50**		
Li-metal	**2.25**	0.53	**1.11**		8.68
Total	**59.00**		**17.87**		
				Energy Density (Wh/kg)	223
				Energy Density (Wh/L)	769

*For a dense layer thickness reduced to 10 μm, the total mass of the bilayer Ta-LLZO is lowered to 17 mg/cm^2.
** In reality, 150–200% excess Li metal was used in making cells to get a good physical contact between stainless steel spacer and Li metal after melting. This 150–200% excess Li metal led to a thickness and capacity of ~63–85 μm and 13–17 mAh/cm^2, respectively. However, this excess amount of Li can be reduced or eliminated by engineering-level adjustment.

1). For all calculations, the sulfur weight content of 44% in the SPAN electrode is applied which keeps consistent with the elemental analysis results.

2). The capacity match is used to get the amount of Li metal needed for the battery designs.

$$m(Li) = \frac{m(sulfur) \times c(sulfur)}{c(Li)}$$

where $m(Li)$ and $m(sulfur)$ are the areal mass of Li and sulfur (5.2 mg/cm^2), respectively. $c(Li)$ and $c(sulfur)$ are the capacity of Li (3860 mAh/g) and of sulfur (1670 mAh/g).

$$m(Li) = \frac{m(sulfur) \times c(sulfur)}{c(Li)} = \frac{5.2\ mg/cm^2 \times 1670\ mAh/g}{3860\ mAh/g}$$
$$= 2.55\ mg/cm^2$$

3). The volume of the SPAN cathode is the same as PAN polymer host that confine the active sulfur materials.

4). GPE eventually can be absorbed by the cathode or fill the pores of the cathode which does not contribute additional volume when calculating the volumetric energy density.

Table 5.5. A comparison of our work with the state-of-art published results

Electrolyte	Sulfur Loading (mg/cm^2)	Discharge (mA/cm^2)	Cycles	Discharge Capacity (mAh/g)*	Energy Density (Wh/kg/Wh/L)*	Ref.
LE*/LLZO	1	0.1	10	~1000 (~900)	10/50	(124)
LE/LLZO	1	0.2	50	~850 (~800)	8/47	(124)
LE/LLZO	1.2	0.36	5	900 (~850)	69/332	(66)
LE/LLZO	3.2	0.3	50	1000 (~975)	18/81	(101)
LE/LLZO	2.3	0.19	130	1250 (~800)	66/397	(96)
LE/LLZO	0.8	0.08	50	1150 (~700)	3/16	(97)
LE/LLZO	1	0.334	200	~1150 (~800)	4/20	(100)
LE/LLZO	1	0.2	200	1190 (~700)	5/24	(99)
LE/trilayer LLZO	5.4	1.62	5	350 (350)	81/189	(69)
Ionic liquid /trilayer LLZO	5.3	0.22	8	1244 (~1100)	195/450	(57)
LE/bilayer LLZO	7.5	0.2	32	645 (55)	248/511	(58)
PEO / bilayer LLZO	4	0.2	200	1307 (395)	134/639	(119)
2M GPE (#1)	5.2	0.87	60	1542 (1379)	223/769	This work
2M GPE (#3)	5.2	1.74	265	1367 (1218)	199/686	This work

* For the discharge capacity, it is listed as initial (average) discharge capacity.
**The energy density listed in the Table 5.5 was calculated based on the initial discharge capacity.
***All the above results are tested at a temperature range of 22℃–25℃, and our work which was conducted at 22℃. (2). LE is short for liquid electrolyte which is 1M LiTFSI in DOLDME with or without $LiNO_3$ additive.

In addition, when considering the dense layer thickness to be 10 μm, further energy density projection based on different sulfur loading (mg/cm^2) are shown in Figure 5.11. For example, when the sulfur loading would be 7.5 mg/cm^2 as we demonstrated(58), a high energy density of 361 Wh/kg and 1116 Wh/L could be achieved.

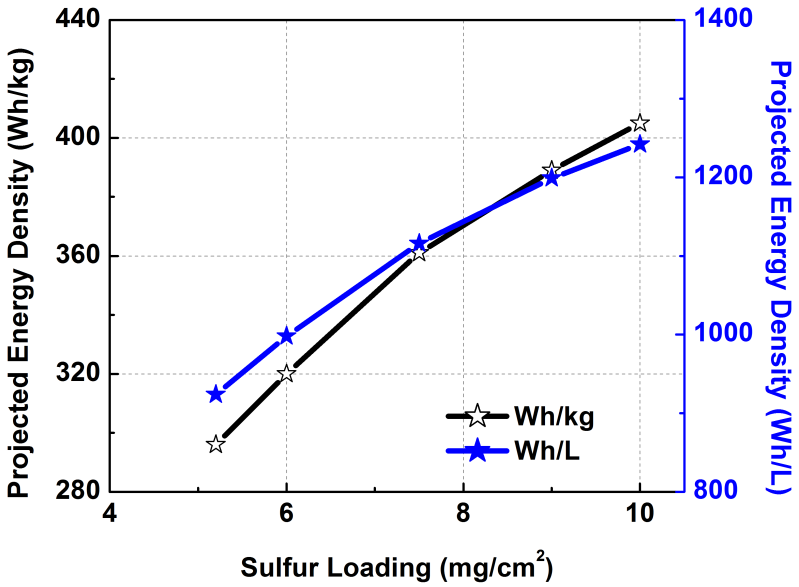


Figure 5.11. The further energy density prediction versus sulfur mass loading by using the dense layer thickness to be 10 μm in the bilayer Ta-LLZO.

* The assumptions to obtain the values in Figure 5.11 include:

- Considering the balance between sulfur loading and the sulfur utilization, the sulfur utilization was reduced by ~1% when sulfur loading increased by 1 mg/cm^2 as indicated in our previous results(125).
- The projected energy density as calculated based on capacity matching the anode Li with the cathode sulfur.
- An average discharge voltage 1.715 V was used, the same as the average discharge voltage to get the capacity of 1542 mAh/g under a sulfur loading of 5.2 mg/cm^2.
- Keep all other parameters the same as Table 5.4.

5.3.3 Cell Stability Characterization

X-Ray Diffraction (XRD) scans were used to study the phase stability of the bilayer Ta-LLZO after battery cycling. As shown in Figure 5.12, pure cubic Ta-LLZO was well maintained after cycling the 1M, 2M, and 3M GPE cells, indicating there was no crystal structure changes in the Ta-LLZO during the SPAN de-lithiation/lithiation process. These measurements confirmed the phase structure stability of the Ta-LLZO in our GPE/bilayer Ta-LLZO design.

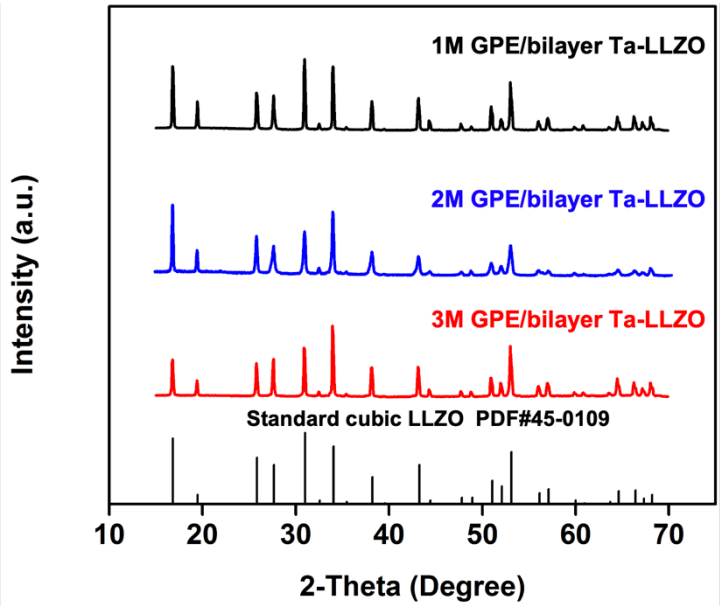


Figure 5.12. The XRD pattern of the 1M/2M/3M GPE/bilayer Ta-LLZO after cycling. All of them showed a pure cubic LLZO phase without impurity.

Interfacial decomposition between Ta-LLZO and GPE due to electrochemical reactions were investigated by X-ray photoelectron spectroscopy (XPS). Figure 5.13 shows the C 1s and F 1s spectra of Ta-LLZO which confirm the prolonged charging issue in 1M GPE compared to the cycled charge-discharge in 3M GPE. The largest difference of the decomposition between 1M GPE cells and 3M GPE cells was in the comparative magnitude of the fluorinated carbon peak in the XPS spectra. In the C 1s spectra, the lowest binding energy peak is a hydrocarbon at 284.8 eV(*30*). A peak at 286.2 eV is attributed to C-O bonds(*31*), which is likely from decomposed GPE. A peak at 288.3 eV is attributed to ketones(*31*), and a peak around 289.7 eV is attributed to carbonates(*31*). Ketones and carbonates are expected to be decomposition products from GPE. In contrast the C 1s spectra from 3 M GPE (Figure 5.13 (b)), a prominent peak of fluorinated carbon(*31*) is observed, while the peak of fluorinated carbon in 1

M GPE shown in Figure 5.13 (a) is very small. The higher amount of fluorinated carbon in 3 M GPE cell compared to the 1 M GPE cell suggests that the there was a greater amount of fluorinated decomposition products formed at LLZO surface at higher concentrations.

In the F 1s spectra, a peak around 684.8 eV is attributed to LiF(*30*, *31*). The amount of LiF increased for the 3 M GPE (Figure 5.13d) to nearly double the amount in 1 M GPE (Figure 5.13c). A peak around 688.3 eV is attributed to decomposed FSI(*20*) and a peak around 689.4 eV is attributed to fluorinated carbons(*30*, *31*). The amount of fluorinated carbon in F 1s is significantly higher in 3 M GPE than 1 M GPE, which is consistent with the results from C 1s spectra. The peak areas of decomposed FSI and fluorinated carbon relative to LiF peak area are larger in 3 M GPE than 1 M GPE. The increase in the ratio of decomposed FSI and fluorinated carbon over LiF indicates that there was difference in decomposition process of FSI.

As indicated in both F 1s and C 1s spectra, increased amount of LiF, fluorinated carbon and decomposed FSI were observed in 3 M GPE compared to 1 M GPE. The ratio of fluorinated carbon and decomposed FSI with respect to LiF was higher in 3 M GPE than 1 M GPE. This suggests that the electrochemical reaction at Ta-LLZO surface is concentration dependent. This difference in the electrochemical reactions may have contributed to successful charging and good capacity retention of 2M and 3M GPE cells. 2M and 3M GPE did not show a prolonged charging issue as 1 M GPE. This suggests that the change of the electrochemical reactions due to higher concentration helped to stabilize the Ta-LLZO surface.

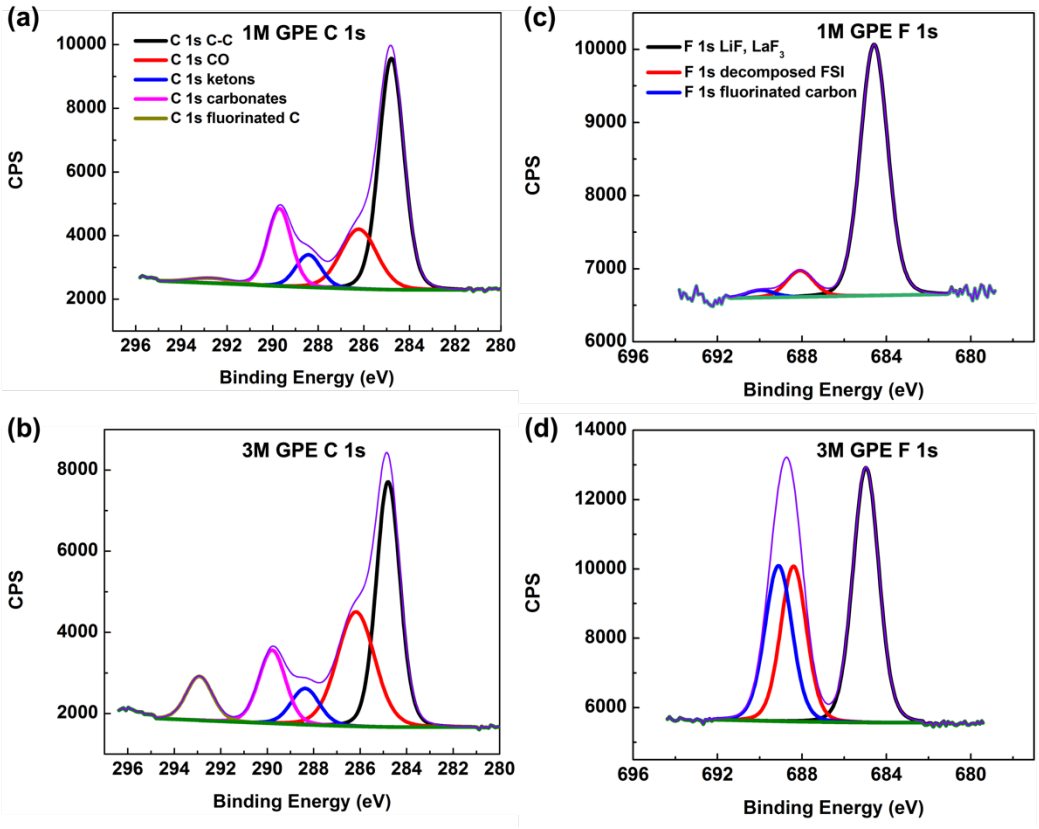


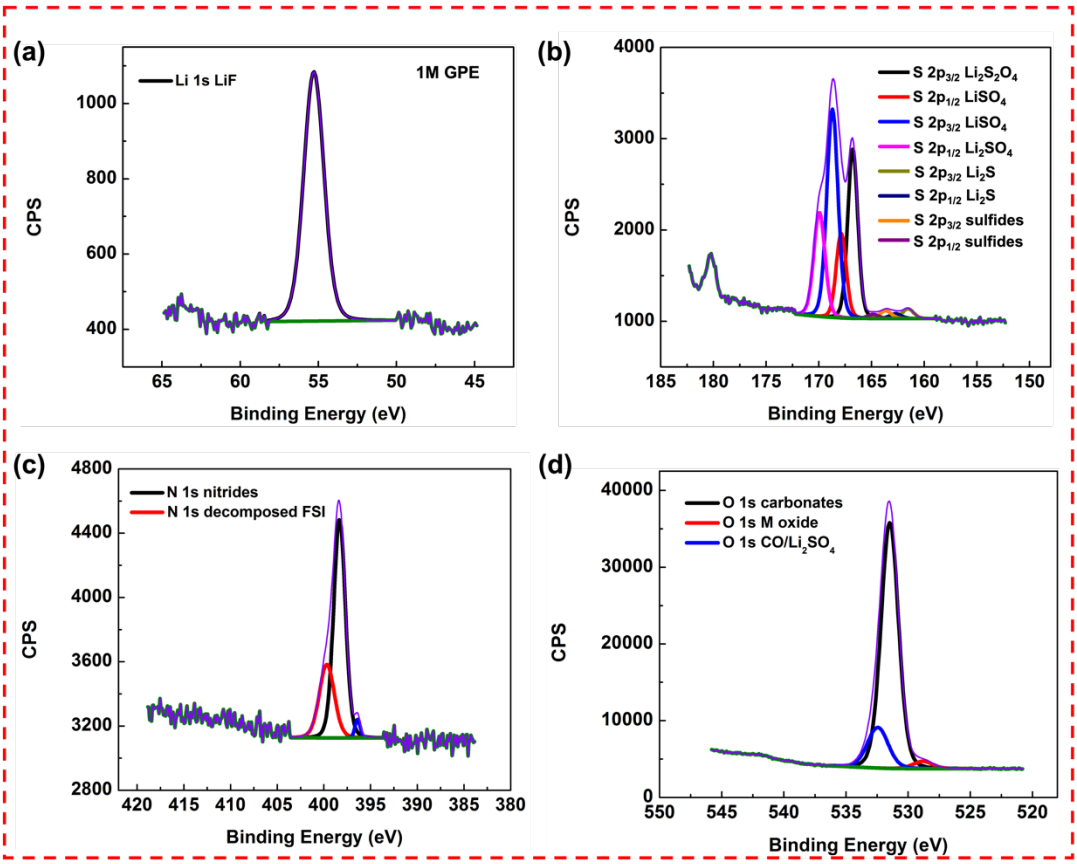
Figure 5.13. XPS analysis on the electrochemical decomposition between Ta-LLZO and GPE through XPS. C 1s and F 1s spectra of Ta-LLZO charged in 1M GPE and cycled in 3M GPE. (a) and (b) shows C 1s spectra of 1M GPE and 3M GPE, respectively. (c) and (d) shows F 1s spectra of 1M GPE and 3M GPE, respectively. The same color was used for the same decomposed compounds in C 1s and F 1s spectra for 1M and 3M GPE to be easy for comparison.

The Li 1s, S 2p, N 1s, O 1s spectra of 1M GPE (Figure 5.14a–d) and 3 M GPE (Figure 5.14e–h) are shown in Figure 5.14, respectively. Li salts such as LiF, LiOH, Li_2CO_3, Li_2O(83) and Li in Ta-LLZO(117) can show the peak around 55.5 eV where the peak is observed in the Li 1s spectrum. Based on the observation of F 1s spectrum, the peak likely includes LiF, however, does not exclude other components because of the close vicinity of the expected peak positions.

The area ratio of S $2p_{3/2}$ and S $2p_{1/2}$ peaks were fixed to its theoretical area ratio for fitting S 2p spectra. S $2p_{3/2}$ peaks at 168.9 eV, 166.9 eV, 163.6 eV, and 161.6 eV are attributed to Li_2SO_4, $Li_2S_2O_4$, sulfides, and Li_2S(83, 108), respectively.

In the N 1s spectra, a peak at 398.6 eV is attributed to nitrides(83) and a peak at 399.9 eV is attributed to decomposed FSI(119). Compared to N 1s spectra from 1 M GPE (Figure 5.14c), area of a peak attributed to decomposed FSI increased with the amount of FSI increased. The result is consistent with the increased amount of F observed in F 1s spectra of 3 M GPE compared to 1 M GPE.

In the O 1s spectra, the largest peak at 531.7 eV is attributed to carbonates(108), and the second largest peak at 532.6 eV is attributed to ethers and/or Li_2SO_4(108). ethers and Li_2SO_4 peaks were not clearly distinguishable due to close vicinity of expected peak positions, but both components are expected to be present at the studied surface based on C 1s spectrum indicating C-O and S 2p spectrum indicating Li_2SO_4. A shoulder at 528.8 eV is attributed to metal oxides(83).


(a)
Li 1s LiF
1M GPE
CPS
Binding Energy (eV)
(b)
S 2p3/2 Li2S2O4
S 2p1/2 LiSO4
S 2p3/2 LiSO4
S 2p1/2 Li2SO4
S 2p3/2 Li2S
S 2p1/2 Li2S
S 2p3/2 sulfides
S 2p1/2 sulfides
CPS
Binding Energy (eV)
(c)
N 1s nitrides
N 1s decomposed FSI
CPS
Binding Energy (eV)
(d)
O 1s carbonates
O 1s M oxide
O 1s CO/Li2SO4
CPS
Binding Energy (eV)

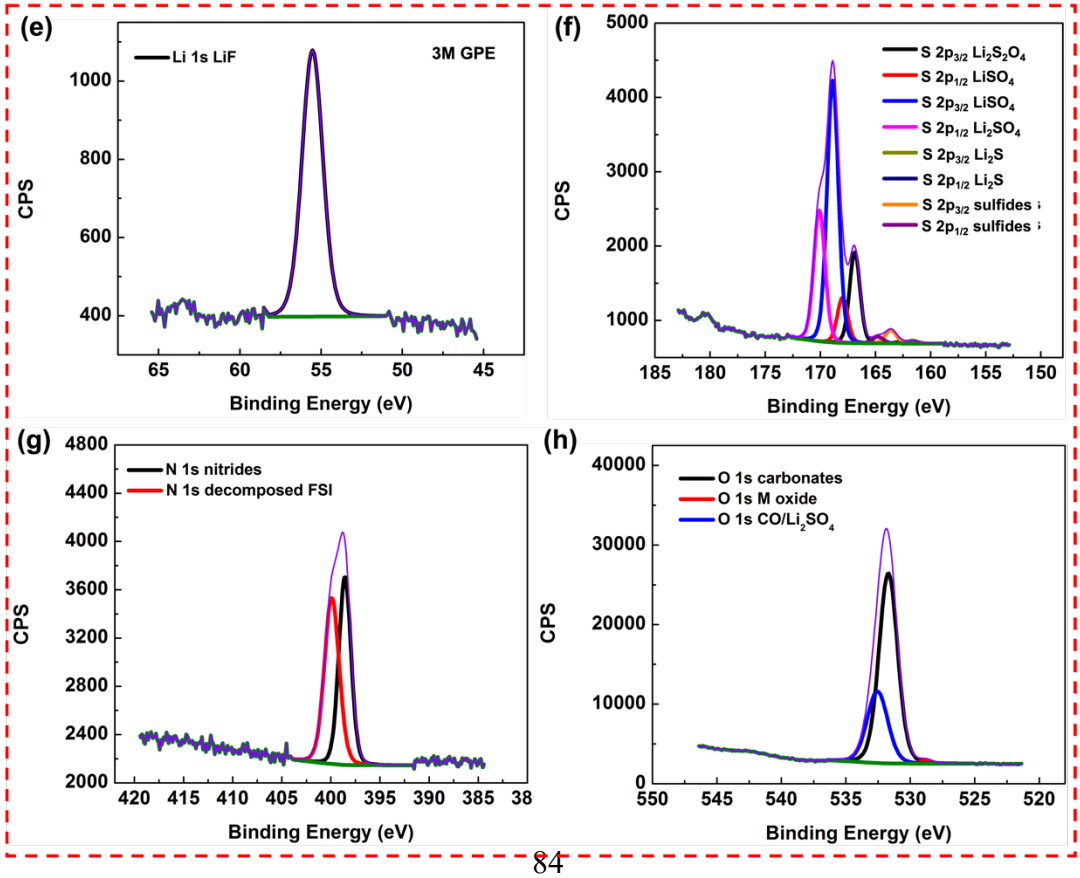

(e)
Li 1s LiF
3M GPE
CPS
Binding Energy (eV)
(f)
S 2p3/2 Li2S2O4
S 2p1/2 LiSO4
S 2p3/2 LiSO4
S 2p1/2 Li2SO4
S 2p3/2 Li2S
S 2p1/2 Li2S
S 2p3/2 sulfides
S 2p1/2 sulfides
CPS
Binding Energy (eV)
(g)
N 1s nitrides
N 1s decomposed FSI
CPS
Binding Energy (eV)
(h)
O 1s carbonates
O 1s M oxide
O 1s CO/Li2SO4
CPS
Binding Energy (eV)

Figure 5.14. (a–d) Li 1s, S 2p, N 1s, and O 1s spectra of Ta-LLZO in 1M GPE having prolong charged issue. (d–h) Li 1s, S 2p, N 1s, and O 1s spectra of Ta-LLZO cycled in 3M GPE.

Based on the observations from Figure 5.13 and Figure 5.14, the list of components formed on the surface of LLZO are followings: Li salts (includes LiF, but may also include Li_2CO_3, Li_2O, LiOH), Li_2SO_4, $Li_2S_2O_4$, sulfides, Li_2S, ethers, ketones, carbonates, fluorinated carbons, nitrides, and decomposed FSI. While there was a larger amount of chemicals that are associated with FSI (fluorinated carbons, decomposed FSI) for 3M GPE the list of the observed components is the same for 1 M GPE and 3 M GPE.

All the XPS spectra of 2M GPE are shown in Figure 5.15. All the 2M GPE spectra look very similar with the ones in 3M GPE cases.

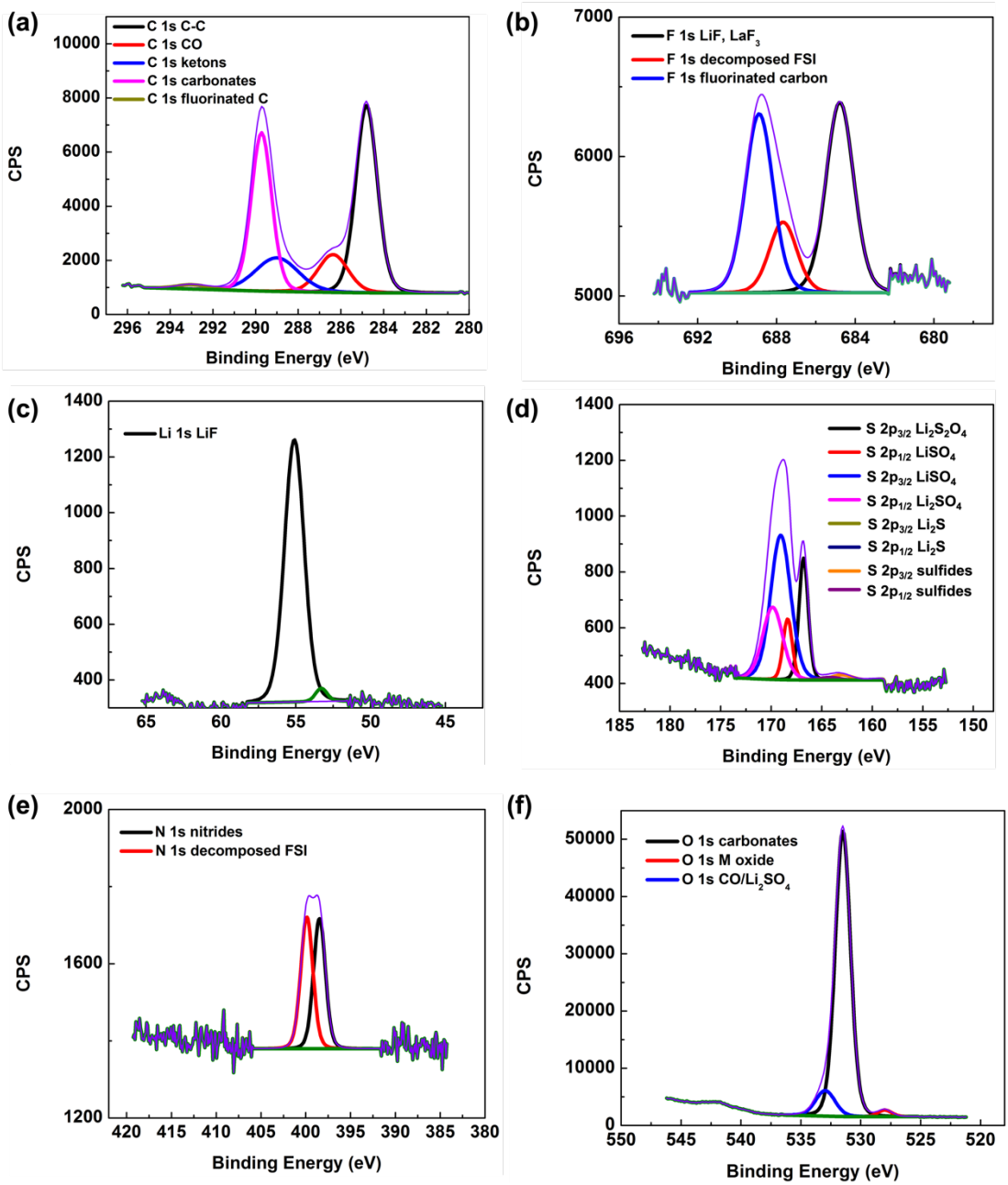


Figure 5.15. C 1s, F 1s, Li 1s, S 2p, N 1s, and O 1s spectra of Ta-LLZO cycled in 2M GPE.

The difference in the electrochemical reaction may be attributed to preferred FSI decomposition over decomposition of the solvents in 3M GPE, while decomposition of solvents was preferred over FSI decomposition in 1 M GPE. In a

similar system, LiTFSI /ACN system, it is reported that the decomposition reactions of an electrolyte differ with its concentration. It was shown by DFT-MD simulation that AN has the unoccupied molecular orbital that is the lowest in the electrolyte in 0.4 M LiTFSI/ACN, hence LUMO is determined by ACN. On the other hand, in 4.2 M LiTFSI/ACN, TFSI has the unoccupied molecular orbital that is the lowest in the electrolyte, not AN, hence LUMO is determined by TFSI at high concentration. Accordingly, decomposition of ACN is preferred in 0.4 M LiTFSI/ACN while TFSI anion decomposition is preferred in 4.2 M LiTFSI/ACN(126, 127). The changes of the surface reactions in high concentration electrolytes have been reported with various salts (LiFSI, LiTFSI, $LiPF_6$, $LiN(SO_2C_2F_5)_2$, $LiClO_4$, etc), various organic solvents (ACN, PC, DMSO, DME, ethylene carbonate (EC): diethyl carbonate (DEC), etc) and with various electrode materials (graphite, Li metal, Al, $LiNi_{0.5}Mn_{1.5}O_4$, $LiMn_2O_4$, etc)(126–136).

Assuming the same analogy of the DFT-MD simulation(*32*, *33*) can be applied, decomposition of FSI was preferred over decompositions of solvents for the 2M and 3M cell, leading to more LiF, fluorinated carbons and FSI decomposed products formed on Ta-LLZO surface that was characterized by XPS.

In addition to XPS spectra results, the ATR-FTIR spectra (Figure 5.3b) also shows that, there is -O-C- stretching (1080 cm^{-1}) contributed from DOL in the 1M GPE cell. Again, this finding suggests the DOL was only partially polymerized in the 1M GPE. Accordingly, we infer that the incompletely polymerized 1M GPE still has liquid-like behavior, which allowed the sulfur cathode to come into direct contact with

the Ta-LLZO surface and react with a lanthanum-segregated secondary phase as we demonstrated in Chapter 4, eventually resulting in cell degradation.

The morphology of the SPAN cathode before and after cycling was characterized through SEM and EDX mapping. As shown in Figure 5.16a, the SPAN cathode of the 1M GPE/bilayer LLZO showed severe micro-cracking after discharging at 0.87 mA/cm^2 compared with pristine SPAN (Figure 5.16b). While no micro-cracking was visible in the SPAN cathodes of the 2M/3M GPE/bilayer LLZO. This suggested that even if the cells using 1M GPE/bilayer Ta-LLZO had been able to successfully cycle, they would likely have shown rapid capacity decay due to the physical breakdown of the SPAN cathode. In addition, at fully discharge/charged state, the SPAN cathodes in 2M/3M GPE/bilayer Ta-LLZO (Figure 5.17a–d) had almost the same morphologies as the pristine SPAN cathode (Figure 5.16b), with no micro-cracking or delamination visible. Maintaining intact cathode morphology was critical to achieving ultra-stable cycling performance(137). Higher magnification SEM and EDX mapping images and analysis regarding were shown in Figure 5.18. Particularly, Figure 5.18a–c show that the SPAN cathode particles still maintain almost the same as the pristine SPAN after cycling in both 2M/3M GPE/bilayer LLZO cases. In addition, it is also clear to see that the cathode particles are still tightened to the carbon fiber, although binder free sulfur compound cathodes were used in this study and after peeling off the SPAN from the outer part of the electrode (Figure 5.18d–i).

TEM images in Figure 5.17e–f revealed an amorphous cathode electrolyte interface (CEI) layer had formed in the 2M and 3M GPE/bilayer Ta-LLZO batteries during cycling and was approximately 4 nm and 5 nm thick, respectively. The thin

intimate and conformal CEI coating layer likely helped passivate the cathode surface, providing a stable cathode/electrolyte interface(138) and potentially helping to mitigate interfacial stress/strain associated with the sulfur volume expansion which can help intact particle contact.

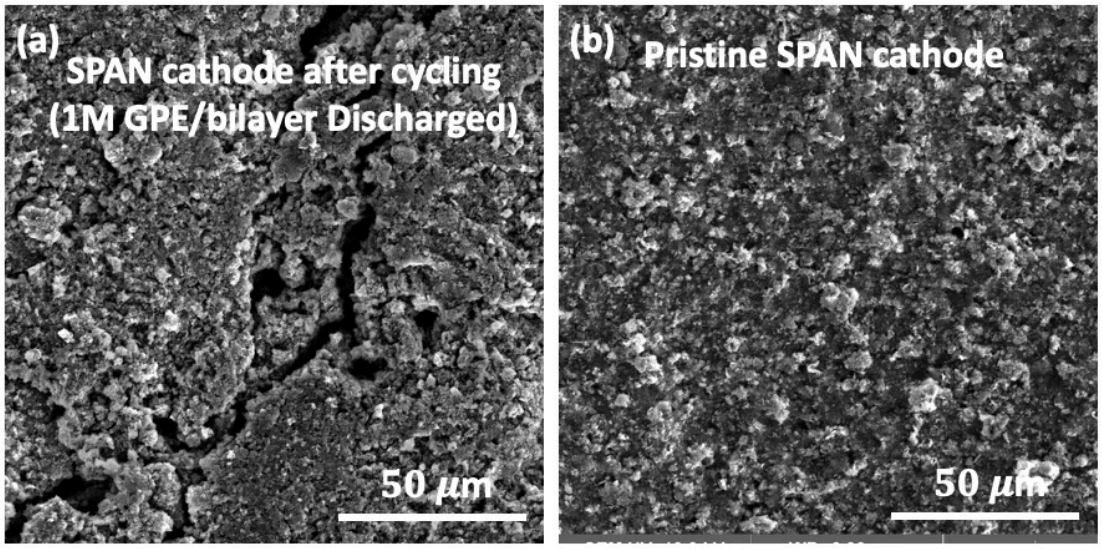


Figure 5.16. (a) The SPAN cathode after fully discharged at 1M GPE/bilayer-LLZO case configuration. (b) The SEM image of pristine SPAN cathode without electrochemical cycling.

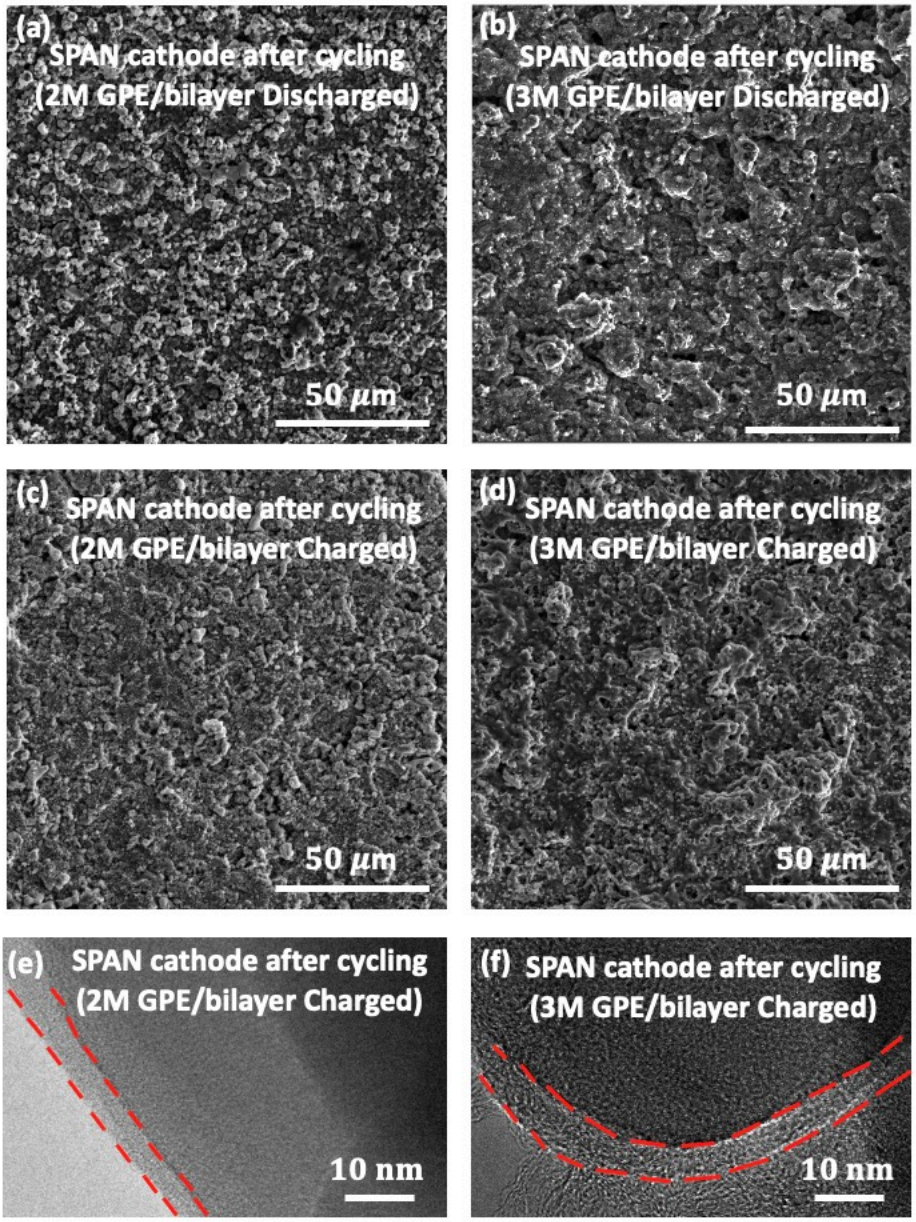


Figure 5.17. The morphology of SPAN cathode after cycling. (a–b). The SPAN cathode under fully discharged state with an applied discharge current density of 0.87 mA/cm^2 for 2M, and 3M GPE case, respectively. (c–d). The SPAN cathode after cycling under fully charged state for 2M and 3M GPE cells, respectively. (e–f) are the TEM images of SPAN after cycling in fully charged state for 2M and 3M GPE case, respectively.

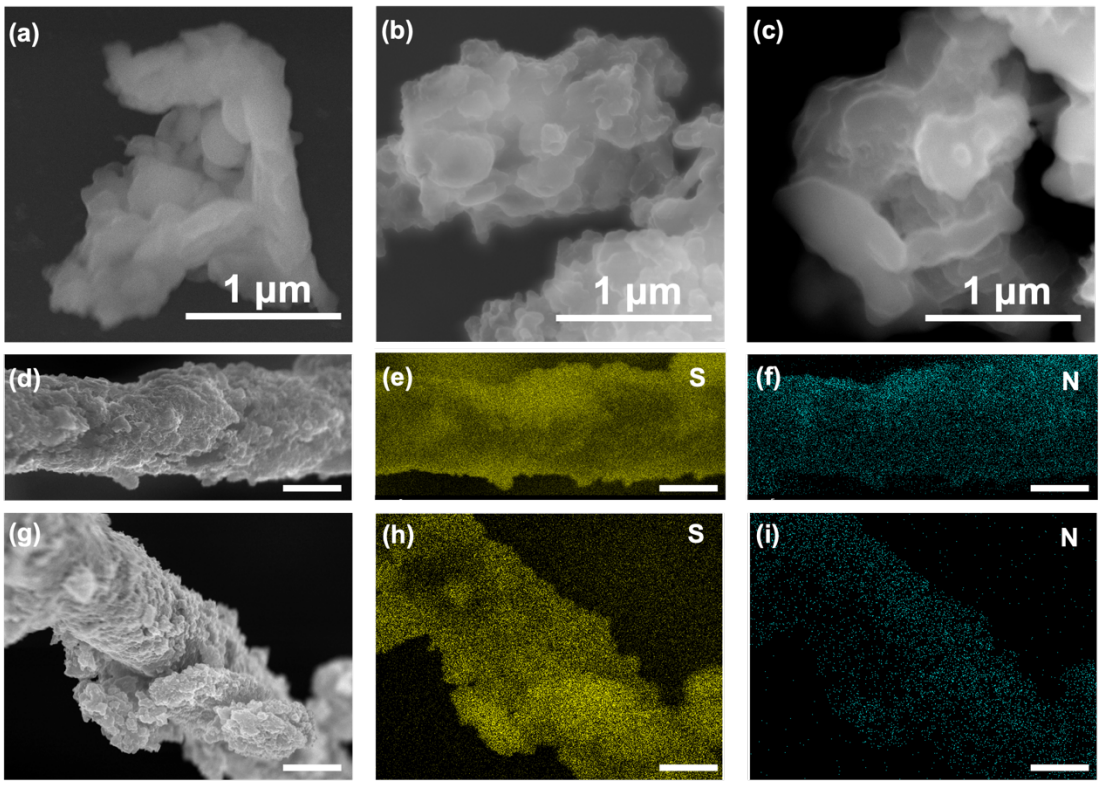


Figure 5.18. The morphology of SPAN cathode before and after cycling regarding SPAN particles and SPAN cathode coated on carbon fibers. (a). The pristine SPAN particles. (b) and (c) are the SPAN cathode after cycling of 2M/3M GPE/bilayer Ta-LLZO case, respectively. (d–f) and (g–i) are the SPAN coated on the carbon felt current collector after cycling of 2M GPE/bilayer Ta-LLZO and 3M GPE/bilayer Ta-LLZO case, respectively. The scale bar of (d–i) is 5 μm. The S and N mapping are intentionally selected because they are representative elements of SPAN. The SPAN cathode samples coated on carbon felt were prepared by peeling off the SPAN from the outer part of the electrode so that the SPAN cathode coated on the carbon felt can be exposed.

*5.4 **Conclusions***

By modifying the sulfur cathode/LLZO interface through the addition of an *in-situ* formed GPE electrolyte interlayer between LLZO and both 2M and 3M GPE, we

fabricated batteries that demonstrated stable performance and good energy densities. For the 2M GPE cells, we obtained a high initial discharge capacity of 1542 mAh/g discharged at 0.87 mA/cm^2, corresponding to an energy density of 223 Wh/kg and 769 Wh/L (cell #1). In addition, the 2M GPE cell (cell #3) could also deliver an average discharge capacity of 1218 mAh/g (80% capacity retention) over 265 cycles discharged at 1.74 mA/cm^2. This excellent electrochemical performance was principally due to the stabilized SPAN cathode/LLZO interface through the GPE interlayer. In particular, the preferred FSI decomposition over decomposition of the solvents in 2M and 3M GPE, compared to decomposition of solvents being preferred over FSI decomposition in 1 M GPE. In addition, the stabilized sulfur cathode/LLZO interface was also likely due to the formation of a completely intimate and conformal CEI coating layer that protected the sulfur cathode/LLZO interface and potentially helped mitigate the stress/strain generated by volume expansion of sulfur cathode. The stability and high performance obtained from this new battery architecture provide a promising pathway for the development of garnet-type solid-state Li-S batteries for practical applications requiring high energy densities and high cycling rates.

Chapter 6: All-Solid-State Garnet type Li-S Battery Enabled by Inorganic Conductive Lithium Salt and 3D Garnet Electrolyte Architectures

6.1 Introduction

In Chapter 4, we demonstrated a high initial discharge capacity of 1307 mAh/g at 22 ℃ by using a PEO-based interlayer on the cathode side and an ether-based catholyte. Later in Chapter 5, a gel polymer catholyte was introduced to further stabilize cell cycling performance at 22 ℃, achieving 80% capacity retention over 265 cycles using sulfur in the form of SPAN. With the novel bilayer LLZO architecture applied pressure is not necessary for cell operation. However, the flammable catholyte used to improve the sulfur-cathode/LLZO interface compromises the safety of such solid-state cells. Therefore, it is desirable to replace the hybridized garnet Li-S cells with all-solid-state garnet Li-S cells.

In this work, we have designed a novel three-phase cathode consisting of sulfur active material (Sulfur/Li redox material: SPAN), electronic conductive carbon (graphene nanoribbons, from NTherma Corporation are trademarked as NGraphene wires (NGW^{TM})) and LiFSI to improve the SPAN/SPAN particle contact, lower the contact resistance of the cathode/LLZO interface and to provide ionic conductivity in the composite cathode. With a thin bilayer LLZO architecture(58, 81), we demonstrate all-solid-state garnet Li-S cell with stable cycling. In addition, with a thin 3D column LLZO architecture, we demonstrated high-energy-density Li-S cells(139).

*6.2 **Experimental***

LLZO Synthesis: the synthesis process for bilayer Ta-doped LLZO was based on the synthesis process for Nb-doped LLZO discussed in our previous publication(58), with the Ta precursor replacing the Nb precursor. The preparation of 3D column LLZO architecture was as follow: the garnet inks were made by suspending cubic LLZO powder in ESL-441 (texanol-based) binder system along with an alpha-terpineol and ethyl-cellulose mixture. The final ink was 72 wt% LLZO powder, 21 wt% ESL-441, and 7% alpha-terpineol/ethyl-cellulose mixture. The inks were then printed/extruded with an nScrypt 3Dn-300 printer through a 75 μm tip onto a LLZO bilayer tape substrate. The prints were given 1 hour to settle in preparation for sintering. The sintering condition was the same as bilayer LLZO. The Li_2CO_3 on the surface of the LLZO samples was removed by heating the LLZO to 800℃ for 2 hours under inert gas flow. After that, the ZnO ALD coating layer was created using an ATHENA ALD system (Forge Nano Inc.).

SPAN synthesis: S_8 (Millipore Sigma) and PAN (Mw. ~ 151,000, Millipore Sigma) are mixed with a mass ratio of 8:1 in a high-energy ball mill overnight. After that, the S_8 and PAN mixture was heated to 300 °C at a heating rate of 5°C/min, held at 300 °C for 7.5 hours under flowing Ar with a gas pressure of 0.2 MPa, and then cooled to 25℃ with a cooling rate of 5°C/min.

Graphene nanoribbons from NTherma Corporation that are trademarked as NGraphene wires (NGW™): NGW™ was derived from chemical unzipping of multi-walled carbon nanotubes (MWCNTs). The chemicals used in unzipping the MWCNTs were $KMnO_4$ and H_2SO_4 in aqueous solution at 80℃, which was similar to previously

reported procedures(140). The MWCNTs were produced by NTherma Corporation by thermal chemical vapor deposition (CVD) with patented method and process(141), which involved growing the MWCNTs from Fe catalyst particles supported on a stainless steel foil in a roll-to-roll fashion. The MWCNTs were mechanically extracted from the metal foil at the interface of the MWCNTs and the metal surface, resulting in MWCNTs with a consistent length that could be controlled by changing the CVD growth processing conditions. The NGW™ was produced by unzipping the MWCNTs without any purification process of the MWCNTs. The length of the NGW™ used in this study was 20 μm (+/- 10%).

Composite cathode preparation: All the following steps were carried out in an Ar-filled glovebox with O_2 < 0.01 ppm and H_2O < 0.20 ppm.

(1). For the SPAN+NGW™ two-phase cathode: NGW™ (NTherma Corporation) was dispersed in N-Methyl-2-pyrrolidone (NMP, Millipore Sigma), drop-casted on the dense side of the thin LLZO bilayer to obtain an areal loading of ~ 1 mg/cm^2 and then dried. Then SPAN and NGW™ were mixed with a mass ratio of 4:1 and dispersed in NMP, followed by stirring for 24 hours to get a uniformly dispersed cathode suspension. The SPAN-NGW™ cathode suspension was drop-casted onto the NGW™-coated LLZO bilayer to obtain a sulfur loading of 1 mg/cm^2, followed by drying at 130℃.

(2). For the three-phase cathode using NGW™ as the carbon source: NGW™ was dispersed in NMP, drop-casted on the dense side of the thin LLZO bilayer to obtain an areal loading of ~ 1 mg/cm^2 and then dried. Then SPAN powder was mixed with LiFSI (Alfa Chemistry) with a mass ratio of 1:1. The mixture was ground manually

using a mortar and pestle. The as-collected powder was mixed with NGW^{TM} with a mass ratio of 8:1 in DME (Millipore Sigma), followed by stirring for 24 hours to get a uniformly dispersed cathode suspension. The SPAN-LiFSI-NGW^{TM} three-phase cathode suspension was drop-casted onto the NGW^{TM}-coated LLZO bilayer to obtain a sulfur loading of 1 mg/cm^2, followed by drying at 22–45℃. Then 0.5M LiFSI in DME was drop-casted on top of the deposited SPAN-LiFSI-NGW^{TM} cathode and fully dried. The thermal stability of LiFSI after being dried in DME solvent was shown in Figure 6.1 through ATR-FTIR, which indicated that there is no thermal run-away or LiFSI decomposition during such heat treatment. For the composite cathode used in the demonstration of high-energy-density cell using 3D column LLZO architecture, the mass ratio of SPAN to NGW(TM) was 85:15 with a sulfur loading of 7 mg/cm^2 while keeping all other parameters the same. Regarding the heat treatment, the composite cathode was heated to 150 ℃ for five minutes on a hot plate and then cooled down.

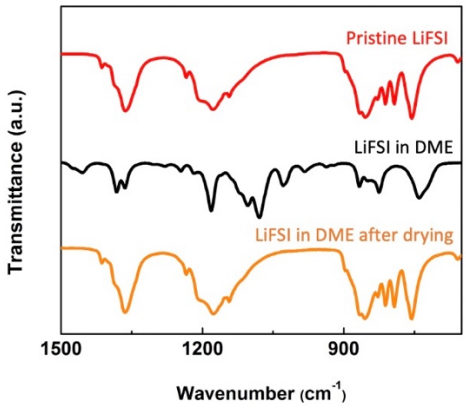


Figure 6.1. The ATR-FITR spectroscopy regarding the thermal stability of LiFSI salt after the DME solvent is evaporated. The spectra shows the LiFSI structure is maintained perfectly without any bonding change compared to the pure pristine LiFSI,

indicating there is no thermal runaway or decomposition behavior during the drying process(2–4).

(3). For the three-phase cathode using carbon black as the carbon source: the procedure was identical to the three-phase cathode using NGW™, but the NGW™ was instead replaced by an equal mass of carbon-black (H.M. Royal Inc.).

(4). For the LiFSI+ NGW™ cathode for CV measurement: NGW™ suspension was drop-casted on the dense side of the thin LLZO bilayer to obtain an areal loading of ~ 1 mg/cm^2 and then dried. Then LiFSI was spread on the surface of the NGW™-coated LLZO-bilayer and was melted at 150 ℃ for five minutes. While the LiFSI was in a molten state, the carbon felt current collector was placed on top of the molten LiFSI to enable good contact and then cooled down to 22 ℃.

Electrochemical Measurement: 2032 type coin cells were used for all cell cycling measurements, which were conducted using an Arbin BT 2000 instrument. The voltage cutoffs for full-cell testing were set to 1 V and 3.2 V (vs. Li^+/Li). EIS measurement of the conductivity of LiFSI was conducted through using a Bio-logic VSP-300 potentiostat with a stainless-steel/LiFSI/stainless-steel cell configuration. The conductivity of LiFSI was calculated through: $\sigma = \frac{1}{R}\frac{L}{A}$, where R, A, and L are the total resistance, the area, and the thickness of the LiFSI, respectively. The EIS measurement of all the Li-S full cells and the CV tests were also conducted by Bio-logic VSP-300 potentiostat.

Characterizations: All sample were prepared and packaged in the Ar-filled glovebox with O_2 < 0.01 ppm and H_2O < 0.20 ppm to avoid moisture contamination. In addition, all the samples were not washed by any solvents before characterizations.

(1) SEM and EDX images were captured with a Tescan XEIA FEG SEM. (2) TEM observation was performed with a JEM 2100F (JEOL, Japan) at 200 keV. (3) ATR-FTIR was recorded by NEXUS 670 FTIR instrument. The background signal was subtracted before each ATR-FTIR measurement. (4) XRD was performed using a D8 Discover diffractometer (Bruker AXS) with a Cu Kα radiation source (λ = 1.54056 Å) operated at 40 kV and 40 mA. The angle testing range was from 10° to 90° 2θ. A special XRD sample holder with a plastic dome that is gas tightened was used to prevent LiFSI from reacting with moisture and air. The SPAN+LiFSI composite samples for XRD and ATR-FTIR analysis were prepared in the same way as indicated in the cathode preparation section but without using NGW^{TM}. (5) The elemental analysis was conducted by LECO 628 carbon nitrogen analyzer to quantify the actual sulfur content in the SPAN powder. Samples were combusted at 950°C and CO_2 was measured by infrared detection, while nitrogen gas was measured by thermal conductivity. Analytical results were reported as %C and %N and calculated from the mass of the sample placed inside a Tin sample cup.

6.3 Results and Discussions

6.3.1 *Solid Catholyte Development*

To enable a fast charge transfer process in all-solid-state cells, a solid-state catholyte is necessary to enable Li^+ transport through the cathode structure and, moreover it must provide a continuous Li^+ path from/to the cathode active material (CAM). A number of inorganic solid-state catholyte materials have been investigated including $Li_{2.3}C_{0.7}B_{0.3}O_3$ (LCBO), Li_6PS_5Cl (LPS-Cl), Li_6PS_5Br (LPS-Br), and Li_6PS_5I

(LPS-I)(5, 6, 72, 142, 143). However, these were typically for co-sintering with oxide CAMs which enable a much higher sintering temperature than is possible for use with sulfur-based cathodes due to its limited thermal stability (e.g., S melts at 112.8°C and has a high vapor pressure). For example, Wang et al.(5) co-sintered a composite $LiCoO_2$ and LLZO cathode with LCBO at 700°C, well above the thermal stability limit of sulfur-based cathodes. Similarly, the majority of halide argyrodite catholytes require a high stacking pressure (i.e. >100 MPa) to have good CAMs/solid-state-catholyte contact and provide good cell performance(6, 72, 142, 143) which is not desirable for practical batteries and can be avoided using our novel bilayer/trilayer LLZO architectures(58, 69).

Therefore, in this study we introduced an inorganic Li salt, LiFSI, as a potential solid-state catholyte. As shown in Figure 6.2a and 6.2b, the LiFSI demonstrates an ionic conductivity of 1.9×10^{-5} S/cm at 22 ℃ and 1.2×10^{-4} S/cm at 60 ℃, one order of magnitude less than LLZO but still higher than some of the alternative solid catholytes (Figure 6.2b). Details of the ionic conductivity measurement setup and calculations are identical to those in literature(144, 145) and are discussed in the Methods Section in Supporting Information. LiFSI does not have significant electronic conductivity due to its wide bandgap (~5.9 eV) (85). Moreover, of particular importance to use with a sulfur cathode the low melting temperature (145 ℃) of LiFSI allows it to spread through the cathode matrix in the thermal stability range of SPAN (<200℃)(22, 146, 147).

The electrochemical stability of LiFSI as an ionically conductive material on the cathode side was characterized using cyclic voltammetry (CV) on a carbon-felt/LiFSI+NGW^{TM}/bilayer-LLZO/Li-metal cell (Figure 6.2c). A similar cell

configuration was previously used to determine the stability of LLZO and sulfide electrolyte(148). The cell was assembled by depositing NGW^{TM} onto the dense side of the pre-lithiated bilayer-LLZO, and then depositing LiFSI onto NGW^{TM}-coated side of the bilayer LLZO. The LiFSI was melted at 150°C and after which the cell was cooled to re-solidify the LiFSI and form a continuous Li^+ conducting path. In this configuration, no decomposition markers for LiFSI were observed between 1 V and 3.5 V (vs. Li^+/Li). The current observed between 100 mV and 900 mV was most likely due to the decomposition of LiFSI(149).

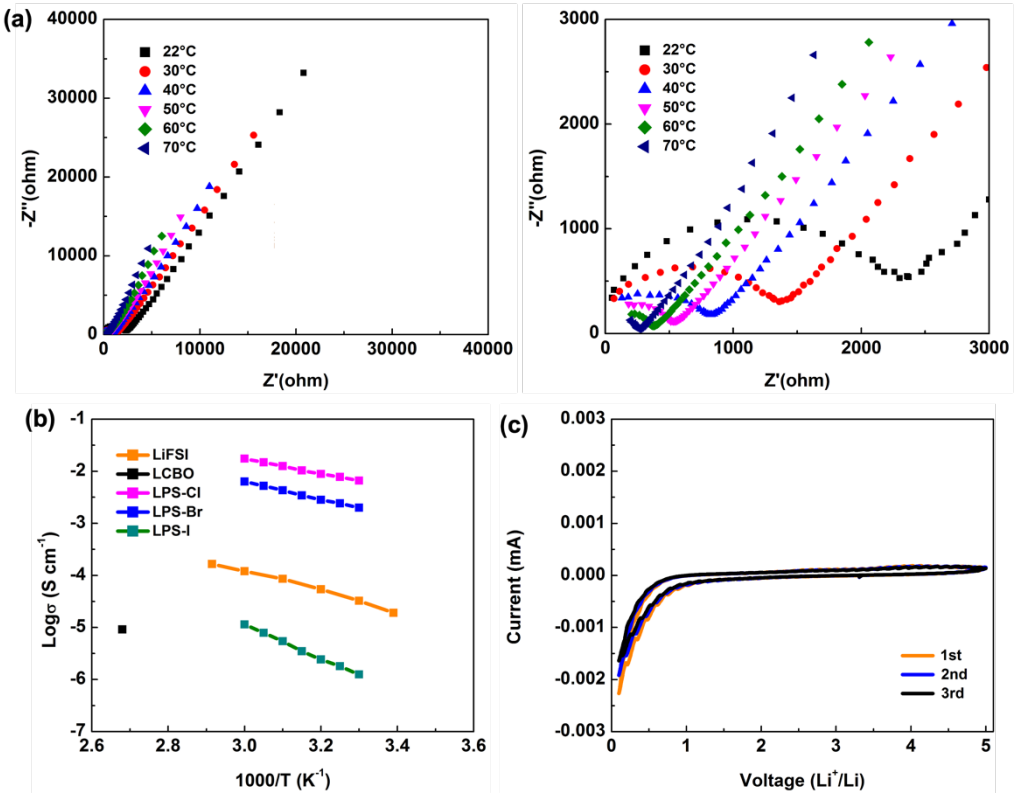


Figure 6.2. The electrochemical properties of pure LiFSI salt. (a). The Nyquist plot of a cell configuration of Stainless Steel (SS)/LiFSI/SS measured over the frequency range of 1MHz to 100 Hz and a voltage amplitude of 10 mV at different temperatures. The figure on the right is the zoomed-in version of the figure on the left. (b). The

experimentally measured ionic conductivity of LiFSI and the ionic conductivity of other solid-state catholytes reported in literature. Ionic conductivity data for $Li_{2.3}C_{0.7}B_{0.3}O_3$ (LCBO), Li_6PS_5Cl (LPS-Cl), Li_6PS_5Br (LPS-Br), and Li_6PS_5I (LPS-I) were extracted from the references(5, 6). (c). The electrochemical stability window of LiFSI obtained by cyclic voltammetry with a carbon-felt/LiFSI+NGW^{TM}/bilayer-LLZO/Li-metal cell. The voltage range was 100 mV to 5 V with a scanning rate of 0.1 mV/second.

6.3.2 *All-Solid-State Cathode Structure*

The design of our all-solid-state garnet Li-S cells is shown in Figure 6.3. SPAN was chosen as the CAM due to its higher electronic conductivity and more stable cycling performance compared to elemental sulfur(12, 150). However, the electronic conductivity of SPAN is not sufficient. To overcome this issue, we investigated carbon to provide the necessary electronic transport. Initial work using carbon black indicated issues with the cathode cracking (Figure 6.4). Therefore, we investigated longer carbon structures to alleviate this issue, specifically NGW^{TM}s. The individual NGW^{TM}s provided long-range mechanical support and electronic conductivity within the cathode (Figure 6.3), enabling heat treatment, and cycling of the cathode without cracking (Figure 6.4). Additionally, the longer NGW^{TM} microstructures had the potential to create continuous electronic conductive networks at a lower volume fraction than the discrete carbon-black particles, allowing for batteries with higher volumetric energy densities. The LiFSI then fills the pores in the cathode after it melts to improve the SPAN particle contact, lower the contact resistance of the cathode/LLZO interface and to provide ionic conductivity.

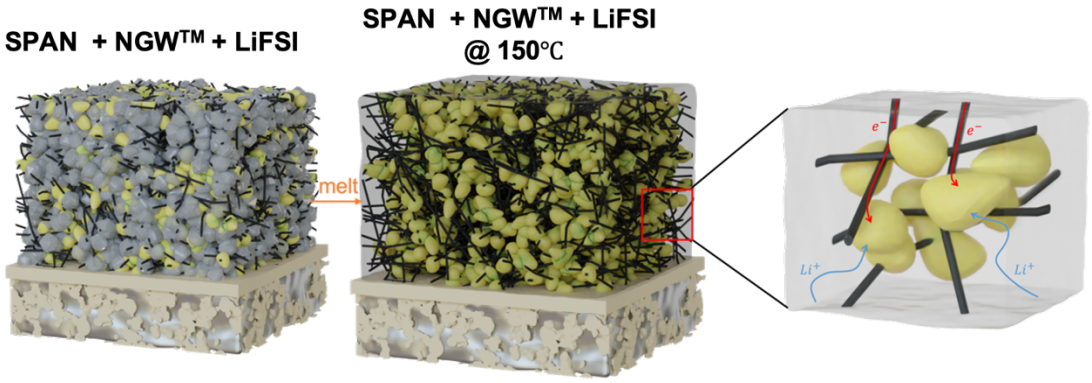


Figure 6.3. The schematics of the all-solid-state garnet type Li-S cells enabled by the novel three-phase cathode and bilayer-LLZO electrolyte architecture. The SPAN+NGW^{TM}+LiFSI composite cathode was obtained through melting the LiFSI in the SPAN+NGW^{TM}+LiFSI mixture and then cooled.

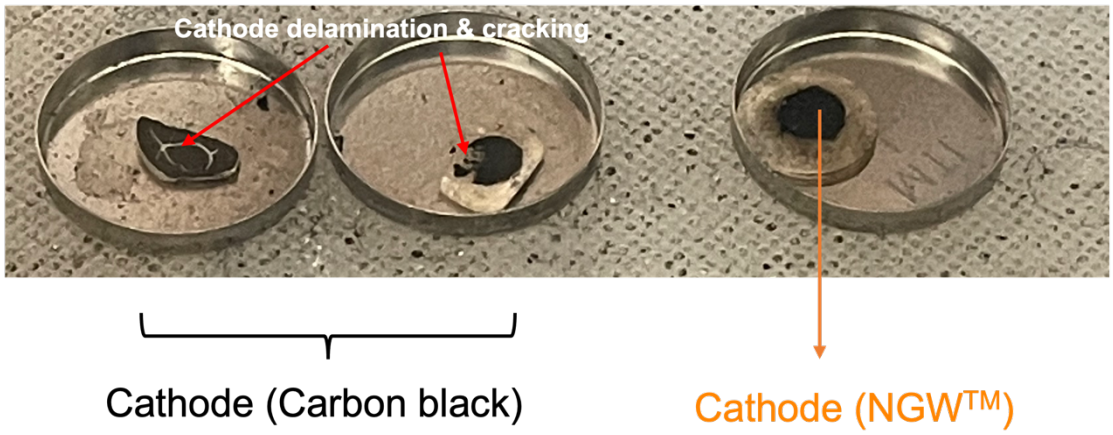


Figure 6.4. The optical image of three-phase cathode after heat treatment using carbon-black and NGW^{TM} as carbon source.

The phase stability and chemical stability between the SPAN and LiFSI were characterized through X-ray diffraction (XRD) and Attenuated Total Reflection-Fourier transform infrared spectroscopy (ATR-FTIR). The XRD pattern for the SPAN+LiFSI composite after heat treatment (Figure 6.5a) showed peaks corresponding to pure SPAN and pure LiFSI, indicating the heat treatment used to

develop the cathode did not induce crystallographic changes in the LiFSI or SPAN. ATR-FTIR characterization of the SPAN+LiFSI composite (Figure 6.5b) showed that the vibrational bonding behavior below 1500 cm^{-1} was identical before and after the heat treatment. Moreover, the SPAN+LiFSI composite did not show any new bonding vibrations compared with pure LiFSI and pure SPAN. This is further evidence that there was no chemical reaction between LiFSI and SPAN during the heat treatment of the cathode.

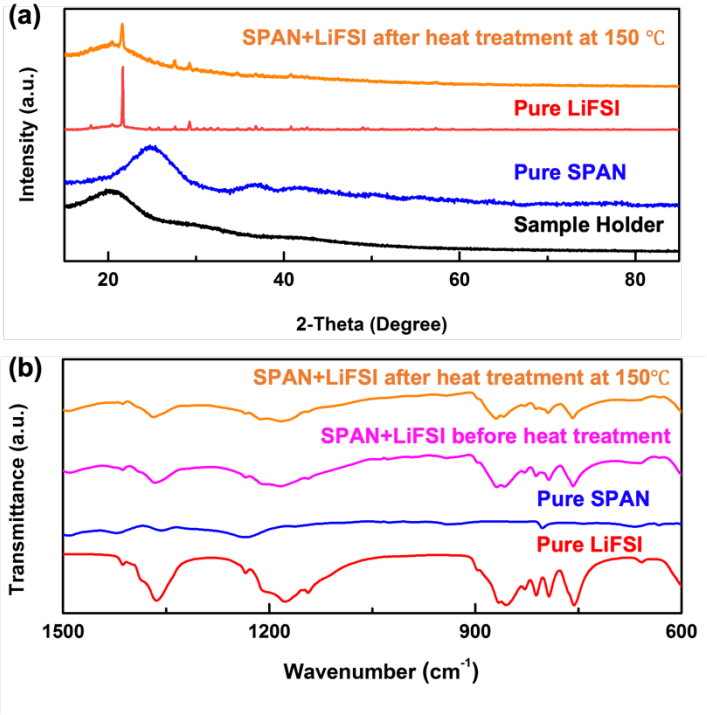


Figure 6.5. Characterizations of the all-solid-state garnet Li-S cell regarding the stability between SPAN and LiFSI and the morphology of cathode and cathode/LLZO interface. (a) and (b) are the XRD and ATR-FTIR pattern of the cathode materials in different conditions, respectively.

The morphology of the cathodes and the cathode/LLZO interface was characterized by scanning electron microscopy (SEM) and transmission electron

microscopy (TEM). Note that LiFSI salt was not chemically stable when exposed to the electron beam in the SEM (Video 2) and TEM (Video 3), so all morphological images were captured after the sample had stabilized.

SEM images of the morphology of the cathodes and the cathode/LLZO interface are shown in Figure 6.6. The two-phase cathode without LiFSI (Figure 6.6a and 6.6b) showed poor contact within the cathode and between the cathode and the bilayer-LLZO. This led to an extremely high area specific resistance (ASR) of more than 250,000 ohm-cm^2, measured at both 22 ℃ and 60 ℃ (Figure 6.7a). Note that 60℃ was chosen for high-temperature cell-testing because the ionic conductivity of LiFSI increased to approximately 10^{-4} S/cm, which should enable relatively fast Li^+ transport and good charge transfer kinetics(5, 151).

When three-phase cathode (SPAN+NGW^{TM}+LiFSI) was applied without heat treatment (Figure 6.6c and 6.6d), the cell showed a reduced impedance (24,500-ohm cm^2 at 22 ℃ and 4800 ohm-cm^2 at 60 ℃, Figure 6.7b) but still displayed a relatively poor interfacial contact. In contrast, the cell with the heat-treated three-phase cathode (Figure 6.6e and 6.6f) showed better inter-particle contact between the phases within the cathode and better interfacial contact between cathode and LLZO. EIS results yielded an ASR of 1400 ohm-cm^2 at 22 ℃ and 433 ohm-cm^2 at 60 ℃ (Figure 6.7c). This decrease in ASR is due to the enhanced particle-to-particle contact in the cathode and across the cathode-electrolyte interface of the Li-S cell. Assuming the pores in the three-phase cathode (after heat treatment) were all filled by LiFSI, the total thickness of the cathode layer was ~ 29 μm/cm^2. The actual cathode thickness cannot be captured by SEM due to the chemical instability of LiFSI under electron beam. The TEM image

of the three-phase cathode after heat treatment (Figure 6.8) also showed that the LiFSI formed a contiguous coating for the other phases.

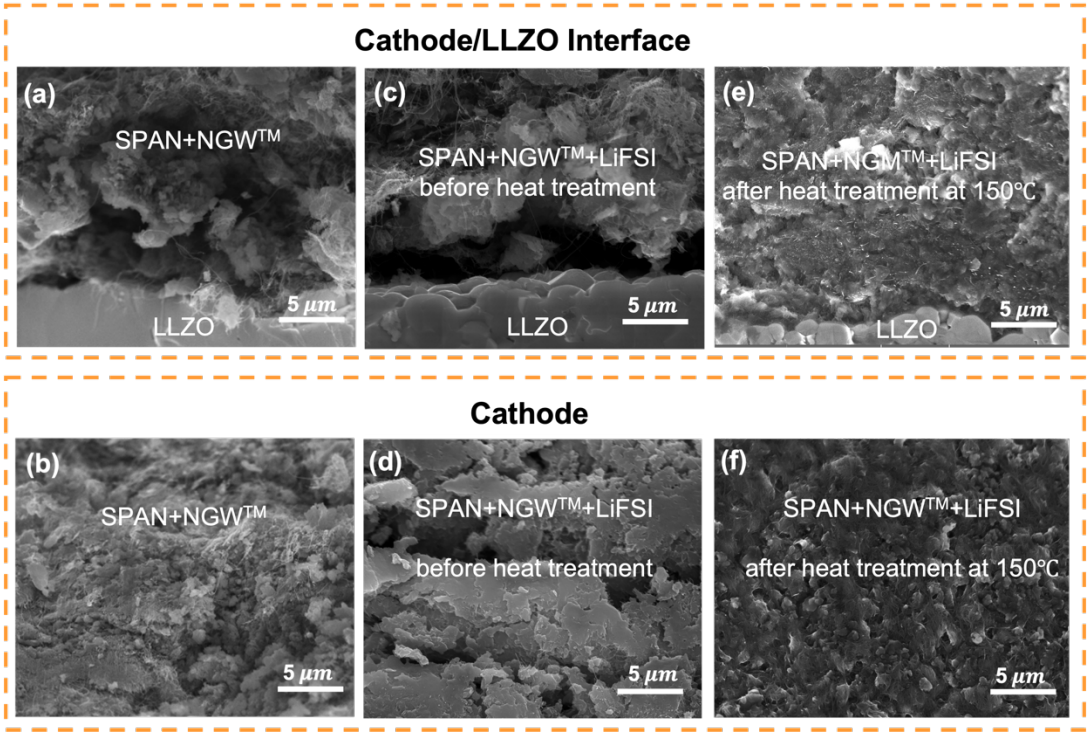


Figure 6.6. Morphology Characterizations of the all-solid-state garnet Li-S cell of the cathode and cathode/LLZO interface. Cross-section SEM images (a) of the interface between SPAN+NGW™ cathode and bilayer LLZO, and (b) of the cathode with a cell configuration of SPAN+NGW™/bilayer-LLZO/Li-metal. Cross-section SEM images (c) of the interface between SPAN+NGW™+LiFSI cathode and bilayer LLZO, and (d) of the SPAN+NGW™+LiFSI cathode. Note that the LiFSI in these SEM images was simply mixed with SPAN+NGW™ without heat treatment. Cross-section SEM images (e) of the interface between cathode and bilayer LLZO, and (f) of the cathode with a cell configuration of SPAN+NGW™+LiFSI (after heat treatment)/bilayer-LLZO/Li-metal.

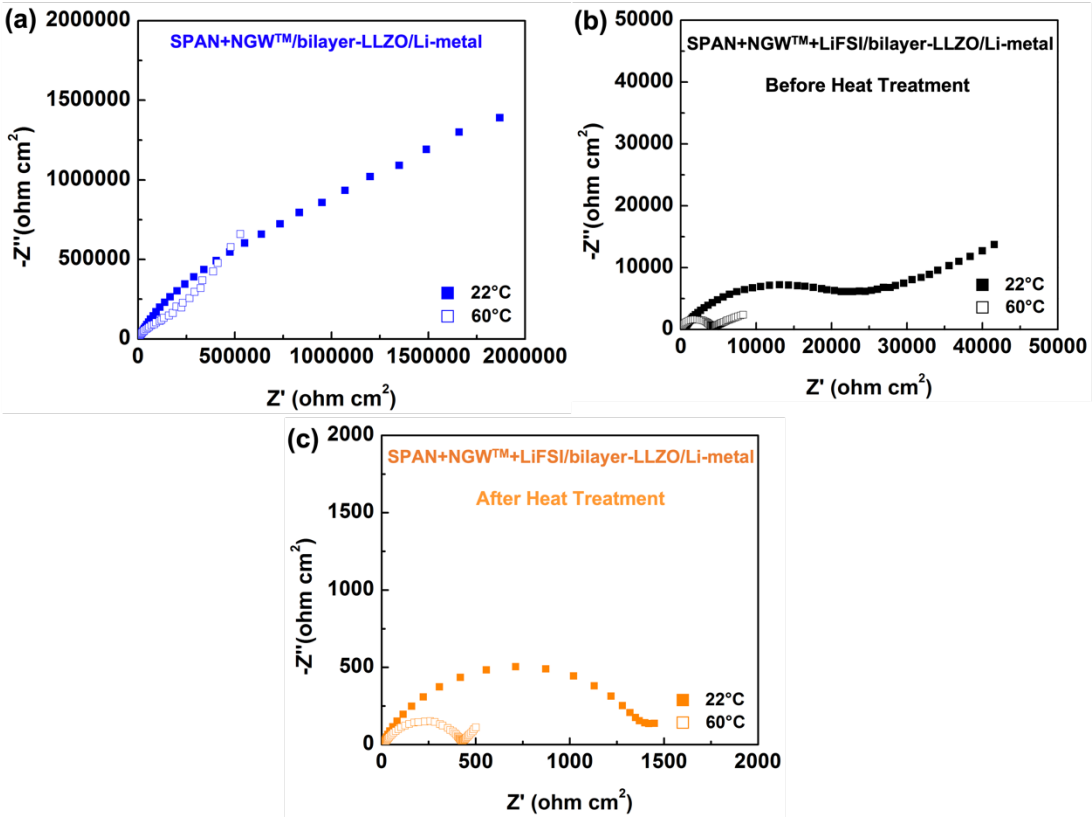


Figure 6.7. The Nyquist plot of a cell configuration of (a) SPAN+NGW^{TM}/bilayer-LLZO/Li-metal. The ASR at both 22°C and 60°C are more than 250,000-ohm cm^2. (b) SPAN+NGW^{TM}+LiFSI mixture (without melting LiFSI)/ bilayer-LLZO/Li-metal with an ASR of 24,500-ohm cm^2 at 22 °C and 4800-ohm cm^2 at 60 °C . (c) SPAN+NGW(TM)+LiFSI composite (after melting LiFSI)/bilayer-LLZO/Li-metal with an ASR of 1400 ohm cm^2 at 22°C and 433-ohm cm^2 at 60°C. The frequency ranges from 1MHz to 0.5 Hz and a voltage amplitude of 10 mV for all tests.

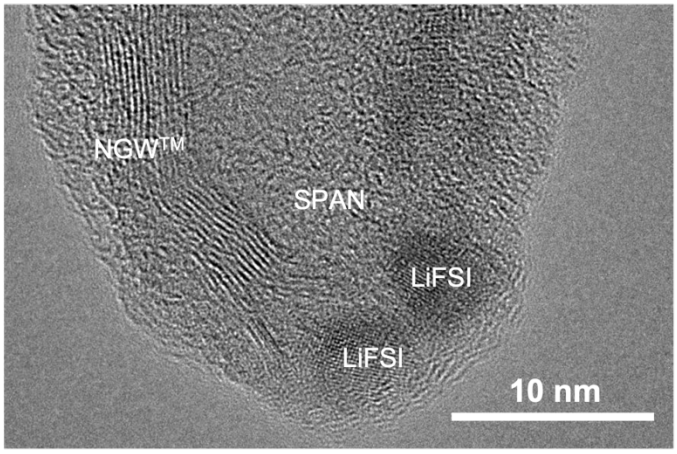


Figure 6.8. The TEM images of the three-phase cathode: SPAN+NGW™+LiFSI (after melting LiFSI).

6.3.3 *Cell Performance*

The electrochemical performance of all-solid-state garnet Li-S cells were characterized using 2032-type coin cells with a sulfur mass loading of 1 mg/cm^2. For the two-phase cathode without LiFSI, the poor interfacial contact observed in Figure 4a–4b resulted in low discharge capacities of less than 2 mAh/g at 22 ℃ and less than 20 mAh/g at 60 ℃ (cell#1, Figure 6.9a and 6.9b). When the LiFSI was simply mixed with the SPAN and NGW™ without heat treatment (Figure 6.6c and 6.6d), the cell still showed a low discharge capacity of less than 10 mAh/g at 22 ℃ and less than 120 mAh/g at 60 ℃ (cell# 2, Figure 6.9c and 6.9d). In both cases, the discharge capacities were not high enough for all-solid-state garnet Li-S batteries.

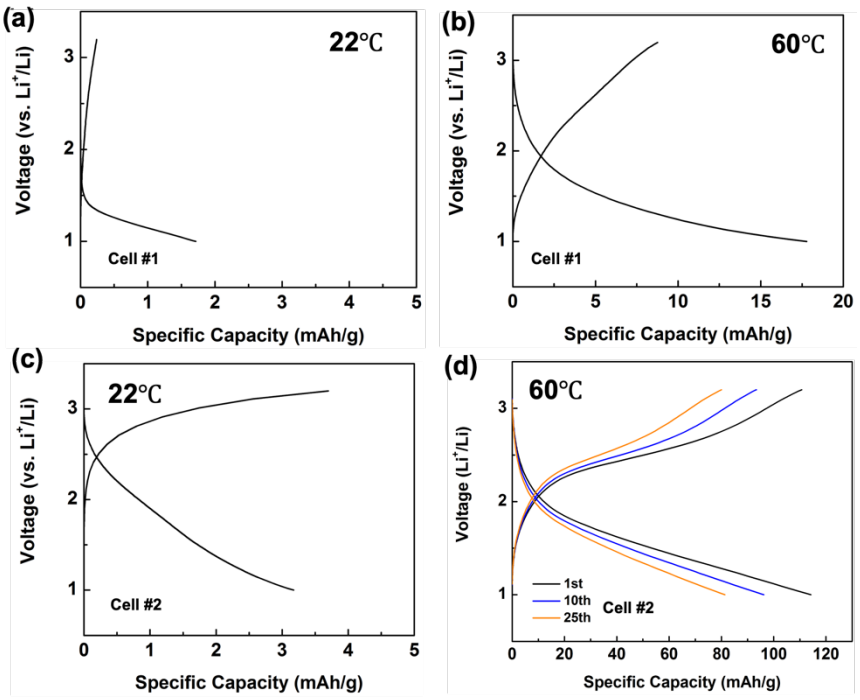


Figure 6.9. The electrochemical cycling of all-solid-state Li-S cell with a cell configuration of (a) and (b). SPAN+NGW^{TM}/bilayer LLZO/Li metal cells tested at 0.084 mA/cm^2 at 22°C and 60°C, respectively. (c) and (d). SPAN+NGW^{TM}+LiFSI (without melting LiFSI)/bilayer LLZO/Li metal cells tested at 0.084 mA/cm^2 at 22°C and 60°C, respectively.

In contrast, the all-solid-state Li-S cell using the heat-treated three-phase cathode showed a good initial discharge capacity of 1106 mAh/g at 22°C (Figure 6.10a, cell #3). When the cell stabilized after the 81st cycle the average discharge capacity was 396 mAh/g at 0.084 mA/cm^2 with a decay rate of ~0.4% per cycle. By comparison, an all-solid-state Li-S cell with carbon black (instead of NGW^{TM}) as carbon source in the cathode showed a faster capacity decay rate of ~0.7% per cycle when tested under the same conditions (Figure 6.11), demonstrating the benefits of the NGW^{TM}.

When the all-solid-state Li-S cell using the heat-treated three-phase cathode was tested under the same current density at 60 ℃ the initial discharge capacity increased to near theoretical 1594 mAh/g (cell #4) as shown in Figure 6.10b and 6.10c. For the C-rate performance evaluation the discharge current density was varied from 0.084 mA/cm^2 to 1.67 mA/cm^2 and back down to 0.084 mA/cm^2 with 5 cycles at each current density. The discharge capacity reduced to almost zero at 1.67 mA/cm^2 and recovered to 1364 mAh/g (the highest value in the last 5 cycles) when the discharge current density was returned to 0.084 mA/cm^2, indicating high-capacity recoverability during the C-rate testing. The average discharge capacity under each C-rate is given in Table 6.1.

The long-term cycling performance of the all-solid-state Li-S cell at 60 ℃ was then tested at 0.1C due to the high capacity achieved at a reasonably high current density (0.167 mA/cm^2). Under these test conditions, cell #5 showed an average discharge capacity of 1400 mAh/g over 40 cycles (Figure 6.10d and 6.10e). However, the cell showed a fast capacity decay after 40 cycles (Figure 6.12a). According to the postmortem SEM images of the cell (Figure 6.12b), the fast capacity decay was likely due to partial delamination within the three-phase cathode and at the cathode/electrolyte interface.

Long-term cycling performance was also evaluated at a higher discharge current density of 0.84 mA/cm^2 at 60 ℃ (cell #6) corresponding to a 0.5C discharge rate. Cell #6 displayed very stable cycling over 200 cycles and an average coulombic efficiency of ~99%, but at a lower average discharge capacity of 437 mAh/g due to the higher cycling rate indicating ionic/electronic conductivity limitations on sulfur

utilization (Figure 6.10f and Figure 6.13a). The postmortem SEM images of the cell (Figure 6.13b) revealed that there was little delamination within the three-phase cathode or at the cathode/electrolyte interface. This further indicated that the relatively fast capacity decay of cell #5 was likely due to the cathode delamination and adhesion issues. This is in good agreement with previous reports in literature that maintaining the integrity of the electrode microstructure is critical to achieving stable cell cycling(137).

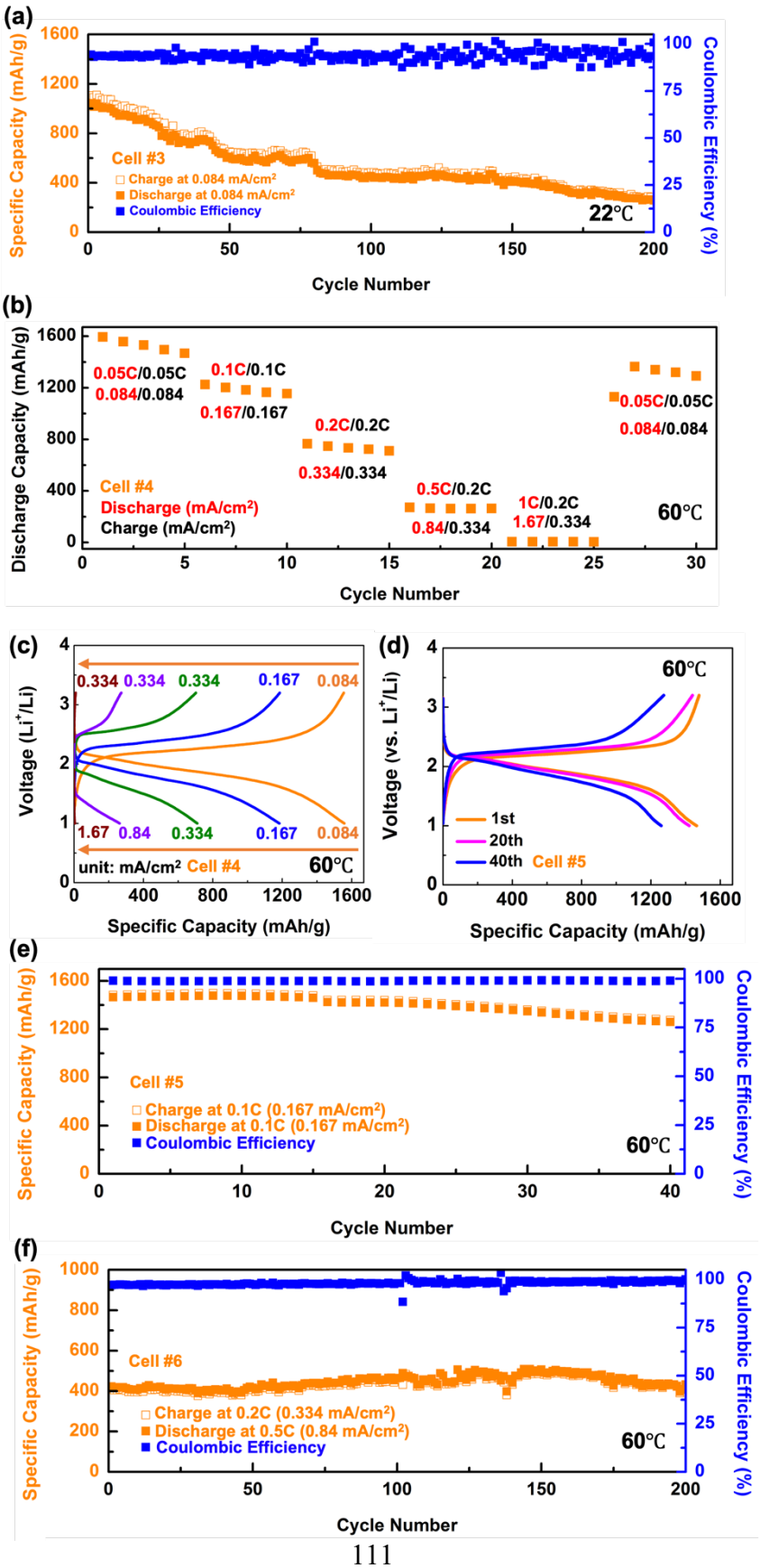

(a)
Specific Capacity (mAh/g)
Coulombic Efficiency (%)
Cycle Number
Cell #3
Charge at 0.084 mA/cm²
Discharge at 0.084 mA/cm²
Coulombic Efficiency
22℃
(b)
Discharge Capacity (mAh/g)
Cycle Number
0.05C/0.05C
0.084/0.084
0.1C/0.1C
0.167/0.167
0.2C/0.2C
0.334/0.334
0.5C/0.2C
0.84/0.334
1C/0.2C
1.67/0.334
0.05C/0.05C
0.084/0.084
Cell #4
Discharge (mA/cm²)
Charge (mA/cm²)
60℃
(c)
Voltage (Li⁺/Li)
Specific Capacity (mAh/g)
0.334 0.334 0.334 0.167 0.084
1.67 0.84 0.334 0.167 0.084
unit: mA/cm² Cell #4
60℃
(d)
Voltage (vs. Li⁺/Li)
Specific Capacity (mAh/g)
60℃
1st
20th
40th
Cell #5
(e)
Specific Capacity (mAh/g)
Coulombic Efficiency (%)
Cycle Number
Cell #5
Charge at 0.1C (0.167 mA/cm²)
Discharge at 0.1C (0.167 mA/cm²)
Coulombic Efficiency
60℃
(f)
Specific Capacity (mAh/g)
Coulombic Efficiency (%)
Cycle Number
Cell #6
Charge at 0.2C (0.334 mA/cm²)
Discharge at 0.5C (0.84 mA/cm²)
Coulombic Efficiency
60℃

Figure 6.10. Electrochemical performance of all-solid-state bilayer LLZO Li-S cells at 22 ℃ and 60 ℃. (a). The cycling performance tested at 0.084 mA/cm^2 at 22 ℃ over 200 cycles. (b). The rate performance at 60 ℃ under different current density of the all-solid-state garnet Li-S cell. 5 cycles were performed for each C-rate. (c) The voltage profile of the C-rate test. (d) and (e) The voltage profile and cycling performance of the all-solid-state Li-S cell tested at 60 ℃ at 0.167 mA/cm^2, respectively. (f). The cycling performance at 60 ℃ at a high current density of 0.84 mA/cm^2 (discharge)/0.334 mA/cm^2 (charge).

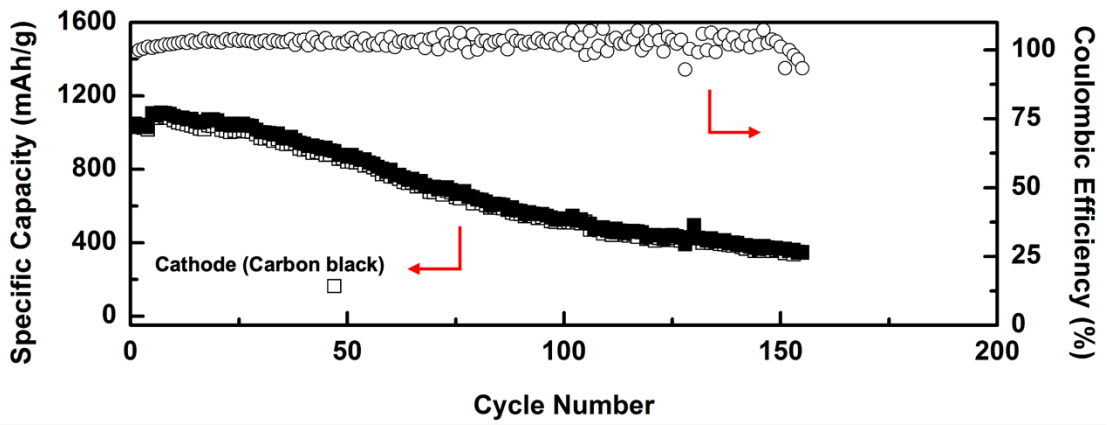


Figure 6.11. The all-solid-state garnet Li-S cell using carbon-black as carbon source and tested at a current density of 0.084 mA/cm^2 at 22 ℃.

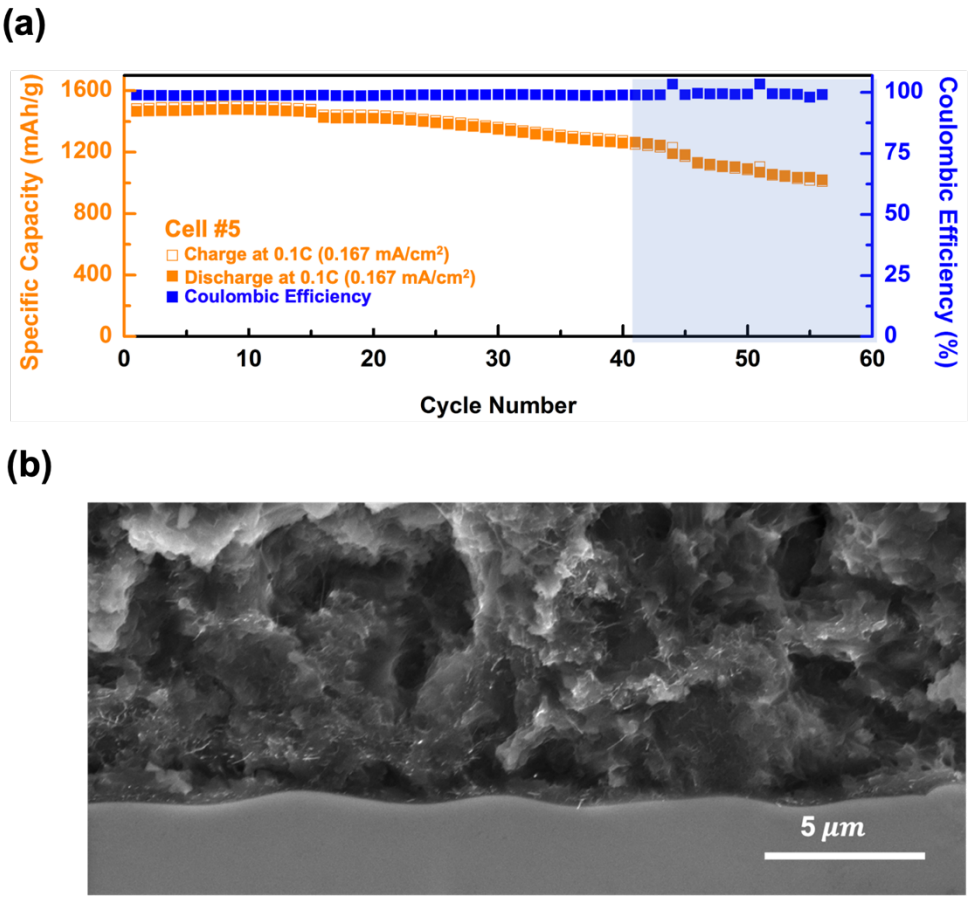


Figure 6.12. Electrochemical and morphological characterizations of the all-solid-state garnet Li-S batteries tested at 0.167 mA/cm^2 at 60℃ (a). Electrochemical performances of the all-solid-state garnet Li-S battery over the entire cycling. The cell was stopped at 57th cycle due to a relative fast capacity decay from 41st to 57th cycle (blue region) compared with the first 40 cycles. (b). The SEM image captured at the composite cathode (top) and LLZO (bottom) interface of the all-solid-state Li-S cell after cycling.

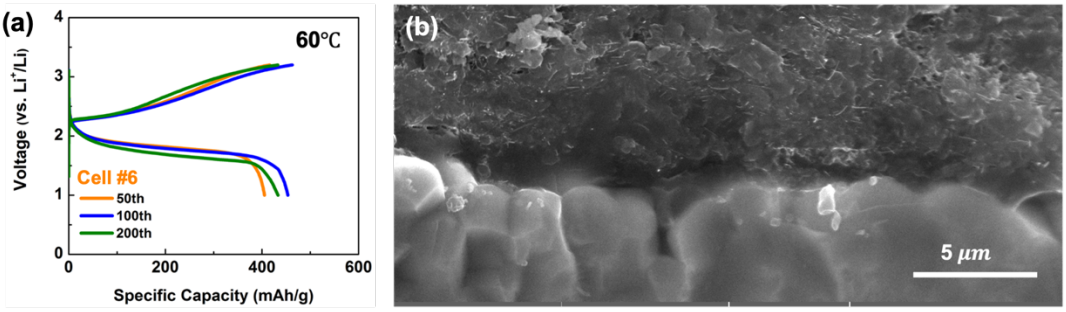


Figure 6.13. (a). The voltage profile of the all-solid-state garnet Li-S cell (cell #6) tested at 0.84 mA/cm^2 (discharge current density)/ 0.334 mA/cm^2 (charge current density) at 60℃ under a sulfur mass loading of 1mg/cm^2. (b). The SEM image captured at the composite cathode (top) and LLZO (bottom) interface of the all-solid-state Li-S cell after cycling of (a).

Overall, the all-solid-state garnet Li-S cells demonstrated excellent initial cycling performance at different current densities at 22℃ and 60℃ and reasonably stable cycling at 60°C (Table 6.1). We attribute the excellent cycling performance to (i) our thin bilayer LLZO architecture (Figure 6.14) enabled by scalable tape-casting technique that had 10 times lower ASR than thick LLZO pellets and enabled faster Li^+ ion transport kinetics through the LLZO(57, 98, 99, 152); (ii) LiFSI as a high ionic conductivity catholyte (1.9×10^{-5} S/cm at 22℃ and 1.2×10^{-4} S/cm at 60℃), which enabled good Li^+ ion transport kinetics throughout the three-phase cathode and at the cathode/LLZO interface; and (ii) good contact between within the three-phase cathode, and along the cathode/bilayer-LLZO interface.

Table 6.1. Cell Performance Summary

Cathode Type (Cell Number)	Temperature	Cycles	Current Density Charge/Discharge (mA/cm^2)	Average Discharge Capacity (mAh/g)
Two-phase (cell #1)	60°C 22°C	1 1	0.084/0.084 0.084/0.084	<20 <2
Three-phase (cell #2)*	60°C 22°C	25 1	0.084/0.084 0.084/0.084	<100 <4
Three-phase (cell #3)	60°C	5 cycles for each	0.084/0.084 0.167/0.167 0.334/0.334 0.84/0.334 1.67/0.334 0.084/0.084	1529 1186 736 407 ~5 1289
Three-phase (cell #4)	60°C	40	0.167/0.167	1400
Three-phase (cell #5)	60°C	200	0.334/0.84	437
Three-phase (cell #6)	22°C	150	0.084/0.084	445**

*The cathode in cell #2 was before heat treatment and the cathode in cell #3–#6 was after heat treatment.

** The value was calculated after the 81st cycle when the cell capacity got stabilized.

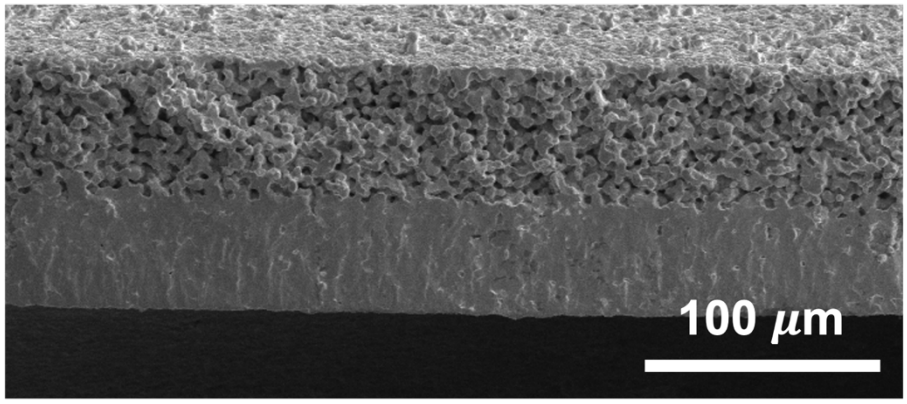


Figure 6.14. The SEM image of a representee bilayer LLZO with a dense layer thickness of 45 μm and a porous layer thickness of 55 μm.

6.3.4 *High-Energy-Density All-Solid-State Garnet Li-S Batteries*

Energy density is a critical factor for practical solid-state battery applications. To achieve high energy density, the three-phase sulfur cathode was incorporated into a newly invented 3D column LLZO architecture that had higher surface area and could further increase Li^+ kinetics between the cathode and electrolyte in all-solid-state Li-S

cell under high sulfur mass loading. Figure 6.15a shows the process of making the 3D column LLZO architecture using a direct ink writing method to apply a cubic LLZO ink to the dense side of a bilayer tape. The SEM images (Figure 6.15b) showed the column was printed and sintered very uniformly on the dense side of the bilayer LLZO. The whole 3D column architecture showed pure cubic LLZO phase in XRD analysis (Figure 6.15c), which enabled fast Li^+ transport throughout the entire architecture. This 3D-printing work was conducted by my colleague Griffin Godbey.

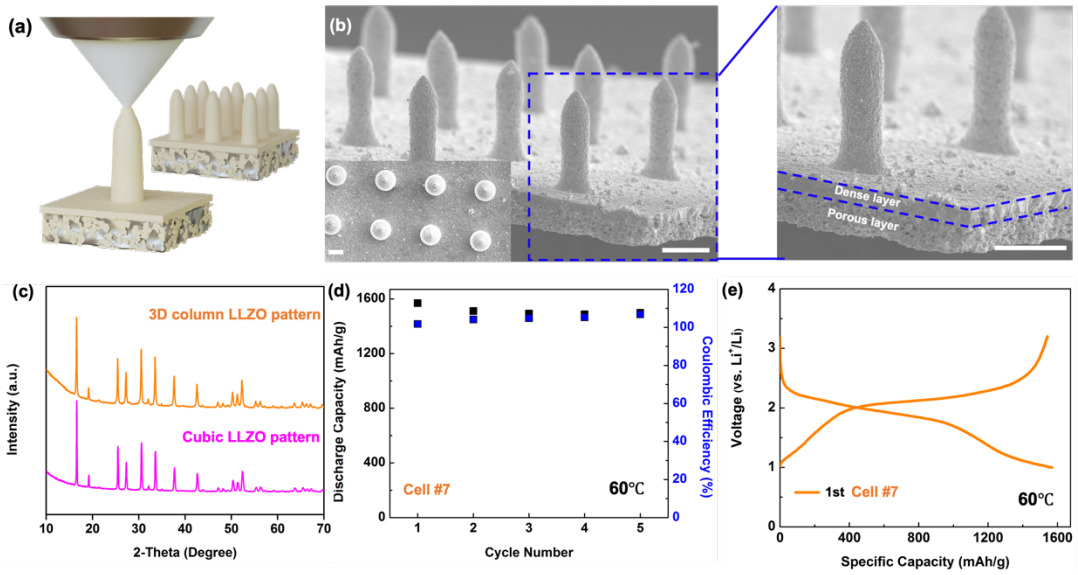


Figure 6.15. High-Energy-Density cell demonstration using 3D column LLZO architecture. (a) The schematics of 3D column LLZO enabled by direct ink writing. The column was printed directly onto the dense side of the bilayer LLZO. (b) The SEM (cross section and top view (insert)) images of the 3D column LLZO and the zoom-in SEM image of (b) to show the well-sintered bilayer LLZO architecture. The scale bars are 100 μm. (c) The XRD pattern of the 3D printed column LLZO architecture. (d) and (e) are the voltage profile and cycling performance respectively of the high-energy-density cell with a high sulfur mass loading of 7 mg/cm^2 tested at 60°C.

Electrochemical performances of the 3D column LLZO architecture were demonstrated using an extremely high sulfur loading of 7 mg/cm^2 at 60℃ using the all-solid-state Li-S battery design. The all-solid-state Li-S cell enabled by the 3D column architecture tested at 0.03C (C-rate was calculated based on the theoretical capacity of elemental sulfur.) illustrated an exceptionally high initial discharge capacity of 1569 mAh/g (cell #7), which was ~3.5 times higher than an all-solid-state garnet Li-S cell enabled by a bilayer LLZO architecture (444 mAh/g, cell #8 in Figure 6.16) tested using the same sulfur mass loading (7mg/cm^2) and same C-rate. Such high discharge capacity achieved by 3D column LLZO architecture corresponded to a high energy density of 338 Wh/kg and 797 Wh/L. The high-energy-density all-solid-state Li-S cell performance was summarized in Table 6.2. The energy density calculation details are presented in Table 6.3.

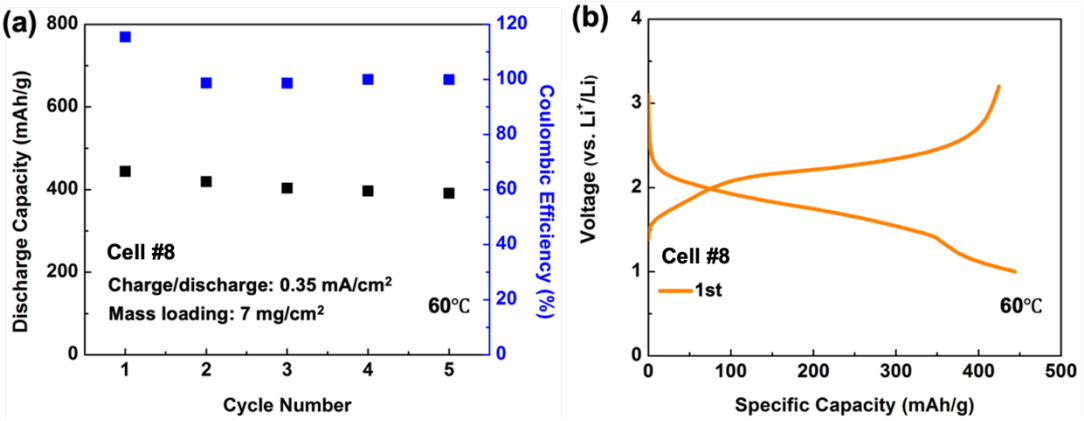


Figure 6.16. High sulfur loading (7 mg/cm^2) all-solid-state garnet Li-S cell enabled by the 3D LLZO bilayer architecture tested at 60℃ with current density of 0.35 mA/cm^2. (a) the cycling performance the all-solid-state garnet Li-S batteries (b). The voltage profile of the first cycle shown in (a).

Table 6.2. High-energy-density cell performance summary

Cell Type (Cell Number)	Current Density (mA/cm^2)	Discharge Capacity (mAh/g)	Energy Density Wh/kg/Wh/L
Three-phase cathode/3D Column Architecture (cell #7)	0.35	1569	338/797
Three-phase cathode/Bilayer Architecture (cell #8)	0.35	444	82/239

* The cell testing temperature in Table 6.2 is 60℃. The sulfur loading is 7 mg/cm^2.

For the energy density calculation, the following reasonable assumptions were applied when performing the energy density calculation:

(1). The amount of Li metal was assumed to capacity match the sulfur

$$m(Li) = \frac{m(sulfur) \times c(sulfur)}{c(Li)}$$

where $m(Li)$ and $m(sulfur)$ are the areal mass of Li and sulfur (7 mg/cm^2), respectively. $c(Li)$ and $c(sulfur)$ are the capacity of Li (3861 mAh/g) and the demonstrated capacity of sulfur (1545 mAh/g).

$$m(Li) = \frac{m(sulfur) \times c(sulfur)}{c(Li)} = \frac{7\ mg/cm^2 \times 1670\ mAh/g}{3860\ mAh/g} = 2.55\ mg/cm^2$$

(2). The porosity of the porous layer of the bilayer LLZO was 60%.

(3). The average discharge voltage was 1.8V.

(4). The volume of the SPAN was equal to the volume of the PAN sulfur host.

Table 6.3. The demonstrated energy density of the all-solid-state garnet Li-S battery using 3D column structure

Material	**Mass mg/cm^2**	Density g/cm^3	**Volume (µL/cm^2)**	Specific Capacity (mAh/g)	Charge (mAh)
Sulfur	**7**	2.07		1569	10.98
PAN	**8.22**	1.18	**6.96**		
NGW™	**3.69**	2.27	**1.62**		
LIFSI	**15.33**	2.32	**6.61**		
LLZO	**21.50**	5.00	**4.30**		
Li-metal	**2.84**	0.53	**5.33**	3861	10.98
Total	**58.57**		**24.23**		
	Average discharge voltage = 1.8V			Energy Density (Wh/kg)	338
				Energy Density (Wh/L)	797

Given the remarkably high energy density (338 Wh/kg and 797 Wh/L) achieved through the all-solid-state garnet Li-S cells enabled by our inorganic interfacial engineering method and 3D printed column LLZO architecture, our performance is very promising in the field of garnet Li-S batteries (Figure 6.17). The detailed information of the energy density comparison is also summarized in Table 6.4 with references cited. When the dense layer thickness of the 3D column architecture reduced to 10 μm, a high projected energy densities of 387 Wh/kg and 848 Wh/L can be achievable.

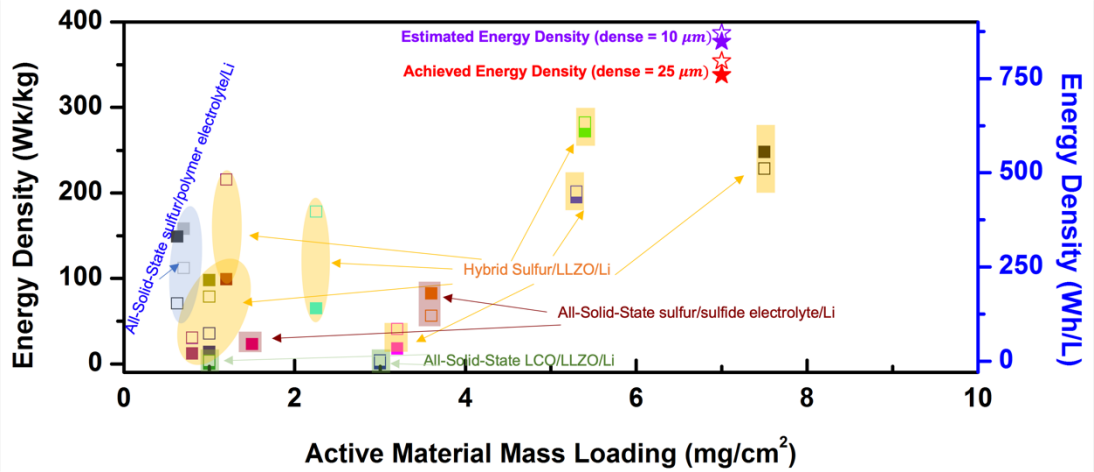


Figure 6.17. Energy Density Comparison of the all-solid-state garnet Li-S batteries with the state-of-art garnet-based Li-S batteries. Note that the solid square/star and open square/star is for gravimetric energy density and volumetric energy density, respectively. The references were cited in Table 6.4.

Table 6.4. Energy density comparison of our work with the state-of-art published results

Cell Configuration	Active material mass loading (mg/cm^2)	Energy Density		Ref.
		Wh/kg	Wh/L	
Sulfur cathode/liquid electrolyte/bilayer LLZO/Li (hybrid cell)	7.5	248	511	(58)
Sulfur cathode/liquid electrolyte/trilayer LLZO/Li (hybrid cell)	5.4	272	633	(69)
SPAN cathode/ionic liquid/trilayer LLZO/Li (hybrid cell)	5.3	195	450	(57)
Sulfur cathode/liquid electrolyte/LLZO pellet/Li (hybrid cell)	2.25	65	397	(96)
Sulfur cathode/liquid electrolyte/LLZO pellet/Li (hybrid cell)	3.2	18	85	(101)
Sulfur cathode/liquid electrolyte/LLZO pellet/Li (hybrid cell)	0.8	12	61	(97)
Sulfur cathode/liquid electrolyte/LLZO pellet/Li (hybrid cell)	1	98	171	(153)

Sulfur cathode/liquid electrolyte/LLZO pellet/Li (hybrid cell)	1	14	73	(100)
Sulfur cathode/liquid electrolyte/LLZO pellet/Li (hybrid cell)	0.8	12	62	(98)
Sulfur cathode/liquid electrolyte/LLZO pellet/Li (hybrid cell)	1.2	99	482	(66)
$LiCoO_2$/LCBO/LLZO pellet/Li (all-solid-state cell)	1	0.08	0.4	(5)
LCO/LCBO/LLZO pellet/Li (all-solid-state cell)	3	0.3	1.2	(5)
Li_2S/sulfide electrolyte/Li (all-solid-state cell)	3.6	82.5	120.5	(154)
Li_2S+$LiTiS_2$/sulfide electrolyte/Li (all-solid-state cell)	1.5	23	38	(155)
Sulfur cathode/PEO-based electrolyte/Li (all-solid-state cell)	0.7	158	247	(156)
Sulfur cathode/PEO-based electrolyte/Li (all-solid-state cell)	0.625	149	153	(90)
SPAN+NGW^{TM}+LiFSI/bilayer LLZO/Li	7	338	797	This work

6.4 Conclusions

In summary, we demonstrated that LiFSI can be used as a solid-state catholyte with an ionic conductivity of 1.9×10^{-5} S/cm at 22 ℃ and 1.2×10^{-4} S/cm at 60 ℃, and that it is stable with the SPAN CAM and is electrochemically stable between 1 V and 3.5 V (vs. Li^+/Li). Moreover, we developed a novel three-phase (SPAN+NGW^{TM}+LiFSI) sulfur cathode for all-solid-state garnet Li-S cells. Replacing traditional carbon black with NGW^{TM} resulted in a more mechanically robust composite cathode while maintaining a continuous electronic conductive network. Melt infiltration of the LiFSI into the composite cathode greatly improved inter-particle contact within the cathode and cathode/electrolyte interfacial contact. All-solid-state Li-S cells using the heat-treated three-phase cathode demonstrated stable cycling

performance at 60 ℃ with a high average discharge capacity of 1400 mAh/g at 0.167 mA/cm^2 for over 40 cycles and 437 mAh/g at 0.84 mA/cm^2 for over 200 cycles. Furthermore, enabled by an innovative 3D column LLZO structure using 3D printing method, the all-solid-state cathode design also demonstrated a high energy density of 309 Wh/kg and 766 Wh/L at a cell level.

Chapter 7: Conclusions and Future Work

7.1 Conclusions

Overall, through the work in this dissertation, the energy densities of solid-state Li-S batteries using garnet electrolyte have been greatly improved. Through Chapter 4, I have found that La segregation of garnet electrolyte to the surface on the cathode side led to the charge fluctuation issue which causes battery failure. To address this issue, a PEO-based interlayer was applied between sulfur cathode and Ta-LLZO. With the help of this protective interlayer, a high initial discharge capacity of 1307 mAh/g was achieved with a sulfur mass loading of 4 mg/cm^2 at RT, corresponding to energy densities of 134 Wh/kg and 639 Wh/L. When the dense layer of the bilayer LLZO reduced to 10 μm which is only an engineering-level adjustment, high energy densities of 257 Wh/kg and 1308 Wh/L is achievable.

However, this solution required a relatively large amount of catholyte (20 μL/cm^2), reducing cell energy density. In Chapter 5, I innovated an in-situ formed GPE to stabilize the sulfur cathode and Ta-LLZO interface. Through XPS, it was shown that if the salt decomposition is preferred over solvent decomposition (2M/3M GPE), the sulfur cathode/Ta-LLZO interface can be better stabilized, compared with the case where solvent decomposition preferred over salt decomposition (1M GPE). Through this designed 2M GPE, high sulfur loading (5.2 mg/cm^2) and high capacity retention garnet Li-S cells were obtained. Specifically, the cell demonstrated high initial capacity of 1542 mAh/g with an average capacity of 1379 mAh/g over 60 cycles discharged at 0.87 mA/cm^2 at 22℃. This high initial discharge capacity corresponds to an energy

density of 223 Wh/kg (769 Wh/L). With the same cell configuration, another fresh 2M GPE cell can deliver an average discharge capacity of 1218 mAh/g over 265 cycles with 80% capacity retention under a discharge current density of 1.74 mA/cm^2

Finally, since the catholytes used in Chapter 4 and Chapter 5 are flammable, compromising on the safety of solid-state batteries. Therefore, it is critical to develop all-solid-state garnet Li-S batteries and that is what Chapter 6 focuses on. In Chapter 6, we report an all-solid-state garnet Li-S cell in which a solid-state sulfur cathode is fabricated by mixing SPAN with molten LiFSI and NGW^{TM} to improve interfacial contact and ionic and electronic conduction throughout the solid cathode structure. This solid SPAN+LiFSI+NGW cathode was deposited on a dense/porous bilayer garnet structure impregnated on the porous anode side with Li metal. LiFSI has an ionic conductivity of 1.9×10^{-5} S/cm at 22 ℃ and 1.2×10^{-4} S/cm at 60 ℃ and is electrochemically stable in the Li-S battery operational voltage window (1V–3.5V) as a solid-state catholyte. Moreover, of particular importance to use with a sulfur cathode the low melting temperature (145 ℃) of LiFSI allows it to spread through the cathode matrix in the thermal stability range of SPAN (<200℃)(22, 146, 147). The all-solid-state cells obtained an average discharge capacity of 1400 mAh/g at a current density of 0.167 mA/cm^2 (0.1C) for over 40 cycles and 437 mAh/g at 0.84 mA/cm^2 (0.5C) for over 200 cycles for our Li-S cell at 60°C. By applying an innovative 3D column LLZO structure enabled by 3D printing method, an exceptionally high energy density of 338 Wh/kg and 797 Wh/L was demonstrated at 60℃ under a high sulfur loading of 7 mg/cm^2 with the same all-solid-state cathode design.

7.2 Future Work

Through Chapter 5, it was demonstrated that the salt decomposition preferred over the solvent decomposition in the catholyte can fully stabilize the sulfur cathode/Ta-LLZO interface. Therefore, it is worth to use high concentrated liquid electrolyte (i.e. salt-in-solvent electrolyte) and/or localized high concentrated liquid electrolyte which shows less flammability, to be an alternative as GPE to achieve good cycling performances with high energy densities.

Chapter 8: Publications

C.M. Shi, G. Alexander, J. O'Neill, G. Godbey, K. Duncan, E. Wachsman*, All-Solid-State Garnet type Lithium-Sulfur Battery Enabled by Inorganic Lithium Conductive Salt and Bilayer Electrolyte Architecture, submitted.

C.M. Shi, S. Takeuchi, G. Alexander, T. Hamman, J. O'Neill, J.A. Dura, E. Wachsman*, High Sulfur Loading and Capacity Retention in Bilayer Garnet Lithium-Sulfur Batteries with Gel Polymer Electrolytes, submitted.

C.M. Shi§, T. Hamman§, S. Takeuchi, G. Alexander, A. Nolan, M. Limpert, Z.Z. Fu, J. O'Neill, G. Godbey, E. Wachsman*, 3D Asymmetric Bilayer Garnet Hybridized High-Energy-Density Lithium-Sulfur Batteries, accepted by *ACS Applied Materials & Interface*.

C.M. Shi, R. Hoft, Y.Y. Ren, E. Wachsman*, Cathode and Electrolyte Interface Towards Garnet-type Solid-State Lithium-Sulfur Battery, draft finished.

§: contributed equally to the manuscript; * corresponding author

Bibliography

1. B. Liu, *et al.*, Garnet Solid Electrolyte Protected Li-Metal Batteries. *ACS Appl. Mater. Interfaces* **9**, 18809–18815 (2017).
2. J. Hou, *et al.*, Thermal runaway of Lithium-ion batteries employing LiN(SO2F)2-based concentrated electrolytes. *Nat. Commun.* **11**, 1–11 (2020).
3. J. Huang, A. F. Hollenkamp, Thermal behavior of ionic liquids containing the FSI anion and the Li + cation. *J. Phys. Chem. C* **114**, 21840–21847 (2010).
4. M. Kerner, N. Plylahan, J. Scheers, P. Johansson, Thermal stability and decomposition of lithium bis(fluorosulfonyl)imide (LiFSI) salts. *RSC Adv.* **6**, 23327–23334 (2016).
5. F. Han, *et al.*, Interphase Engineering Enabled All-Ceramic Lithium Battery. *Joule* **2**, 497–508 (2018).
6. L. Zhou, Q. Zhang, L. F. Nazar, Li-Rich and Halide-Deficient Argyrodite Fast Ion Conductors. *Chem. Mater.* (2022) https:/doi.org/10.1021/acs.chemmater.2c02343.
7. H. D., U. J., Electric dry cells and storage batteries - US Patent 3043896. 3043896 (1962).
8. R. M. L. Bhaskara, Organic electrolyte cells. *US Pat. 3413154*, Nov 26 (1968).
9. P. E., G. A., S. M., S. Y., Rechargable Lithium-Sulfur Battery (Extended Abstract). *J. Power Sources* **26**, 269–271 (1989).
10. P. G. Bruce, S. A. Freunberger, L. J. Hardwick, J. M. Tarascon, Li-O2 and Li-S batteries with high energy storage. *Nat. Mater.* **11**, 19–29 (2012).

11. H. J. Peng, J. Q. Huang, Q. Zhang, A review of flexible lithium-sulfur and analogous alkali metal-chalcogen rechargeable batteries. *Chem. Soc. Rev.* **46**, 5237–5288 (2017).

12. S. Wei, L. Ma, K. E. Hendrickson, Z. Tu, L. A. Archer, Metal-Sulfur Battery Cathodes Based on PAN-Sulfur Composites. *J. Am. Chem. Soc.* **137**, 12143–12152 (2015).

13. S. Xin, *et al.*, Smaller sulfur molecules promise better lithium'sulfur batteries. *J. Am. Chem. Soc.* **134**, 18510–18513 (2012).

14. M. Rana, *et al.*, Recent advances in separators to mitigate technical challenges associated with re-chargeable lithium sulfur batteries. *J. Mater. Chem. A* **7**, 6596–6615 (2019).

15. W. P. Wang, *et al.*, Solidifying Cathode–Electrolyte Interface for Lithium–Sulfur Batteries. *Adv. Energy Mater.* **11** (2021).

16. A. Manthiram, Y. Fu, S. Chung, C. Zu, Y. Su, Rechargeable Lithium − Sulfur Batteries. *Chem. Rev.* (2014).

17. J. Zheng, *et al.*, High-Fluorinated Electrolytes for Li–S Batteries. *Adv. Energy Mater.* **9**, 1–9 (2019).

18. J. Zheng, *et al.*, Manipulating electrolyte and solid electrolyte interphase to enable safe and efficient Li-S batteries. *Nano Energy* **50**, 431–440 (2018).

19. M. Zhao, *et al.*, Lithium–Sulfur Batteries under Lean Electrolyte Conditions: Challenges and Opportunities. *Angew. Chemie - Int. Ed.* **59**, 12636–12652 (2020).

20. Y. Yang, *et al.*, High-capacity micrometer-sized Li 2S particles as cathode materials for advanced rechargeable lithium-ion batteries. *J. Am. Chem. Soc.* **134**, 15387–15394 (2012).

21. M. Ma, A. N. Mansour, J. K. Ko, G. H. Waller, C. E. Hendricks, Characterization of Li Diffusion and Solid Electrolyte Interface for Li 4 Ti 5 O 12 Electrode Cycled with an Organosilicon Additive Electrolyte . *J. Electrochem. Soc.* **167**, 110549 (2020).

22. S. S. Zhang, Understanding of sulfurized polyacrylonitrile for superior performance lithium/sulfur battery. *Energies* **7**, 4588–4600 (2014).

23. R. Mukkabla, M. R. Buchmeiser, Cathode materials for lithium-sulfur batteries based on sulfur covalently bound to a polymeric backbone. *J. Mater. Chem. A* **8**, 5379–5394 (2020).

24. W. Huang, *et al.*, Mechanically-robust structural lithium-sulfur battery with high energy density. *Energy Storage Mater.* **33**, 416–422 (2020).

25. D. Aurbach, E. Zinigrad, Y. Cohen, H. Teller, A short review of failure mechanisms of lithium metal and lithiated graphite anodes in liquid electrolyte solutions Doron. *Solid State Ionics* **148**, 405–416 (2002).

26. Q. Zhao, *et al.*, Designing electrolytes with polymerlike glass-forming properties and fast ion transport at low temperatures. *Proc. Natl. Acad. Sci. U. S. A.* **117**, 26053–26060 (2020).

27. Q. Pang, *et al.*, Tuning the electrolyte network structure to invoke quasi-solid state sulfur conversion and suppress lithium dendrite formation in Li–S batteries. *Nat. Energy* **3**, 783–791 (2018).

28. R. H. Basappa, T. Ito, H. Yamada, Contact between Garnet-Type Solid Electrolyte and Lithium Metal Anode: Influence on Charge Transfer Resistance and Short Circuit Prevention. *J. Electrochem. Soc.* **164**, A666–A671 (2017).

29. H. K. Tian, Z. Liu, Y. Ji, L. Q. Chen, Y. Qi, Interfacial Electronic Properties Dictate Li Dendrite Growth in Solid Electrolytes. *Chem. Mater.* **31**, 7351–7359 (2019).

30. F. Yonemoto, *et al.*, Temperature effects on cycling stability of Li plating/stripping on Ta-doped Li7La3Zr2O12. *J. Power Sources* **343**, 207–215 (2017).

31. F. Han, *et al.*, High electronic conductivity as the origin of lithium dendrite formation within solid electrolytes. *Nat. Energy* **4**, 187–196 (2019).

32. S. S. Zhang, Role of LiNO 3 in rechargeable lithium/sulfur battery. *Electrochim. Acta* **70**, 344–348 (2012).

33. S. S. Zhang, Liquid electrolyte lithium/sulfur battery: Fundamental chemistry, problems, and solutions. *J. Power Sources* **231**, 153–162 (2013).

34. A. N. Mistry, P. P. Mukherjee, “Shuttle” in Polysulfide Shuttle: Friend or Foe? *J. Phys. Chem. C* **122**, 23845–23851 (2018).

35. A. Bhargav, J. He, A. Gupta, A. Manthiram, Lithium-Sulfur Batteries: Attaining the Critical Metrics. *Joule* **4**, 285–291 (2020).

36. A. Rosenman, *et al.*, Review on Li-Sulfur Battery Systems: An Integral Perspective. *Adv. Energy Mater.* **5** (2015).

37. H. Wang, *et al.*, Graphene-wrapped sulfur particles as a rechargeable lithium-sulfur battery cathode material with high capacity and cycling stability. *Nano Lett.* **11**, 2644–2647 (2011).

38. Q. Cheng, *et al.*, Full Dissolution of the Whole Lithium Sulfide Family (Li2S <inf>8</inf> to Li <inf>2</inf> S) in a Safe Eutectic Solvent for Rechargeable Lithium–Sulfur Batteries. *Angew. Chemie - Int. Ed.* **58** (2019).

39. X. Ji, L. F. Nazar, Advances in Li-S batteries. *J. Mater. Chem.* **20**, 9821–9826 (2010).

40. X. Fan, *et al.*, All-temperature batteries enabled by fluorinated electrolytes with non-polar solvents. *Nat. Energy* **4**, 882–890 (2019).

41. X. Fan, *et al.*, Non-flammable electrolyte enables li-metal batteries with aggressive cathode chemistries. *Nat. Nanotechnol.* **13**, 715–722 (2018).

42. D. Zhou, D. Shanmukaraj, A. Tkacheva, M. Armand, G. Wang, Polymer Electrolytes for Lithium-Based Batteries: Advances and Prospects. *Chem* **5**, 2326–2352 (2019).

43. S. Wenzel, *et al.*, Direct Observation of the Interfacial Instability of the Fast Ionic Conductor Li10GeP2S12 at the Lithium Metal Anode. *Chem. Mater.* **28**, 2400–2407 (2016).

44. N. Kamaya, *et al.*, A lithium superionic conductor. *Nat. Mater.* **10**, 682–686 (2011).

45. W. G. Suci, H. Kasuma, K. Aliwarga, Y. R. Azinuddin, Review of various sul fi de electrolyte types for solid - state lithium - ion batteries. 409–423 (2022).

46. A. Sakuda, A. Hayashi, M. Tatsumisago, Sulfide solid electrolyte with favorable mechanical property for all-solid-state lithium battery. *Sci. Rep.* **3**, 2–6 (2013).

47. J. Yue, M. Yan, Y. X. Yin, Y. G. Guo, Progress of the Interface Design in All-Solid-State Li–S Batteries. *Adv. Funct. Mater.* **28**, 1–16 (2018).

48. J. Lau, *et al.*, Sulfide Solid Electrolytes for Lithium Battery Applications. *Adv. Energy Mater.* **8**, 1–24 (2018).

49. M. Hou, F. Liang, K. Chen, Y. Dai, D. Xue, Challenges and perspectives of NASICON-type solid electrolytes for all-solid-state lithium batteries. *Nanotechnology* **31** (2020).

50. Q. Cheng, *et al.*, Stabilizing Solid Electrolyte-Anode Interface in Li-Metal Batteries by Boron Nitride-Based Nanocomposite Coating. *Joule* **3**, 1510–1522 (2019).

51. N. J. Dudney, Solid-state thin-film rechargeable batteries. *Mater. Sci. Eng. B Solid-State Mater. Adv. Technol.* **116**, 245–249 (2005).

52. M. Huijben, G. Christiani, G. F. Harrington, C. W. Schneider, N . Pryds and V . Esposito (eds .) Metal Oxide-based Thin Film Structures : Formation , Characterization and Application of Interface-based Phenomena. 13–14 (2017).

53. Y. Zhu, X. He, Y. Mo, Origin of Outstanding Stability in the Lithium Solid Electrolyte Materials: Insights from Thermodynamic Analyses Based on First-Principles Calculations. *ACS Appl. Mater. Interfaces* **7**, 23685–23693 (2015).

54. V. Thangadurai, S. Narayanan, D. Pinzaru, Garnet-type solid-state fast Li ion conductors for Li batteries: Critical review. *Chem. Soc. Rev.* **43**, 4714–4727 (2014).

55. C. Wang, *et al.*, Garnet-Type Solid-State Electrolytes: Materials, Interfaces, and Batteries. *Chem. Rev.* (2020) https:/doi.org/10.1021/acs.chemrev.9b00427.

56. K. Kerman, A. Luntz, V. Viswanathan, Y.-M. Chiang, Z. Chen, Review—Practical Challenges Hindering the Development of Solid State Li Ion Batteries. *J. Electrochem. Soc.* **164**, A1731–A1744 (2017).

57. G. T. Hitz, *et al.*, High-rate lithium cycling in a scalable trilayer Li-garnet-electrolyte architecture. *Mater. Today* **22**, 50–57 (2019).

58. K. Fu, *et al.*, Three-dimensional bilayer garnet solid electrolyte based high energy density lithium metal-sulfur batteries. *Energy Environ. Sci.* **10**, 1568–1575 (2017).

59. B. Liu, *et al.*, 3D lithium metal anodes hosted in asymmetric garnet frameworks toward high energy density batteries. *Energy Storage Mater.* **14**, 376–382 (2018).

60. H. Xie, *et al.*, Amorphous-Carbon-Coated 3D Solid Electrolyte for an Electro-Chemomechanically Stable Lithium Metal Anode in Solid-State Batteries. *Nano Lett.* **21**, 6163–6170 (2021).

61. K. K. Fu, *et al.*, Transient Behavior of the Metal Interface in Lithium Metal–Garnet Batteries. *Angew. Chemie - Int. Ed.* **56**, 14942–14947 (2017).

62. W. Luo, *et al.*, Transition from Superlithiophobicity to Superlithiophilicity of Garnet Solid-State Electrolyte. *J. Am. Chem. Soc.* **138**, 12258–12262 (2016).

63. K. K. Fu, *et al.*, Toward garnet electrolyte–based Li metal batteries: An ultrathin, highly effective, artificial solid-state electrolyte/metallic Li interface. *Sci. Adv.* **3**, 1–12 (2017).

64. X. Han, *et al.*, Negating interfacial impedance in garnet-based solid-state Li metal batteries. *Nat. Mater.* **16**, 572–579 (2017).

65. W. L. Bragg, The relfection of X-ray by Crystal. *Proc. Camb. Philol. Soc.* **17**, 43 (1913).

66. K. Fu, *et al.*, Stabilizing the garnet solid-electrolyte/polysulfide interface in Li-S batteries. *Chem. Mater.* **29**, 8037–8041 (2017).

67. S. H. Chung, A. Manthiram, Current Status and Future Prospects of Metal–Sulfur Batteries. *Adv. Mater.* **31** (2019).

68. M. Shaibani, *et al.*, Expansion-tolerant architectures for stable cycling of ultrahigh-loading sulfur cathodes in lithium-sulfur batteries. *Sci. Adv.* **6** (2020).

69. S. Xu, *et al.*, All-in-one lithium-sulfur battery enabled by a porous-dense-porous garnet architecture. *Energy Storage Mater.* **15**, 458–464 (2018).

70. S. Xu, *et al.*, All-in-one lithium-sulfur battery enabled by a porous-dense-porous garnet architecture. *Energy Storage Mater.* **15**, 458–464 (2018).

71. E. Hanc, W. Zając, J. Molenda, Synthesis procedure and effect of Nd, Ca and Nb doping on structure and electrical conductivity of Li7La3Zr2O 12 garnets. *Solid State Ionics* **262**, 617–621 (2014).

72. S. Kim, *et al.*, High-energy and durable lithium metal batteries using garnet-type solid electrolytes with tailored lithium-metal compatibility. *Nat. Commun.* **13** (2022).

73. Y. Kim, *et al.*, Electrochemical stability of Li 6.5 La 3 Zr 1.5 M 0.5 O 12 (M = Nb or Ta) against metallic lithium. *Front. Energy Res.* **4**, 1–7 (2016).

74. Y. Zhu, *et al.*, Dopant-Dependent Stability of Garnet Solid Electrolyte Interfaces with Lithium Metal. *Adv. Energy Mater.* **9**, 1–11 (2019).

75. D. W. McOwen, *et al.*, 3D-Printing Electrolytes for Solid-State Batteries. *Adv. Mater.* **30**, 1–7 (2018).

76. M. Zhao, B. Q. Li, X. Q. Zhang, J. Q. Huang, Q. Zhang, A Perspective toward Practical Lithium-Sulfur Batteries. *ACS Cent. Sci.* **6**, 1095–1104 (2020).

77. A. Manthiram, X. Yu, S. Wang, Lithium battery chemistries enabled by solid-state electrolytes. *Nat. Rev. Mater.* **2**, 1–16 (2017).

78. Y. Liu, P. He, H. Zhou, Rechargeable Solid-State Li–Air and Li–S Batteries: Materials, Construction, and Challenges. *Adv. Energy Mater.* **8** (2018).

79. G. F. Dewald, S. Ohno, J. G. C. Hering, J. Janek, W. G. Zeier, Analysis of Charge Carrier Transport Toward Optimized Cathode Composites for All-Solid-State Li−S Batteries. *Batter. Supercaps* **4**, 183–194 (2021).

80. R. Murugan, V. Thangadurai, W. Weppner, Fast lithium ion conduction in garnet-type Li7La 3Zr2O12. *Angew. Chemie - Int. Ed.* **46**, 7778–7781 (2007).

81. B. Liu, *et al.*, 3D lithium metal anodes hosted in asymmetric garnet frameworks toward high energy density batteries. *Energy Storage Mater.* **14**, 376–382 (2018).

82. N. Fairley, *et al.*, Systematic and collaborative approach to problem solving using X-ray photoelectron spectroscopy. *Appl. Surf. Sci. Adv.* **5**, 100112 (2021).

83. J. Moulder, W. Stickle, P. Sobol, K. Bomben, *Handbook of X-ray photoelectron spectroscopy (XPS)* (2005) https:/doi.org/10.1002/0470014229.ch22.

84. A. M. Nolan, Y. Liu, Y. Mo, Solid-State Chemistries Stable with High-Energy Cathodes for Lithium-Ion Batteries. *ACS Energy Lett.*, 2444–2451 (2019).

85. A. Jain, *et al.*, Commentary: The materials project: A materials genome approach to accelerating materials innovation. *APL Mater.* **1** (2013).

86. Z. Fu, *et al.*, Probing the Mechanical Properties of a Doped Li7La3Zr2O12Garnet Thin Electrolyte for Solid-State Batteries. *ACS Appl. Mater. Interfaces* **12**, 24693–24700 (2020).

87. M. Pharr, Z. Suo, J. J. Vlassak, Measurements of the fracture energy of lithiated silicon electrodes of Li-Ion batteries. *Nano Lett.* **13**, 5570–5577 (2013).

88. S. Yu, *et al.*, Elastic Properties of the Solid Electrolyte Li7La3Zr2O12 (LLZO). *Chem. Mater.* **28**, 197–206 (2016).

89. K. Zhao, M. Pharr, S. Cai, J. J. Vlassak, Z. Suo, Large plastic deformation in high-capacity lithium-ion batteries caused by charge and discharge. *J. Am. Ceram. Soc.* **94**, s226–s235 (2011).

90. X. Judez, *et al.*, Lithium Bis(fluorosulfonyl)imide/Poly(ethylene oxide) Polymer Electrolyte for All Solid-State Li-S Cell. *J. Phys. Chem. Lett.* **8**, 1956–1960 (2017).

91. D. B. Shah, *et al.*, Effect of Anion Size on Conductivity and Transference Number of Perfluoroether Electrolytes with Lithium Salts. *J. Electrochem. Soc.* **164**, A3511–A3517 (2017).

92. H. Xiong, X. Zhao, J. Chen, New Polymer - Inorganic Nanocomposites : PEO - ZnO and PEO - ZnO - LiClO 4 Films. 10169–10174 (2001).

93. S. Choudhary, R. J. Sengwa, Morphological, structural, dielectric and electrical properties of PEO–ZnO nanodielectric films. *J. Polym. Res.* **24** (2017).

94. S. Choudhary, Structural, optical, dielectric and electrical properties of (PEO–PVP)–ZnO nanocomposites. *J. Phys. Chem. Solids* **121**, 196–209 (2018).

95. C. Shen, *et al.*, Self-Discharge Behavior of Lithium-Sulfur Batteries at Different Electrolyte/Sulfur Ratios. *J. Electrochem. Soc.* **166**, A5287–A5294 (2019).

96. C. H. Yu, C. S. Cho, C. C. Li, Well-Dispersed Garnet Crystallites for Applications in Solid-State Li-S Batteries. *ACS Appl. Mater. Interfaces* **13**, 11995–12005 (2021).

97. M. Naguib, *et al.*, Interfacial Reactions and Performance of Li7La3Zr2O12-Stabilized Li-Sulfur Hybrid Cell. *ACS Appl. Mater. Interfaces* **11**, 42042–42048 (2019).

98. J. Lin, L. Wu, Z. Huang, X. Xu, J. Liu, La2Zr2O7 and MgO co-doped composite Li-Garnet solid electrolyte. *J. Energy Chem.* **40**, 132–136 (2020).

99. Y. Ruan, *et al.*, Acid induced conversion towards a robust and lithiophilic interface for Li-Li7La3Zr2O12 solid-state batteries. *J. Mater. Chem. A* **7**, 14565–14574 (2019).

100. X. Huang, *et al.*, A Li-Garnet composite ceramic electrolyte and its solid-state Li-S battery. *J. Power Sources* **382**, 190–197 (2018).

101. Y. Lu, *et al.*, Highly stable garnet solid electrolyte based Li-S battery with modified anodic and cathodic interfaces. *Energy Storage Mater.* **15**, 282–290 (2018).

102. C. Luo, *et al.*, A chemically stabilized sulfur cathode for lean electrolyte lithium sulfur batteries. *Proc. Natl. Acad. Sci. U. S. A.* **117**, 14712–14720 (2020).

103. Z. Yuan, *et al.*, Hierarchical free-standing carbon-nanotube paper electrodes with ultrahigh sulfur-loading for lithium-sulfur batteries. *Adv. Funct. Mater.* **24**, 6105–6112 (2014).

104. M. Yao, *et al.*, A Flexible All-in-One Lithium-Sulfur Battery. *ACS Nano* **12**, 12503–12511 (2018).

105. Y. V. Mikhaylik, U. S. Pat. 7,352,680. **2**, U. S. Pat. 7,352,680 (2008).

106. F. Han, Y. Zhu, X. He, Y. Mo, C. Wang, Electrochemical Stability of Li10GeP2S12 and Li7La3Zr2O12 Solid Electrolytes. *Adv. Energy Mater.* **6** (2016).

107. M. F. Sunding, *et al.*, XPS characterisation of in situ treated lanthanum oxide and hydroxide using tailored charge referencing and peak fitting procedures. *J. Electron Spectros. Relat. Phenomena* **184**, 399–409 (2011).

108. C. Naumkin, Alexander; Kraut-Vass, Anna; Gaarenstroom, Stephen; Powell, NIST X-ray Photoelectron Spectroscopy Database20, Version 4.1. (2020) https:/doi.org/http://dx.doi.org/10.18434/T4T88K.

109. G. E. Murch, R. J. Thorn, Relation between orbital binding energies and ionicities in alkali and alkaline earth flourides. *J. Phys. Chem. Solids* **41**, 785–791 (1980).

110. J. Ren, *et al.*, Rational design of a multidimensional N-doped porous carbon/MoS2/CNT nano-architecture hybrid for high performance lithium-sulfur batteries. *J. Mater. Chem. A* **6**, 13835–13847 (2018).

111. D. Briggs, *X-ray photoelectron spectroscopy (XPS)*, 2nd Ed. (2005).

112. S. A. Pervez, *et al.*, Electrochemical and compositional characterization of solid interphase layers in an interface-modified solid-state Li-sulfur battery. *J. Mater. Chem. A* **8**, 16451–16462 (2020).

113. H. Aono, N. Imanaka, G. ya Adachi, High Li+ Conducting Ceramics. *Acc. Chem. Res.* **27**, 265–270 (1994).

114. J. C. Bachman, *et al.*, Inorganic Solid-State Electrolytes for Lithium Batteries: Mechanisms and Properties Governing Ion Conduction. *Chem. Rev.* **116**, 140–162 (2016).

115. K. M. Abraham, S. M. Chaudhri, The Lithium Surface Film in the Li / SO 2 Cell. *J. Electrochem. Soc.* **133**, 1307–1311 (1986).

116. H. Ota, X. Wang, E. Yasukawa, Characterization of Lithium Electrode in Lithium Imides/Ethylene Carbonate, and Cyclic Ether Electrolytes. *J. Electrochem. Soc.* **151**, A427 (2004).

117. M. Zarabian, M. Bartolini, P. Pereira-Almao, V. Thangadurai, X-ray Photoelectron Spectroscopy and AC Impedance Spectroscopy Studies of Li-

La-Zr-O Solid Electrolyte Thin Film/LiCoO 2 Cathode Interface for All-Solid-State Li Batteries . *J. Electrochem. Soc.* **164**, A1133–A1139 (2017).

118. W. Li, *et al.*, Dynamic behaviour of interphases and its implication on high-energy-density cathode materials in lithium-ion batteries. *Nat. Commun.* **8** (2017).

119. C. Shi, *et al.*, 3D Asymmetric Bilayer Garnet Hybridized High-Energy-Density Lithium-Sulfur Batteries. *Prep.*

120. H. Cheng, *et al.*, In situ initiator-free gelation of highly concentrated lithium bis(fluorosulfonyl)imide-1,3-dioxolane solid polymer electrolyte for high performance lithium-metal batteries. *Mater. Today Energy* **20**, 100623 (2021).

121. Q. Zhao, X. Liu, S. Stalin, K. Khan, L. A. Archer, Solid-state polymer electrolytes with in-built fast interfacial transport for secondary lithium batteries. *Nat. Energy* **4**, 365–373 (2019).

122. A. Natarajan, A. M. Stephan, C. H. Chan, N. Kalarikkal, S. Thomas, Electrochemical studies on composite gel polymer electrolytes for lithium sulfur-batteries. *J. Appl. Polym. Sci.* **134**, 1–8 (2017).

123. L. Lodovico, A. Varzi, S. Passerini, Effect of Aging-Induced Dioxolane Polymerization on the Electrochemistry of Carbon-Coated Lithium Sulfide. *Front. Chem.* **7**, 1–6 (2020).

124. Y. Li, *et al.*, Garnet Electrolyte with an Ultralow Interfacial Resistance for Li-Metal Batteries. *J. Am. Chem. Soc.* **140**, 6448–6455 (2018).

125. Y. Gong, *et al.*, Lithium-ion conductive ceramic textile: A new architecture for flexible solid-state lithium metal batteries. *Mater. Today* **21**, 594–601 (2018).

126. Y. Yamada, *et al.*, Unusual stability of acetonitrile-based superconcentrated electrolytes for fast-charging lithium-ion batteries. *J. Am. Chem. Soc.* **136**, 5039–5046 (2014).

127. K. Sodeyama, Y. Yamada, K. Aikawa, A. Yamada, Y. Tateyama, Sacrificial anion reduction mechanism for electrochemical stability improvement in highly concentrated Li-salt electrolyte. *J. Phys. Chem. C* **118**, 14091–14097 (2014).

128. D. W. McOwen, *et al.*, Concentrated electrolytes: Decrypting electrolyte properties and reassessing Al corrosion mechanisms. *Energy Environ. Sci.* **7**, 416–426 (2014).

129. K. Matsumoto, *et al.*, Suppression of aluminum corrosion by using high concentration LiTFSI electrolyte. *J. Power Sources* **231**, 234–238 (2013).

130. S. K. Jeong, M. Inaba, Y. Iriyama, T. Abe, Z. Ogumi, Electrochemical intercalation of lithium ion within graphite from propylene carbonate solutions. *Electrochem. Solid-State Lett.* **6**, 13–16 (2003).

131. S. K. Jeong, M. Inaba, Y. Iriyama, T. Abe, Z. Ogumi, Interfacial reactions between graphite electrodes and propylene carbonate-based solutions: Electrolyte-concentration dependence of electrochemical lithium intercalation reaction. *J. Power Sources* **175**, 540–546 (2008).

132. Y. Yamada, Y. Takazawa, K. Miyazaki, T. Abe, Electrochemical lithium intercalation into graphite in dimethyl sulfoxide-based electrolytes: Effect of solvation structure of lithium ion. *J. Phys. Chem. C* **114**, 11680–11685 (2010).

133. Y. Yamada, M. Yaegashi, T. Abe, A. Yamada, A superconcentrated ether electrolyte for fast-charging Li-ion batteries. *Chem. Commun.* **49**, 11194–11196 (2013).

134. T. Doi, R. Masuhara, M. Hashinokuchi, Y. Shimizu, M. Inaba, Concentrated LiPF6/PC electrolyte solutions for 5-V LiNi0.5Mn1.5O4 positive electrode in lithium-ion batteries. *Electrochim. Acta* **209**, 219–224 (2016).

135. K. Yoshida, *et al.*, Oxidative-stability enhancement and charge transport mechanism in glyme-lithium salt equimolar complexes. *J. Am. Chem. Soc.* **133**, 13121–13129 (2011).

136. S. Takeuchi, *et al.*, Effect of the Addition of Bivalent Ions on Electrochemical Lithium-Ion Intercalation at Graphite Electrodes. *J. Electrochem. Soc.* **163**, A1693–A1696 (2016).

137. W. Xue, *et al.*, Ultra-high-voltage Ni-rich layered cathodes in practical Li metal batteries enabled by a sulfonamide-based electrolyte. *Nat. Energy* **6**, 495–505 (2021).

138. Z. Zhang, *et al.*, Cathode-Electrolyte Interphase in Lithium Batteries Revealed by Cryogenic Electron Microscopy. *Matter* **4**, 302–312 (2021).

139. D. W. McOwen, *et al.*, 3D-Printing Electrolytes for Solid-State Batteries. *Adv. Mater.* **30**, 1–7 (2018).

140. D. V Kosynkin, *et al.*, Longitudinal unzipping of carbon nanotubes to form graphene nanoribbons. *Nature* **458**, 872–876 (2009).

141. C. V. Nguyen, Vertically Allgned Multi-Walled Carbon Nanotubes (2018).

142. C. Yu, *et al.*, Tailoring Li6PS5Br ionic conductivity and understanding of its role in cathode mixtures for high performance all-solid-state Li-S batteries. *J. Mater. Chem. A* **7**, 10412–10421 (2019).

143. Z. Jiang, *et al.*, Robust Li6PS5I Interlayer to Stabilize the Tailored Electrolyte Li9.95SnP2S11.95F0.05/Li Metal Interface. *ACS Appl. Mater. Interfaces* **13**, 30739–30745 (2021).

144. Y. Lin, X. Wang, J. Liu, J. D. Miller, Natural halloysite nano-clay electrolyte for advanced all-solid-state lithium-sulfur batteries. *Nano Energy* **31**, 478–485 (2017).

145. X. Tao, *et al.*, Solid-State Lithium–Sulfur Batteries Operated at 37 °C with Composites of Nanostructured Li7La3Zr2O12/Carbon Foam and Polymer. *Nano Lett.* **17**, 2967–2972 (2017).

146. X. Wang, *et al.*, Sulfurized Polyacrylonitrile Cathodes with High Compatibility in Both Ether and Carbonate Electrolytes for Ultrastable Lithium–Sulfur Batteries. *Adv. Funct. Mater.* **29**, 1–12 (2019).

147. X. Huang, *et al.*, Flexible free-standing sulfurized polyacrylonitrile electrode for stable Li/Na storage. *Electrochim. Acta* **333** (2020).

148. F. Han, Y. Zhu, X. He, Y. Mo, C. Wang, Electrochemical Stability of Li10GeP2S12 and Li7La3Zr2O12 Solid Electrolytes. *Adv. Energy Mater.* **6**, 1501590 (2016).

149. J. Han, Y. Zheng, N. Guo, P. B. Balbuena, Calculated Reduction Potentials of Electrolyte Species in Lithium–Sulfur Batteries. *J. Phys. Chem. C* **124**, 20654–20670 (2020).

150. M. S. Ahmed, *et al.*, Multiscale Understanding of Covalently Fixed Sulfur–Polyacrylonitrile Composite as Advanced Cathode for Metal–Sulfur Batteries. *Adv. Sci.* **8**, 1–34 (2021).

151. N. Wu, *et al.*, In Situ Formation of Li3P Layer Enables Fast Li+ Conduction across Li/Solid Polymer Electrolyte Interface. *Adv. Funct. Mater.* **30**, 1–6 (2020).

152. X. Huang, *et al.*, A Li-Garnet composite ceramic electrolyte and its solid-state Li-S battery. *J. Power Sources* **382**, 190–197 (2018).

153. H. Ben Youcef, *et al.*, Functionalized cellulose as quasi single-ion conductors in polymer electrolyte for all-solid–state Li/Na and Li[sbnd]S batteries. *Solid State Ionics* **345**, 115168 (2020).

154. F. Han, *et al.*, High-performance all-solid-state lithium-sulfur battery enabled by a mixed-conductive Li2S nanocomposite. *Nano Lett.* **16**, 4521–4527 (2016).

155. H. Wan, *et al.*, Bifunctional Interphase-Enabled Li10GeP2S12Electrolytes for Lithium-Sulfur Battery. *ACS Energy Lett.* **6**, 862–868 (2021).

156. X. Tao, *et al.*, Solid-State Lithium-Sulfur Batteries Operated at 37 °C with Composites of Nanostructured Li7La3Zr2O12/Carbon Foam and Polymer. *Nano Lett.* **17**, 2967–2972 (2017).